ADVANCED MATERIALS

www.advmat.de

On-Demand Reconfiguration of Nanomaterials: When Electronics Meets Ionics

*Jihang Lee and Wei D. Lu**

Rapid advances in the semiconductor industry, driven largely by device scaling, are now approaching fundamental physical limits and face severe power, performance, and cost constraints. Multifunctional materials and devices may lead to a paradigm shift toward new, intelligent, and efficient computing systems, and are being extensively studied. Herein examines how, by controlling the internal ion distribution in a solid-state film, a material's chemical composition and physical properties can be reversibly reconfigured using an applied electric field, at room temperature and after device fabrication. Reconfigurability is observed in a wide range of materials, including commonly used dielectric films, and has led to the development of new device concepts such as resistive random-access memory. Physical reconfigurability further allows memory and logic operations to be merged in the same device for efficient in-memory computing and neuromorphic computing systems. By directly changing the chemical composition of the material, coupled electrical, optical, and magnetic effects can also be obtained. A survey of recent fundamental material and device studies that reveal the dynamic ionic processes is included, along with discussions on systematic modeling efforts, device and material challenges, and future research directions.

1. Introduction

The rapid growth of modern electronics has had unparalleled impact on the ways humans work, live, and socialize in the past few decades. This exponential growth has mostly been driven by device scaling, i.e., constant shrinking of the size of transistors that form the basic building block of integrated circuits, following Moore's law.[1] However, continued geometrical scaling will likely come to a halt within the next decade as the device size approaches fundamental physical limits at ≈5 nm. New materials that offer new functionalities and provide new state variables, which can be used for computing and data storage, are of great interest to maintain the growth of the semiconductor industry.

A close examination of today's electronics systems reveals that they are mostly based on "functional reconfigurable" materials and devices. That is, the device's electrical and optical properties can be modulated upon the application of a stimulation, normally an electric field, but the change is temporary, and the device will recover its original form after the stimulation removal. For example, light-emitting diodes can emit light when a voltage is applied, but the material itself is not modified during the process. Light emission will stop when the voltage is removed. Similarly, a transistor can be turned "on" by a gate voltage but will return to the "off" state when the gate voltage is removed. On the other hand, if a material is not only functional reconfigurable, but also "physically reconfigurable" at the atomic scale, its electrical, optical, mechanical, and magnetic properties can be modified "on the fly" in a "nonvolatile" yet "reversible" fashion, thus can potentially facilitate a paradigm shift in building highly efficient computing systems. For example, compute-in-memory and compute-with-memory concepts have received tremendous interest recently as an alternative architecture to perform "big data" tasks compared to conventional computing architectures. However, the performance of these memory-first approaches is often limited by the properties of the memory and by the ability to integrate large amounts of memory directly with the logic components. Emerging memories based on physical reconfiguration effects, such as resistive random-access memory (RRAM), offer advantages of nonvolatile storage, high density, and fast and random access, and can dramatically simplify the memory hierarchy and improve the system performance.[1–4] In an RRAM, the different stored data are represented by the different resistance values of the storage material through physical ion migrations and associated chemical redox processes within the film.[2,5,6] By directly changing the properties of the storage material itself, the device also directly modulates the signals propagating through it, thus allowing logic functions to be performed at the same physical locations as the memory element, leading to significant speed and energy benefits.[4]

For any device, physical reconfiguration involves moving matter (i.e., atoms) within the device. In this review, we focus on devices where the reconfiguration of the material and device is achieved through electric-field-driven redistribution of ions over large distances (compared to the lattice constant/atomic spacing), allowing the devices and circuits to be reconfigured

J. Lee, Prof. W. D. Lu
Department of Electrical Engineering and Computer Science
University of Michigan
Ann Arbor, MI 48109, USA
E-mail: wluee@umich.edu

J. Lee
Department of Materials Science and Engineering
University of Michigan
Ann Arbor, MI 48109, USA

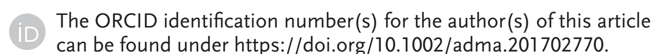
The ORCID identification number(s) for the author(s) of this article can be found under https://doi.org/10.1002/adma.201702770.

DOI: 10.1002/adma.201702770

 © 2017 WILEY-VCH Verlag GmbH & Co. KGaA, Weinheim

conveniently in situ, through simple changes in bias voltages[2,6] One representative example of such reconfigurable devices is RRAM, which exhibits resistive switching effects as a result of the reversible ion migration. In this review, we aim to first provide a summary of the coupled electronic and ionic processes that govern resistive switching effects, by analyzing recent experimental observations and theoretical simulations. Afterward, applications of these reconfigurable materials and devices that offer tunable electrical, optical, and magnetic properties will be introduced, with a focus on memory, logic, and neuromorphic computing systems. Finally, discussions on new research directions that can lead to promising multifunctional systems will be provided.

Jihang Lee received his B.S. degree in materials science and engineering from Seoul National University, South Korea, in 2012. He is currently pursuing a Ph.D. degree at the University of Michigan, USA. His research interests focus on nanomaterials and memristive devices based on nanoionics for memory and neuromorphic computing applications.

Wei D. Lu received his B.S. degree in physics from Tsinghua University, Beijing, China, in 1996, and Ph.D. in physics from Rice University, Houston, TX, USA, in 2003. From 2003 to 2005, he was a postdoctoral research fellow at Harvard University, Cambridge, MA, USA. In 2005, he joined the faculty of the Electrical Engineering and Computer Science Department at the University of Michigan and is currently a Professor. He is the Director of the Lurie Nanofabrication Facility and Associate Editor for Nanoscale. His research interest includes resistive random-access memory, memristor-based logic circuits, neuromorphic computing systems, aggressively scaled transistor devices, and electrical transport in low-dimensional systems.

2. Coupled Electronics and Ionics: Mechanisms

In conventional electronic devices such as transistors, the information is processed by controlling the mobile carriers, e.g., electrons, schematically shown in **Figure 1**. Ions such as dopants are necessary to build the device during fabrication, but are not actively modulated/programmed during device operation. Thus, no physical changes to the devices and materials are involved during device operation. On the contrary, physical reconfiguration of a material requires moving matter (atoms or ions) during the device operation. Although devices based on ionic processes have been extensively studied for other types of applications (e.g., batteries), these devices are normally based on materials that are incompatible with semiconductor electronics and have not been seriously considered as electronic devices. For example, fast ion transport and storage are desirable for conventional ionic devices such as Li-ion batteries and supercapacitor devices,[7,8] while electronic effects are considered secondary. As a result, traditionally, electronic devices and ionic devices utilize distinct classes of materials (the former aiming for materials with high electronic mobility and essentially zero ion mobility, while the latter aiming for materials with high ionic mobility) and target dramatically different applications.[9–11]

Recent advances in thin-film and fabrication technologies, combined with developments in characterization and measurement techniques, have now made it possible to control the migration of individual atoms (ions) in even conventional insulators and semiconductors.[6] These devices can be programmed at high speed with operation parameters compatible with conventional electronic circuits, and thus enable the merge of ionics with electronics. For example, ionic-based resistive switching devices that operate by controlled physical reconfiguration of the switching material, schematically shown in Figure 1, have been extensively studied with excellent performance metrics.[2,6] Specifically, these devices possess the simplicity of a resistor—with the whole device structure consisting of only two electrodes sandwiching a "switching" medium. Unlike a simple resistor, however, the device offers the capability to change its resistance on demand, and more importantly, the ability to store (memorize) the new resistance state as needed, thus, the name memristor (memory + resistor)[12–14] or RRAM in memory applications. The resistance change and storage (termed resistive switching, RS) effects are achieved by the redistribution of ions (atoms) in the switching layer, which, in turn, modulates the local resistivity and the overall electrical resistance of the device.[2,6] In this case, the functionality is realized through ionic processes, but the information is sensed and processed through electrical signals, achieving efficient data storage and computing functions in an extremely compact structure.

Nanoionic devices such as resistive switching devices can be classified in several different ways from materials, switching mechanisms, to switching characteristics and applications.[1,2,5,6] Based on the switching mechanism, commonly studied resistive switching devices can be generally divided into two groups: devices based on the migration and redistribution of metal cations such as Ag or Cu ions, and devices based on the migration of anions such as oxygen ions, leading to redistribution of oxygen vacancies (V_Os). In both types of devices, the RS process is generally triggered by ionic migration leading to the formation of conductive paths for mobile carriers (e.g., electrons), while each type of device may exhibit its own distinct characteristics due to the different material properties and internal dynamics involved in the RS process. In this section, characteristics of each device group will be reviewed based on the microscopic RS mechanism.

© 2017 WILEY-VCH Verlag GmbH & Co. KGaA, Weinheim

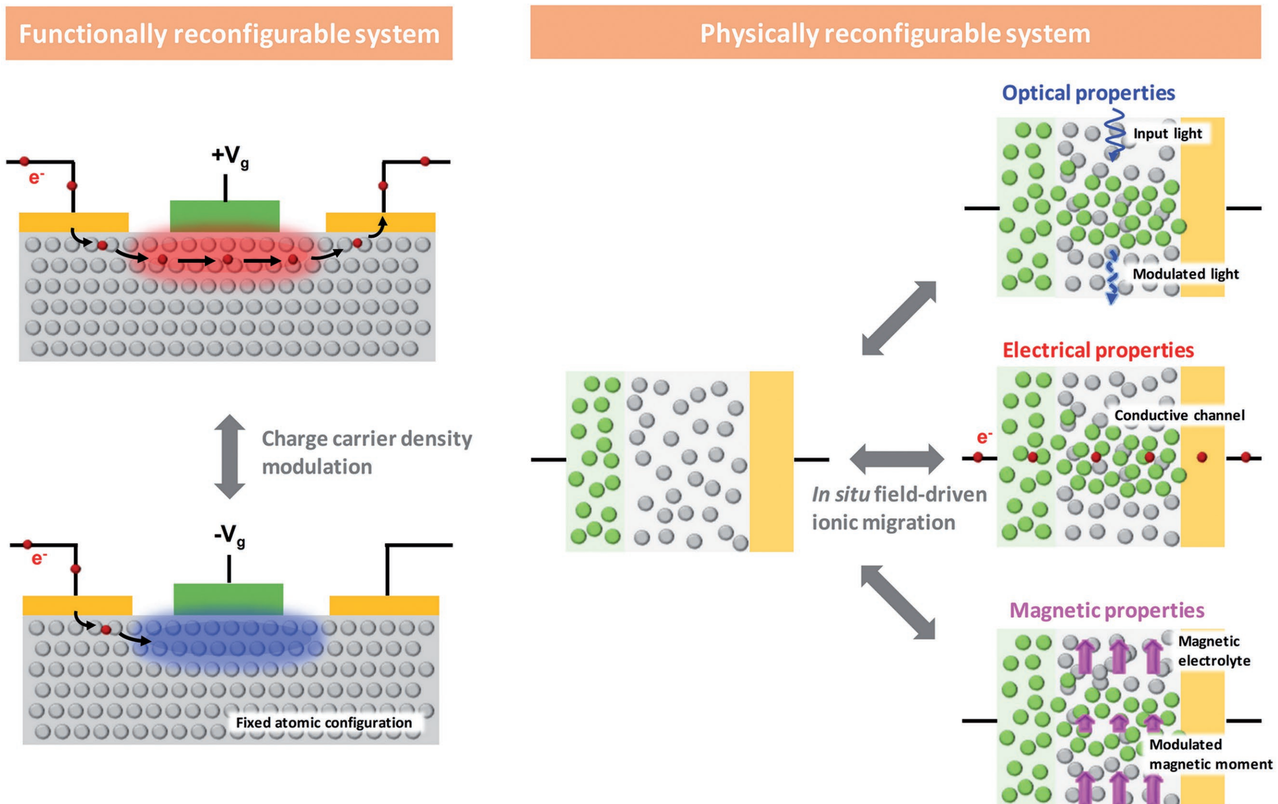

Figure 1. Schematic illustration showing how functionally (left) and physically (right) reconfigurable systems are operated differently. The operation of conventional electronic devices such as transistors is based on the modulation of mobile charge carriers, using a fixed atomic configuration; while the operation of coupled ionic/electronic devices involves physical changes based on ionic migration and chemical reactions, allowing in situ, on-demand control of electronic, optical, and magnetic properties of materials and devices. For example, transmission through a dielectric-based waveguide can be modulated by the formation of an electrically formed metallic filament (upper panel). Resistive switching behaviors have been commonly observed in anion- and cation-based memory devices (middle panel), and magnetization of a ferromagnetic material may be controlled by ion intercalation/de-intercalation, followed by redox reactions, leading to changes of the magnetic moment (bottom panel).

2.1. Electrochemical Metallization Devices

RS devices based on cation migration are usually termed electrochemical metallization (ECM) cells, sometimes also called conductive bridge random-access memory in the literature.[2,5,15] The basic structure of an ECM cell consists of an electrochemically active electrode such as Ag or Cu, an "insulator" layer serving as the switching layer, and an electrochemically inert counter electrode.[2,5,6,15,16] The insulator layer in ECM cells plays the role of a solid electrolyte for Ag or Cu cation migration, and can be based on either conventional electrolyte materials such as chalcogenides[2,17] or even common dielectric materials such as SiO_2,[18] Al_2O_3,[19,20] or amorphous Si (a-Si).[21,22]

During RS, an essentially new material is created in the switching material in an ECM cell, through electrochemical processes and ion migration processes. For example, an Ag filament can be created in an a-Si switching layer under the applied bias, converting the device from the insulating "off" state to the conducting "on" state through this physical reconfiguration process.[21,22] Three steps are normally involved during this material reconfiguration process: oxidation, migration, and reduction of the cations to form the filaments,[2,6,15,17] schematically shown in **Figure 2**a. First, the active anode material (e.g., Ag or Cu) becomes ionized into Ag or Cu cations under an external voltage bias. The ionization rate can be exponentially speeded up under the applied bias, as described by the Butler–Volmer equation.[23,24] Second, facilitated by the applied electric field, the Ag or Cu cations migrate toward the inert electrode through the solid electrolyte. Again, under high field this ion-transport process can be exponentially speeded up due to the barrier lowering effect, allowing fast ion transport in the switching layer at room temperature, as shown in Figure 2c and Equation (1)[15,25]

$$v = a \cdot f \cdot \exp\left(-\frac{E_a}{k_B T}\right) \cdot \sinh\left(\frac{qaE}{2k_B T}\right) \quad (1)$$

where v is the drift velocity of the cation, a is the distance between two sites that can store the ion (the hopping distance), f is the attempt frequency, E_a is the energy barrier for ion migration, E is the applied electric field, k_B is Boltzmann's constant, q is the ion's charge, and T is the absolute temperature. Note that the high-field condition can be readily met in nanoscale thin films even at moderate voltages (e.g., 1 V).[6] The long-distance migration of the ions is a key feature in RRAM

© 2017 WILEY-VCH Verlag GmbH & Co. KGaA, Weinheim

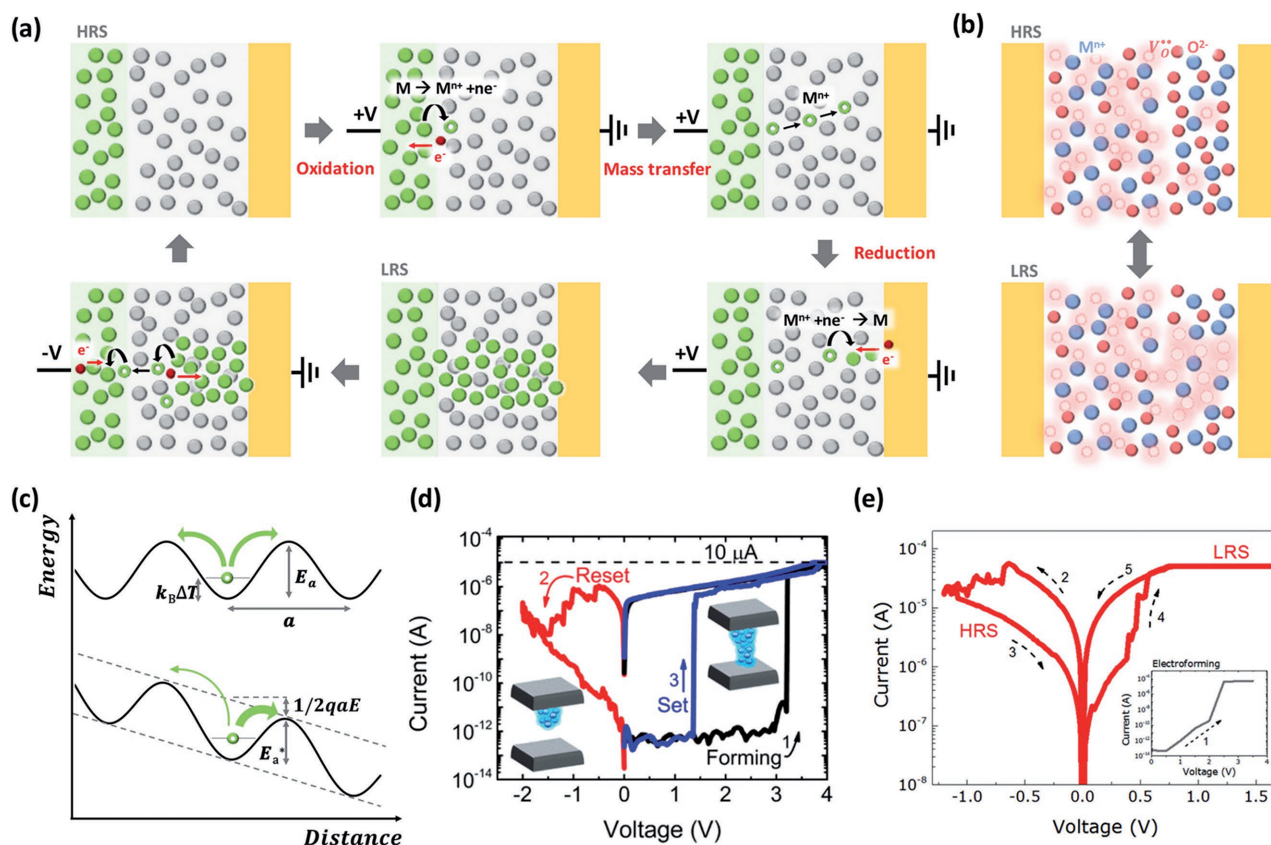

Figure 2. a,b) Schematic illustration of the resistive switching process in a) ECM and b) VCM devices. c) Field-driven acceleration of ionic transport, where the effective energy barrier is lowered by the applied field. d) *I–V* characteristics of a typical ECM device showing large on/off ratio with high off-state resistance. Reproduced with permission.[26] Copyright 2014, American Chemical Society. e) *I–V* characteristics of a typical VCM device. Reproduced with permission.[56] Copyright 2015, American Chemical Society.

and differentiates these devices from other nonvolatile memories that are also based on ion/atom rearrangements such as phase-change memory (where local ordering of the atoms is changed) and ferroelectric memory (where the ion displacement is within a unit cell).

Finally, the displaced Ag or Cu cations become reduced to elemental Ag or Cu atoms after capturing electrons, leading to the nucleation and growth of metal clusters within the switching layer through nucleation and deposition processes, eventually resulting in the creation of nanoscale metal filaments (Figure 2a).[2]

The completion of a metal filament creates an electrically conductive path inside the dielectric layer that leads to a low-resistance state (LRS), with an abrupt conductance increase in the *I–V* curve as shown in Figure 2d.[2,6,15,17,26] The reverse process, where a segment of the filament is broken by physically and chemically removing a portion of the filament material, leads to the reset process that switches the device back to the high-resistance state (HRS).

The dynamics of the physical and chemical ionic processes during RS in ECM devices have been studied through cyclic voltammetry (CV) measurements using very slow sweep rates. (Ionic) Current peaks corresponding to characteristic oxidation and reduction processes of Cu ions were observed in a Cu/SiO_2/Pt device,[27,28] as shown in **Figure 3**a. These measurements help identify the partial electrochemical redox reactions of the cations during the RS process. For example, during the subsequent negative sweep after a positive sweep, Cu ions are reduced, and thus the concentration of Cu ions near the Cu/SiO_2 interface is significantly decreased. As a result, the ionic current is limited by the diffusion of Cu ions injected into SiO_2 through the first oxidation process, leading to the negative current peaks marked as $J_{p,red}$ in Figure 3a. In addition, the peak ionic current values are proportional to the square root of the voltage sweep rate, as shown in Figure 3b, as expected from the Randles–Sevcik equation for electrochemical processes

$$j_p = 2.99 \times 10^5 \times z^{3/2} \times c_{ox} \times \sqrt{\alpha D_{ox} v} \quad (2)$$

where j_p, z, c_{ox}, α, D_{ox}, and v are the peak current density, the number of electrons transferred during the redox reaction, the concentration of the ions, the charge transfer coefficient, the diffusion coefficient of the ions, and the sweep rate, respectively. These quantitative analyses rule out parasitic effects such as the capacitance effect as possible causes of the observed current peaks. Additionally, it has been found that kinetic parameters such as the ion diffusion coefficient and the ion mobility depend on the ion concentration, which is in turn affected by the voltage sweep rate, as shown in Figure 3c,d.[28,29] Specifically, the ion diffusion coefficient and the ion mobility decrease

 © 2017 WILEY-VCH Verlag GmbH & Co. KGaA, Weinheim

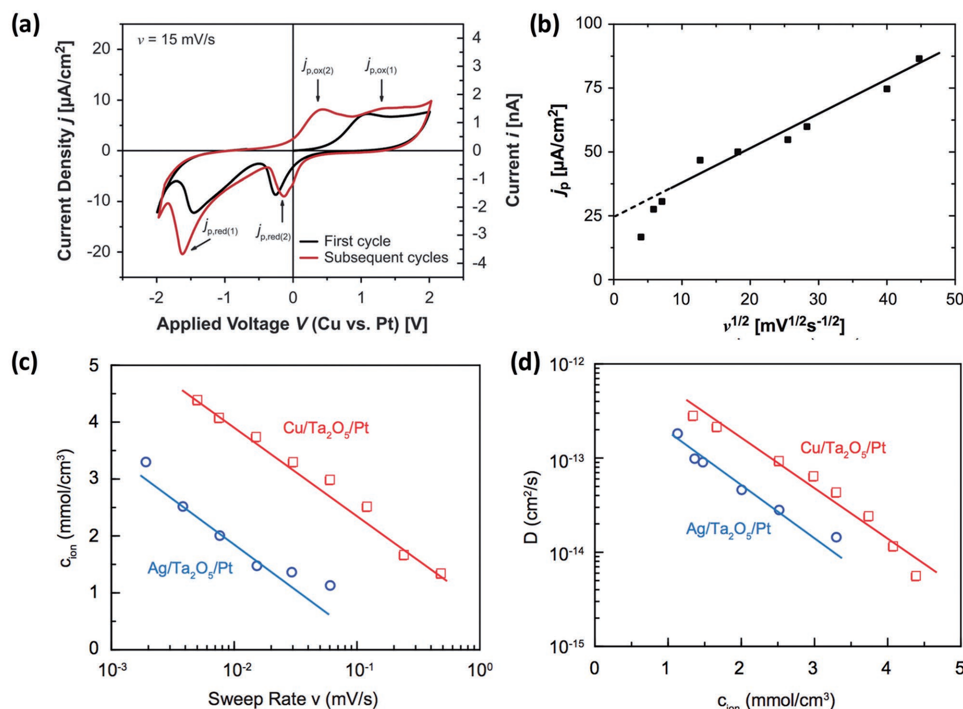

Figure 3. a) Cyclic voltammetry of a $Cu/SiO_2/Pt$ cell, showing current density peaks corresponding to Cu-ion oxidation and reduction processes. Reproduced with permission.[28] Copyright 2012, Royal Society of Chemistry. b) Current density peak value versus voltage sweep rate, showing a linear relation between j_p and $\nu^{1/2}$. Reproduced with permission.[27] Copyright 2011, AIP Publishing LLC. c) Ion concentration versus voltage sweep rate, showing a decrease of the ion concentration as the sweep rate increases.[29] d) Ion diffusion coefficient versus ion concentration, showing a decrease of the ion diffusion coefficient as ion concentration increases, and implying that the electrolyte behaves as a concentrated solution with non-negligible ion–ion interactions. Reproduced with permission.[29] Copyright 2015, John Wiley and Sons.

as ion concentration increases (Figure 3d), indicating that the electrolyte near the reactive electrode behaves as a concentrated solution instead of a diluted solution in CV measurements.[28,29] In other words, ion–ion interactions are not negligible and thus transport of ions is more retarded under higher ion concentration, leading to smaller diffusion coefficient and ion mobility. In particular, a high ionic diffusion coefficient is expected at high sweep rates, supporting the feasibility of electrochemically assisted ion migration even in conventional dielectric materials and at low temperatures (i.e., room temperature).[28] Clear redox peaks were also observed from CV measurements in other ECM systems, such as $Ag/SiO_2/M$ and Ag or Cu/Ta_2O_5/M (where M = Pt, Ir, Ru, etc.).[29,30]

A key characteristic of the ECM cell is the use of an active electrode which provides the active ionic species (metal cations), while the switching layer acts mainly as a physical storage medium (to first order) and does not participate in the chemical redox processes.[2,6,15,17,26] For example, it has been found that Ag or Cu does not form chemical compounds with common insulator-based host switching material such as SiO_2 and, instead, exists as elemental metal inside the dielectric.[31,32] As a result, dramatic changes to the material properties can be obtained as the new material (filament) is injected and removed from the switching material. Additionally, during reset it is possible to fully remove the filament material to create a gap region that maximally recovers the excellent insulating property of the host material (schematically shown in Figure 2a); thus, the reset can lead to a very high off-state resistance in ECM devices and a high on/off resistance ratio, as seen in the *I–V* characteristics during RS of a typical ECM device (Figure 2d).

2.2. Valence Change Memory Devices

Physical and chemical ionic processes can also occur in oxide-based solid electrolytes, where the active ionic species are oxygen ions or oxygen vacancies. Resistive switching devices based on such devices are sometimes termed valence change memory (VCM) or simply referred to as oxide RRAM in the literature.[2] In VCM devices, inert electrodes are used as both the anode and the cathode, and the active species (e.g., V_Os) are present internally inside the switching material stack (e.g., in a nonstoichiometric suboxide[33–35] or at an interface formed through an oxygen gettering material such as a Ti electrode layer[36,37]), as shown in Figure 2b.

RS in VCM devices is driven by the internal redistribution of oxygen vacancies between the V_O-rich and the V_O-poor layers, again involving physical ion migrations and chemical redox processes. Specifically, under a high applied field, oxygen vacancies migrate from a V_O-rich reservoir layer into the near-stoichiometric switching layer that initially has high resistance. As the V_O concentration in the switching layer increases, percolated paths for electron conduction can form at high V_O concentrations, and switch (set) the device from a high-resistance "off" state to a low-resistance "on" state.[4,38] The reverse process

 © 2017 WILEY-VCH Verlag GmbH & Co. KGaA, Weinheim

corresponds to the reset step that switches the device from "on" to "off."

One key feature of VCM devices is that the switching layer will also actively participate in the redox chemical processes, e.g., during set that forms a conducting suboxide channel (filament), the metal cation in the oxide is reduced to a lower oxidation state[2,39,40] and recovers back to the near-stoichiometric oxide composition during reset, schematically shown in Figure 2b. Because the active species, V_Os, are native defects in these oxides and also chemically react with the switching material, it is difficult to completely remove all V_Os from the switching layer and fully restore the near-stoichiometric composition during reset. As a result, the off-state resistance of VCM devices is generally leakier than that of ECM devices, leading to smaller on/off ratios,[4,41] as shown in Figure 2e. On the other hand, VCM devices generally exhibit more reliable switching characteristics with better write/erase endurance due to the use of native ionic species instead of foreign ionic species as in the case of ECM devices, as the repeated insertion and removal of foreign cations in a solid dielectric film may lead to plastic deformation of the film and irrecoverable damage if programming conditions are not optimally set.[34,42]

3. Fundamental Experimental Studies and Modeling

3.1. In Situ Transmission Electron Microscopy Observations

To experimentally reveal the microscopic origin of resistive switching processes, material characterization techniques such as transmission electron microscopy (TEM)[31,32,40,43–47] energy dispersive X-ray spectroscopy,[31,48,49] X-ray absorption spectroscopy (XAS),[50–52] electron energy loss spectroscopy (EELS),[44,45,47] photoemission electron microscopy (PEEM),[53–55] and conductive atomic force microscopy (C-AFM)[26,56] have been employed. As the most direct method, physical reconfigurations of the switching layer have been analyzed via microscopic imaging techniques. Specifically, several TEM-based studies using high-resolution imaging and spectroscopic analysis tools combined with electrical measurements have provided direct evidence of (long distance) ion migration during RS processes for both ECM and VCM types of devices.[31,32,40,43–45,47,50,57–59]

3.1.1. ECM Devices

Figure 4a,b highlights the formation/rupture of nanoscale Ag filaments after set/reset in an Ag/SiO_2/Pt-based ECM device (fabricated in a planar structure on a SiN_x membrane, inset).[31] The as-fabricated device was turned into the low-resistance state with an abrupt increase in current after application of a constant positive voltage bias, as shown in Figure 4c. The electrical resistance change was found to accompany changes in the electrode and the switching material (Figure 4a,c), where the active electrode material, i.e., Ag, was found to be injected into the insulating SiO_2 layer (acting as the switching layer) under the applied electric field. The device is switched "on" when the two electrodes are connected by the Ag filament, abruptly changing the device's electrical resistance. Upon voltage bias of opposite polarity, the device switched back to the high-resistance

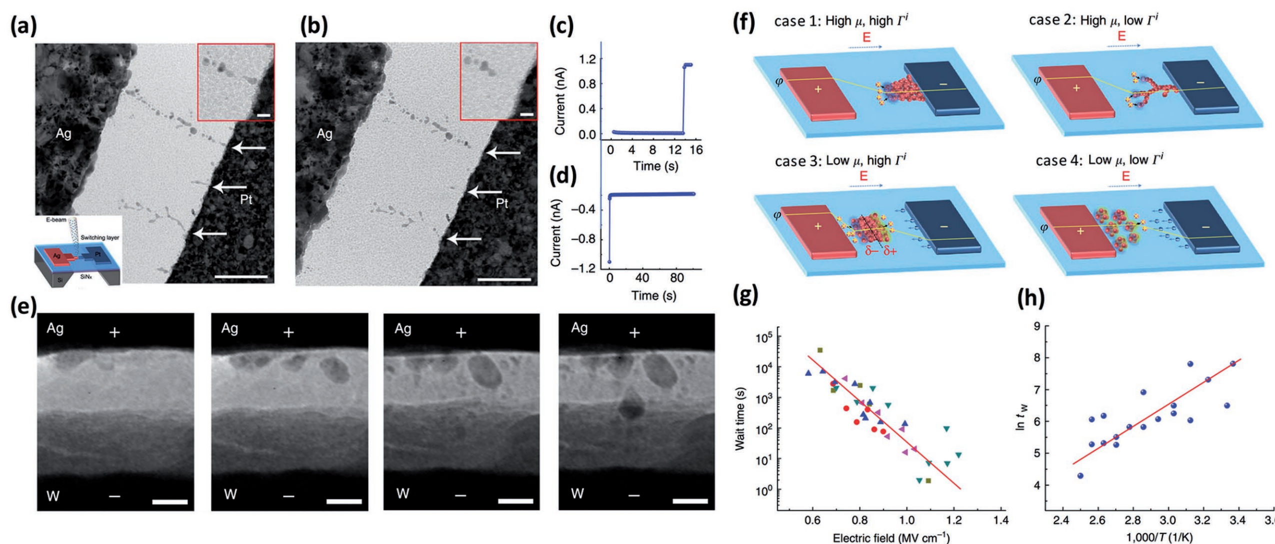

Figure 4. a) TEM image of an Ag/SiO_2/Pt-based device after the forming process, showing the formation of conductive filaments. Inset: schematic of the planar-structured device for TEM observation. b) TEM image of the same device in panel (a) after reset showing the dissolution of the filaments at the inert electrode interface. c) *I*–*t* curve during the forming process under constant bias. The abrupt current increase corresponds to the formation of filaments shown in panel (a). d) *I*–*t* curve during the reset process under constant bias. The abrupt current drop corresponds to the rupture of filaments shown in panel (b). e) Real-time structural evolutions of an Ag/a-Si/W-based device obtained through in situ TEM observation, showing the dynamic filament growth process that initiates from the reactive electrode. Reproduced with permission.[31] Copyright 2012, Nature Publishing Group. f) Schematic illustration of filament growth dynamics at different cases, depending on kinetic parameters such as the redox rates, Γ, and ion mobility, μ. Reproduced with permission.[32] Copyright 2014, Nature Publishing Group. g) Wait time as a function of the applied electric filed during the forming process, showing exponential dependence consistent with Equation (1). h) Arrhenius plot of the wait time versus temperature, consistent with Equation (1).[31]

© 2017 WILEY-VCH Verlag GmbH & Co. KGaA, Weinheim

state (Figure 4d), corresponding to the rupture of the filament (Figure 4b) due to similar redox reactions and ionic migration in the reverse direction. These observations unambiguously reveal the physical nature of the RS process, where the physically displaced Ag atoms lead to dramatic changes to the device's electrical properties.

Besides allowing direct observation of the metal filaments during RS, in situ TEM analyses provide important information concerning the microscopic dynamic ionic processes during filament growth. Figure 4e shows real-time structural evolutions of an Ag/a-Si/W device under a constant voltage bias from an in situ TEM study.[31] The filament growth process can be directly correlated with the electrical measurements, allowing one to identify the different steps during filament growth in real time. Subsequent systematic in situ TEM analyses provided a complete picture of the different dynamic processes that can occur in an ECM device, e.g., filament growth direction, geometry, and morphology.[32] Based on these experimental studies, a model that incorporates key kinetic factors such as the ion mobility and the oxidation/reduction rate has been developed that can reconcile previously reported, seemingly contradicting experimental findings, depending on which ionic process becomes rate limiting.[6,32,60]

Specifically, the filament growth/dissolution dynamics in ECM devices can be classified into four categories based on the ion mobility and the redox reaction rate (Figure 4f). Note that both parameters not only depend on the material properties but can also be affected by programming conditions such as the applied electric field and temperature:[32] (1) in cases with high ion mobility and high redox rates, the active cations injected into the electrolyte during set will be reduced at the inert (cathodic) electrode due to the high ion mobility, leading to filament growth initiated from the inert electrode. A large amount of ion supply due to the high oxidation rate results in the formation of cone-shaped filaments with a large base at the inert electrode interface.[60] Such inverted cone-shaped filaments have been observed in ECM devices using classical solid electrolytes such as GeTe[43] that are known to be good ionic conductors. (2) In cases with high ion mobility and low redox rate, filaments will grow from the cathode because of the high ion mobility, similar to the previous case. The filament shape and filament dissolution behaviors, however, will be different because the oxidation process is slow and rate limiting, so that the supply of cations is limited. The limited cations will be more likely to get reduced at the tip of existing filaments where the field is enhanced, leading to the formation of branched filaments such as the case observed in porous sputtered-SiO_2 (Figure 4a,b).[31,57,60] Categories (3) and (4) correspond to systems with low cation mobility, which will exhibit a different filament growth direction compared to the high cation mobility cases because ionic transport is now the rate-limiting process. In particular, the nucleation of metal clusters could occur inside the electrolyte before the cations reach the inert electrode interface due to the slow movement of ions.[31,60] The precipitated metal clusters inside the electrolyte will extend the filament growth from the active electrode toward the inert electrode during set.[6,32] Indeed, forward growth of filaments was experimentally observed in ECM devices using nonconventional electrolyte such as amorphous Si[31] and oxides such as ZrO_2[58] and plasma-enhanced chemical vapor deposition (PECVD)-grown SiO_2[59] that are known to have lower ion mobility compared to conventional electrolytes. The differences in redox rates can further lead to different filament shapes, with continuous extension of the anode toward the cathode when the redox rate is high, case (3),[32] and discrete nanoclusters and overall forward cone-shaped filaments when the redox rate is low, case (4), as shown in Figure 4e.[31]

The exponential field acceleration, a key feature of the ionic-based RS devices, has also been verified by systematically examining the wait time for the abrupt current change as a function of the applied field. Several studies have demonstrated that the wait time depends exponentially on the electric field, and shows an Arrhenius relationship with the temperature,[31] as shown in Figure 4g,h respectively, consistent with predictions from Equation (1) in cases where ion migration is the rate-limiting process.

3.1.2. VCM Devices

Similar to ECM devices, there have been extensive studies aimed to observe conductive filaments (CFs), and to identify the origin of RS behaviors in oxide-based devices such as TiO_2,[40,50] Ta_2O_5,[45,47] and ZnO[44] systems, using TEM techniques in conjunction with spectroscopic analysis.

Figure 5 shows high-angle annular dark-field (HAADF) scanning TEM (STEM) images of the same location in a Pt/SiO_2/Ta_2O_{5-x}/TaO_y/Pt device, after applying negative (set) and positive (reset) voltages, respectively, using an in situ experimental setup. Clear contrast differences in the HAADF–STEM images can be observed, indicating changes in the composition of the film at different resistance states. Regions corresponding to localized, nanoscale conductive channels with a different composition compared to the host material are indicated by the yellow arrows in Figure 5a. EELS line-scan analysis confirmed that the contrast changes in the STEM images are due to differences in oxygen concentration in the switching regions. Specifically, the local oxygen concentration after the set operation is reduced compared to the off-state, shown in Figure 5d, verifying the role of V_O migration during the operation of VCM devices.

Like metal ions in ECM devices, the migration of V_Os and the associated redox processes cause direct changes to the chemical composition and physical properties of the switching layer. In this case, the redistribution of oxygen vacancies modulates the stoichiometry of the oxide-based switching layer and in turn the film's electrical conductivity, although the changes in material properties may be less dramatic compared with ECM devices where complete new materials are created in the host. Similar to ECM devices, the modulation of the chemical composition and the electrical properties of the switching material in VCM devices can be reversed by applying a voltage bias in the opposite polarity. In this case, typically longer write/erase endurance cycles can be obtained in VCM devices due to the involvement of only native ionic species during the chemical and physical processes.[33,34]

3.2. Other Experimental Techniques

It is generally more challenging to directly observe filament evolution in VCM devices[61] since the filaments consist of native

© 2017 WILEY-VCH Verlag GmbH & Co. KGaA, Weinheim

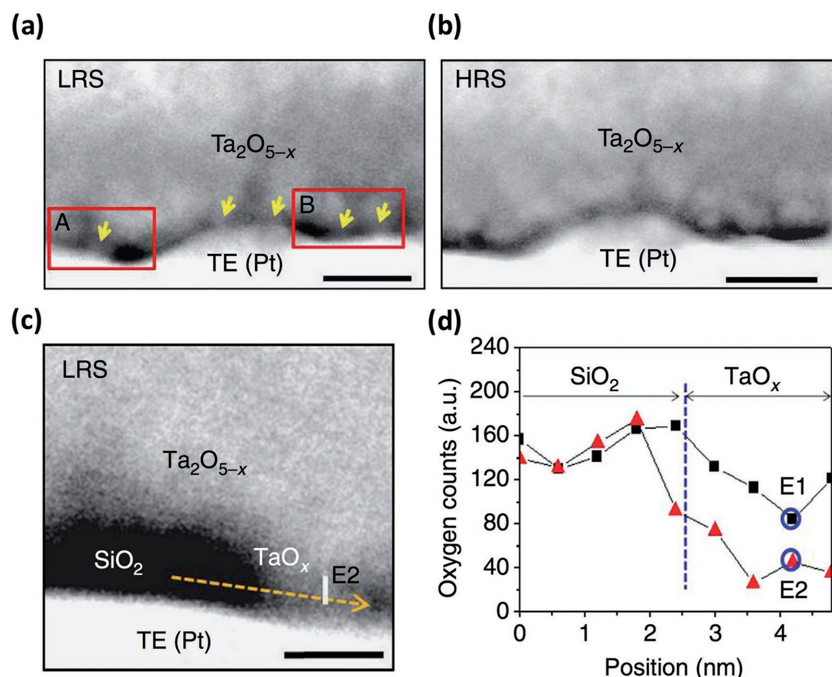

Figure 5. a,b) In-situ HAADF–STEM image of a $Pt/SiO_2/Ta_2O_{5-x}/TaO_y/Pt$ device in a) LRS and b) HRS, showing the formation/annihilation of nanoscale channels in a thin SiO_2 layer, as indicated by yellow arrows in panel (a). Scale bars: 5 nm. c) Magnified image of a channel region in LRS. Scale bar: 2 nm. d) Oxygen EELS line scan profiles obtained from LRS (red triangle) and HRS (black square) along the horizontal direction as indicated by the yellow arrow in panel (c). Significant changes of oxygen concentration between the LRS and the HRS are observed in the channel region. Reproduced with permission.[45] Copyright 2013, Nature Publishing Group.

defects, i.e., oxygen vacancies rather than foreign metallic species. Careful spectroscopic analysis is typically required to confirm the composition changes. A host of state-of-the-art techniques such as XAS,[51,52] PEEM,[53–55] and electron holography[62] has recently been employed to comprehensively characterize the changes in film microstructure, composition, and chemical states accompanying the resistive switching effects in VCM devices. However, continued improvements in spatial and temporal resolution are still needed to clearly reveal in real time the nanoscale filament growth dynamics.

3.2.1. XAS Analysis

Spatially resolved XAS using scanning transmission X-ray microscope (STXM) was performed to nondestructively investigate the chemical and structural changes during RS.[50] After electroforming and set/reset cycling, a localized region showing a different absorption spectrum from that of the surrounding matrix was clearly observed in the STXM image of a TiO_2-based device, as shown in **Figure 6**a.[50] The altered absorption spectrum after the electrical cycling matches that of reduced titanium oxide, in which the valence state of the Ti ions is reduced from +4 to +3, while the absorption spectrum of the titanium oxide layer in virgin state with no prior electrical treatment is consistent with stoichiometric titanium dioxide (Figure 6b). Electron diffraction measurement revealed that the localized region consists of the Ti_4O_7 *Magnéli* phase with metallic conductivity, supporting the formation of localized conducting channels due to oxygen vacancy migration during resistive switching. Localized conducting channels with reduced oxygen concentration after electrical forming/set were also found in a Ta_2O_5-based device from X-ray measurements, consistent with the results obtained from cross-sectional TEM and EELS studies.[63,64]

Thermally driven radial migration of oxygen ions/vacancies and the associated local composition changes were also verified by X-ray photoemission electron spectromicroscopy upon application of multiple high-voltage pulses.[52] Figure 6c shows the O K-edge X-ray transmission intensity map of an electrically cycled Ta_2O_5-based device, where a ring-like feature with a bright inner core and a dark perimeter is observed. Besides field-driven drift of oxygen ions/vacancies in the vertical direction (parallel to the field), temperature gradients due to Joule heating near the localized conduction paths produce thermophoretic forces that cause lateral, inward migration of V_Os (i.e., Soret diffusion),[65] which is, in turn, balanced by Fick diffusion driven by the V_O concentration gradient. As a result, lateral segregation of oxygen-deficient and oxygen-rich regions occurs, corresponding to the bright and dark areas in Figure 6c, respectively. It was found that electrical cycling with high power amplified the lateral V_O migration, eventually inducing irreversible changes to the material, including strong clustering of defects and accelerated device failure. The change of the Ta oxidation state (due to V_O migration) rather than the Ta concentration (due to Ta migration) in the oxygen-deficient region was also verified by Ta L-edge X-ray transmission analysis, consistent with the now generally accepted theory of VCM devices. On the other hand, it has been recently observed that cation migration is also possible in VCM devices under high bias,[66] which should be generally avoided and may affect the reliability of the device operations.

In addition, XAS has been employed to investigate the detailed information of local structural changes and chemical reactions during the operation of RRAM devices. Specifically, the X-ray fine structure (XAFS) technique can provide short-range structure information (e.g., local atomic arrangement, bond distances, and coordination number) from extended XAFS (EXAFS) analysis, as well as local chemical environment (e.g., oxidation state and local coordination) through X-ray absorption near-edge structure (XANES) analysis.[67] For example, the short-range structural changes in the TiO_{2-x} switching layer[68] and the intermediate nanoscale oxide layers that spontaneously form at the Me/MO_x interface (where Me = Ti, Hf, and Ta, and MO_x = Ta_2O_5, HfO_2, and SiO_2)[69] were observed by comparing electron momentum-weighted oscillation spectra, $k^2\chi(k)$ in EXAFS, as shown in Figure 6e. The observed dependence of the electrode oxidation rate on the oxide's thermodynamic stability and the metal's oxygen affinity in ref. [69] was found

 © 2017 WILEY-VCH Verlag GmbH & Co. KGaA, Weinheim

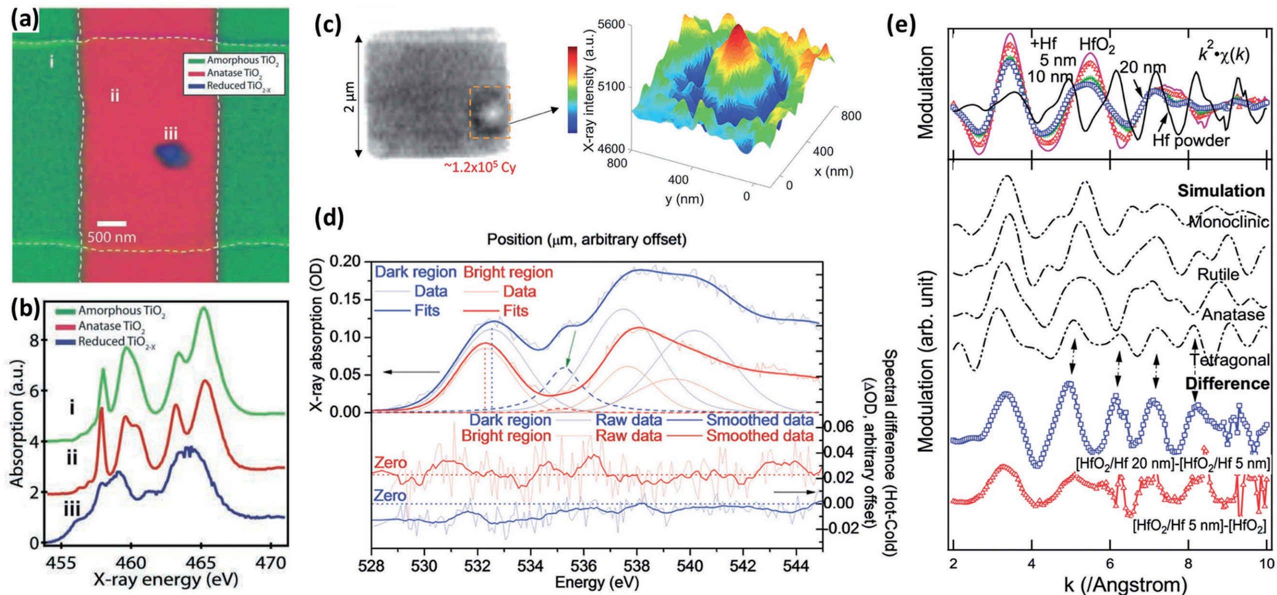

Figure 6. a) Scanning transmission X-ray microscopy (STXM) image of a TiO_2-based device after electrical cycling, showing structural changes and the formation of a localized channel.[50] b) Corresponding Ti L-edge X-ray absorption spectra from the three regions in panel (a); stoichiometric amorphous TiO_2 (green), stoichiometric anatase TiO_2 (pink), and reduced TiO_{2-x} (blue). Reproduced with permission.[50] Copyright 2010, John Wiley and Sons. c) O K-edge X-ray transmission intensity map (left) and 3D intensity plot (right) of a Ta_2O_5-based device after 120 000 electrical cycles. A ring-like feature with a bright core and a dark perimeter, corresponding to low and high O concentrations, respectively, is observed.[52] d) Upper panel: O K-edge absorption spectra from the bright (red) and dark (blue) regions, showing the downshift of the lowest conduction band position (indicated by vertical dotted lines) in the bright region leading to a higher electric conductivity. Lower panel: O K-edge spectra difference between the hot and cold states (corresponding to with and without current flow, respectively) from the bright and dark regions. More recognizable changes are observed in the bright region, indicating that current mainly flows through the bright region. Reproduced with permission.[52] Copyright 2016, John Wiley and Sons. e) Upper panel: $k^2\chi(k)$ spectra of HfO_2 (30 nm)/Hf (5,10, and 20 nm) samples with a reference of Hf powder. Lower panel: simulated $k^2\chi(k)$ spectra for different crystalline structures including monoclinic, rutile, anatase, and tetragonal, revealing that the local structure of the HfO_2 main matrix is monoclinic-like. The $k^2\chi(k)$ difference (e.g., [HfO_2/Hf 20 nm] – [HfO_2/Hf 5 nm] and [HfO_2/Hf 5 nm] – [HfO_2]) is most similar to that of the tetragonal structure instead of monoclinic, suggesting that the interfacial oxide has a different local structure from the matrix oxide. Reproduced with permission.[69] Copyright 2017, American Chemical Society.

to be consistent with the RS behaviors of Ta_2O_5-based devices with different electrodes, as well as predictions from first-principles calculations.[70] More importantly, this sensitive technique helps point out the role of the interfacial oxide layer as an oxygen reservoir in mediating reliable ionic migration, and the mechanism of device failure due to the transition of short-range ordered interfacial oxide toward disordered main oxide matrix.[69] In another study, chemical dissolution of Ag into a GeS_x electrolyte accompanied by Ag ionization was revealed through XANES analysis,[71] which is known to be sensitive to local chemical bonding and thus the metal's oxidation state.[67] Specifically, higher-energy shift was observed in the peaks of XANES derivative spectra from an Ag/GeS_x film compared to an Ag foil, whereas data from an Ag/SiO_2 film showed no change compared with the Ag foil.[71] This observation indicates that the valence number of Ag in SiO_2 is null (e.g., Ag exists as elemental Ag^0) while Ag in GeS is positively charged, implying that not only metallic Ag atoms but also the formation of the conductive Ag–Ge–S ternary compound may account for the RS behavior in chalcogenide-based ECM devices.

3.2.2. X-Ray PEEM Analysis

Besides binary oxides, complex perovskite oxides such as $SrTiO_3$ are also known to exhibit resistive switching behaviors based on the redistribution of oxygen vacancies.[72,73] Nanoscale redox reactions in $SrTiO_3$ were verified by X-ray PEEM (XPEEM) analysis in a device with a graphene top electrode that provides both electrical conductivity and photoelectron transparency to allow electrical programming and spectromicroscopy measurements simultaneously in situ, in a nondestructive fashion.[54] When the device was switched between the LRS and the HRS, noticeable differences were observed in PEEM images in localized areas (**Figure 7**a,c), which can be attributed to the formation/dissolution of a conductive filament. A lower O concentration in the LRS was observed from the O K-edge spectra (Figure 7b,d) compared to the HRS, revealing the correlation between the changes in electric properties and the chemical composition modulation, controlled by in situ electric stimuli. In addition to O migration, redox reactions involving changes of the cation valence state (e.g., $Ti^{4+} \leftrightarrow Ti^{3+}$) were verified, by comparing the relative spectra intensity at different photon energies that are sensitive to specific Ti oxidation states. Specifically, the Ti^{3+} concentration decreases after the reset process and increases again after the set process, as shown in Figure 7e, indicating the valence state change of the Ti ions induced by the O-ion migration during resistive switching. Similar results are also consistently observed in other studies.[50,53,55] On the other hand, even the HRS does not show the same spectra as in the reference area, as shown in Figure 7d, indicating the

 © 2017 WILEY-VCH Verlag GmbH & Co. KGaA, Weinheim

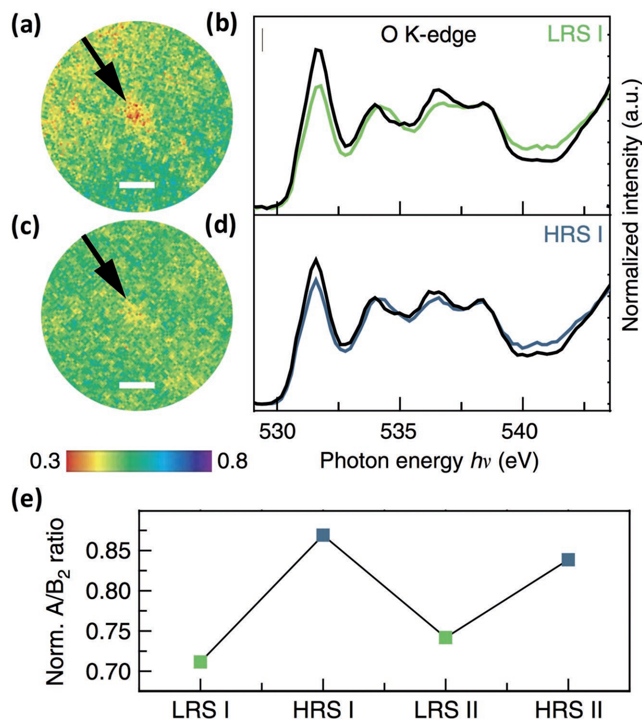

Figure 7. a,c) XPEEM images of an $SrTiO_3$-based device in a) LRS and c) HRS, showing a localized filament with changes of the O concentration. Scale bars: 1 µm. b,d) O K-edge spectra obtained from the filament region (green curve for LRS in panel (b) and blue curve for HRS in panel (d)) and the surrounding region (black curves). e) Normalized A/B_2 ratio, which is inversely proportional to the Ti^{3+} concentration, in different device states, indicating the valence change of Ti ions induced by O migration during the resistive switching process. Reproduced with permission.[54] Copyright 2016, Nature Publishing Group.

incomplete restoration during the reset process in oxide-based devices. Due to the considerable amount of oxygen vacancies left in the switching layer, which cannot be completely removed, the resistance of the off-state in oxide-based devices is much lower than in the prior-forming virgin state, leading to a small memory window as discussed earlier.

3.2.3. C-AFM Analysis

Besides, direct observations of changes in the switching material's composition (e.g., Ag/Cu injection in electrolytes or cation/oxygen ratio in oxides) and chemical states (e.g., oxidation state of cations in oxides), changes in material properties such as the local electrical conductivity can be measured by the 3D C-AFM tomography technique. 3D conductivity tomography is based on scraping the material of interest layer by layer through a conductive diamond tip in a C-AFM setup, allowing the local conductivity of the film to be revealed even for regions normally buried under an electrode, as schematically shown in **Figure 8**a. Figure 8b,c shows 3D conductivity tomography results obtained in a Cu/Al_2O_3 device in the LRS and the HRS, respectively.[26] Due to the high spatial resolution of the scanning probe microscopy and the sub-nanometer precision in the material removal process, the shape and size of the conductive filament can be accurately determined with nanometric resolutions in all three dimensions. Specifically, conductive filaments observed in the Cu/Al_2O_3 device exhibit a conical shape with the narrow constriction formed close to the inert electrode (Figure 8d), consistent with observations through earlier TEM studies and predictions from the electrochemical theoretical framework discussed in Section 3.1.1.[31,32] The ruptured region of the filament in the HRS (Figure 8c) was found to be near the inter-electrode interface, as expected from the geometry the filament since rupture is expected to occur at the narrowest region of the filament. These results identify the actual physical location of the switching events, and are critical for continued device optimizations. The scraping C-AFM technique was also successfully employed for oxide-based VCM devices (Figure 8e).[56] Specifically, direct measurements from the 3D conductivity tomogram verified that the conductive filament size can be controlled to be less than 7×7 nm^2 in an Hf/HfO_2 device, by controlling programming conditions such as the current compliance as shown in Figure 8e, thus supporting the excellent scalability offered by RRAM devices below the 10 nm regime as demonstrated in previous studies.[74,75]

3.3. Theoretical Simulations and Modeling

Accompanying the experimental findings, modeling efforts with different levels of physical details have been performed to examine the underlying physical processes in these coupled ionic/electronic systems. These models in turn help predict the device switching characteristics and provide the needed insights toward continued device and material design and optimization.

Recent atomistic simulations,[76,77] based on molecular dynamics, provide a feasible physical picture for the ECM devices during RS processes. The simulation implemented reactive interatomic potentials, including the effects of electrostatic potential on partial atomic charges, to describe the complex chemical reactions involved in the RS process beyond conventional molecular dynamics approaches.[78,79] Upon the application of a set/reset voltage, the formation/rupture of a conductive bridge connecting the two electrodes was successfully observed,[76,77] as shown in **Figure 9**a,b. More importantly, the growth of the filament by the progressive reduction of dissolved Cu ions was observed during the forming process (Figure 9c–f), which is consistent with experimental observations in systems with fast ionic transport.[31] During reset, the filament became ruptured in the proximity of the inactive electrode as a result of the dissolution of Cu atoms connected to the positively biased electrode (Figure 9g–i), again supporting earlier experimental results on the location of the filament rupture.[31] The concentration of Cu ions in the SiO_2 electrolyte increases in the gap region after the initial forming and reset cycle, which facilitates the re-construction of a new filament at a lower voltage during subsequent set processes, again consistent with widely reported experimental findings.[2,26,31,60] Additionally, simulations on the atomic trajectories during the atomic reconfiguration provide insight into critical kinetic parameters that allow stable switching at nanoscale. For example, the aggregation of Cu atoms with more than three metal–metal bonds leads to metallic clusters and subsequently stable filaments by the

 © 2017 WILEY-VCH Verlag GmbH & Co. KGaA, Weinheim

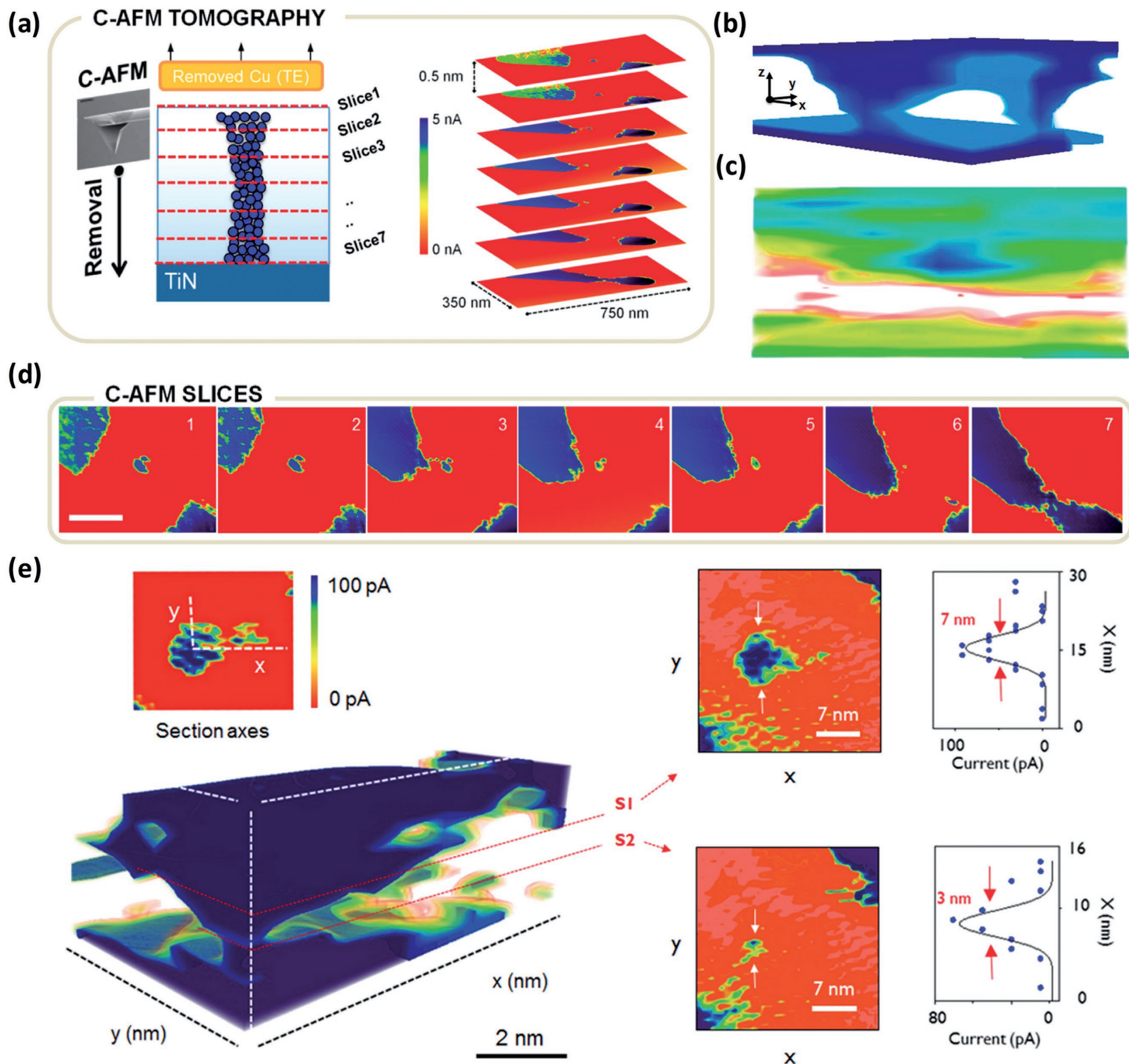

Figure 8. a) Schematic illustration of the 3D C-AFM tomography technique, showing the layer-by-layer scraping and the 2D C-AFM image slices collected at different heights. b,c) Reconstructed 3D C-AFM tomogram of a Cu/Al_2O_3-based ECM device, at b) LRS and c) HRS. d) A set of 2D C-AFM slices used for the 3D reconstruction, indicating a CF having a conical shape with the narrow constriction close to the inert electrode. Scale bar: 80 nm. Reproduced with permission.[26] Copyright 2014, American Chemical Society. e) 3D C-AFM tomogram of an HfO_2-based VCM device, and C-AFM spectra indicating the sub-10 nm size of the CF. Reproduced with permission.[56] Copyright 2015, American Chemical Society.

percolation of the clusters, while single-atom-chain bridges are found not to be thermodynamically stable in this SiO_2/Cu system, probably due to the low activation energy for Cu migration.[76]

Atomistic simulations based on molecular dynamics and first-principles calculations using density functional theory have also been performed to investigate the physical processes during VCM device switching. The changes in electronic structure induced by the modulation of oxygen vacancy concentration in Ta_2O_5 were confirmed by density-of-state calculations using amorphous cells having different stoichiometry.[80,81] Additionally, a V_O-rich region providing continuous conduction path for electrons was observed in a cell with low O concentration.[81] Attractive cohesive interaction between oxygen vacancies was found in TiO_2, supporting experimental observations of a conductive Vo-rich filament with *Magnéli* phase and ordered vacancies.[40,82] In addition, first-principles calculations have been performed to calculate important thermodynamic and kinetic factors such as the V_O formation energy and the migration barrier more accurately, without using empirical parameters as a priori. The calculated formation energy for oxygen vacancies and the migration barrier in various oxides show good agreement with experiments,[83–86] providing not only clear theoretical basis for the roles played by oxygen

 © 2017 WILEY-VCH Verlag GmbH & Co. KGaA, Weinheim

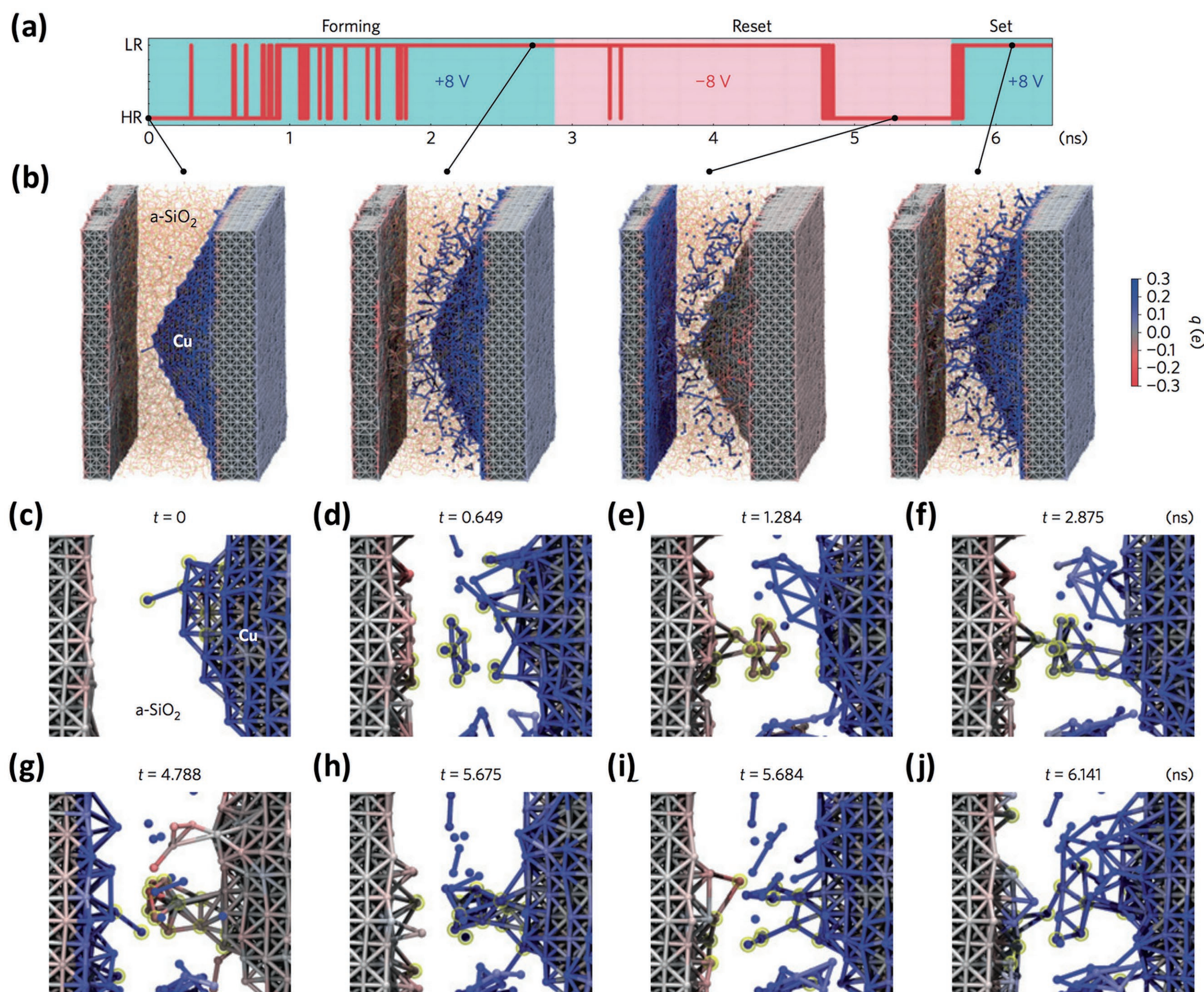

Figure 9. a) Evolution of the cell state for a Cu/SiO_2-based simulation cell between low resistivity (LR) and high resistivity (HR), under forming/set (cyan color) and reset (pink color) bias conditions. b) Snapshots of the atomic configuration at different moments in panel (a). c–j) Zoomed-in snapshots during the c–f) forming/g) reset/h–j) set processes, showing the connection/disconnection of the two electrodes by the formation/rupture of a Cu-based CF upon voltage biases with opposite polarity, supporting experimental observations. Reproduced with permission.[76] Copyright 2015, Nature Publishing Group.

vacancies but also guidelines for device design and optimization. For example, the predicted effects of the filament growth conditions (e.g., the oxygen chemical potential and thus the vacancy formation energy) from theoretical calculations were successfully implemented to experimentally engineer devices with improved *I–V* characteristics by selecting proper materials as the reactive electrode.[70,87]

Although the atomistic simulations are based on accurate underlying physical processes, the spatial and temporal scales analyzed in the simulations are normally experimentally unattainable. For example, the dynamical evolution of the atomic filament configuration was simulated within a very short time, approximately in nanoseconds.[76] Additionally, comprehensive, atomic-level descriptions of VCM devices that can capture all relevant dynamic processes and can be closely linked to experimental observations still remain to be developed. On the other hand, macroscopic-level, phenomenological models that can quantitatively describe resistive switching behaviors in oxide-based devices have been extensively studied. By solving a set of partial differential equations (i.e., ionic drift/diffusion and continuity equation for ion transport, electronic continuity equation for current conduction, and Fourier equation for Joule heating), the dynamic switching processes including the evolution of the atomic configurations and the associated conductance changes can be reliably modeled.[88,89] The obtained *I–V* characteristics from a simulated cell that mimics the actual device structure (**Figure 10**a) exhibit remarkable agreement with the experimentally measured data, as shown in Figure 10b. Dynamic switching processes including the depletion of oxygen vacancies close to the top electrode during the reset process, and the refilling of the gap during the set process, were accurately captured as shown in the V_O concentration profile (Figure 10c,d). In addition to binary resistive switching, rich phenomena based on controlled oxygen vacancy redistribution, such as multiple

 © 2017 WILEY-VCH Verlag GmbH & Co. KGaA, Weinheim

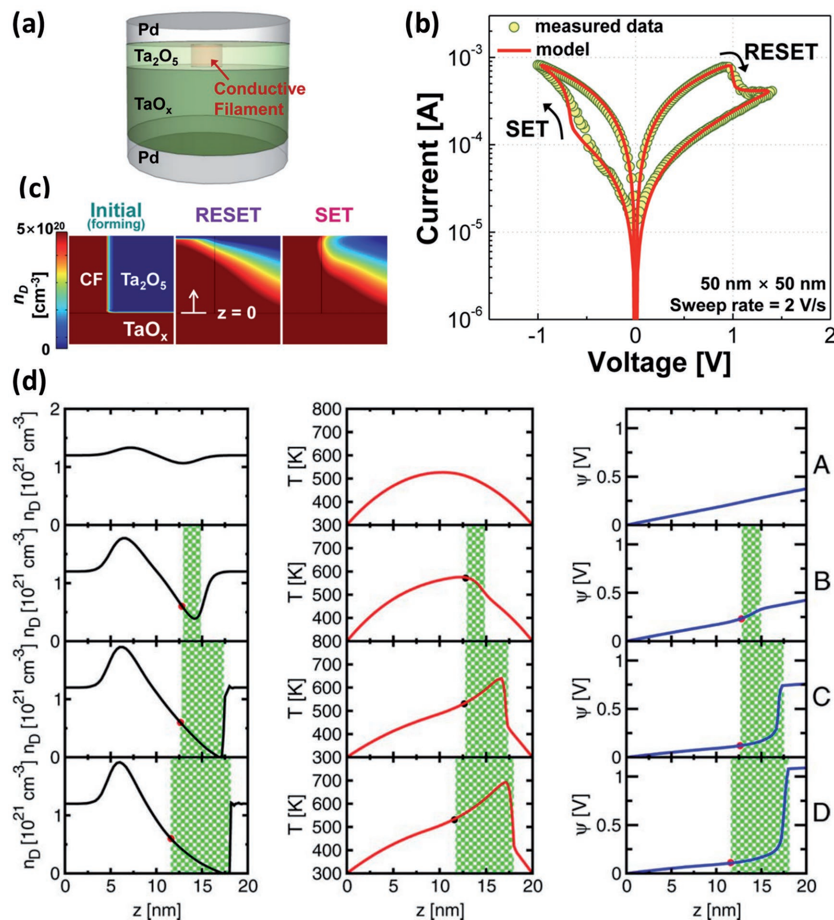

Figure 10. a) Schematic of a simulation cell having a Ta_2O_5/TaO_x bilayer structure. b) *I–V* characteristic during RS, showing good agreement of the model (solid lines) with experimental measurements (circles). c) Calculated 2D V_O concentration profiles in the initial state, HRS and LRS. Reproduced with permission.[89] Copyright 2014, American Chemical Society. d) Calculated 1D profiles of the V_O concentration, temperature, and electrostatic potential at different states of another model VCM cell. Evolution of the depletion gap, defined as the region where the V_O concentration is lower than 6×10^{20} cm^{-3}, is indicated by the shaded area. Reproduced with permission.[88] Copyright 2012, IEEE.

conductance states for multilevel storage, analog conductance modulation that is useful for neuromorphic computing, and complementary resistive switching[90,91] effects, can be accurately captured in the model and used to support experimental findings.[92]

The rich and controlled dynamic processes observed in coupled ionic/electronic systems make these devices promising candidates as a reconfigurable platform for multifunctional devices and circuits. A broad range of material and device parameters, e.g., the ion migration activation energy, ion hopping distance, electrode material, and oxide stoichiometric/thickness, which can affect the RS characteristics have been examined in simulations and experiments, through techniques such as controlled doping,[93] interface/stack engineering,[94] and control of the electrical forming process.[95] In addition, the role of Joule heating was extensively analyzed during the operation of VCM devices. The heat generation inside the filament due to Joule heating, as shown in Figure 10d, can greatly facilitate thermally activated processes including ionic diffusion and drift, and can thus be further utilized to improve the RS characteristics such as the dynamic range of the device.[96] Additionally, utilizing the internal ionic dynamics may allow realistic emulation of synaptic behaviors in these solid-state devices, including activity-dependent synaptic plasticity where the local temperature acts as a short-term state variable (discussed in more detail in Section 4.2.4).[97]

4. Applications

4.1. Resistive Switching Devices: Memory

The most obvious application of the conductance modulation effect is in the form of RRAM for nonvolatile, high density, and fast data storage. RRAM devices are an attractive candidate in applications such as storage-class memory, by potentially combining the desirable characteristics of dynamic random-access memory (DRAM) and flash memory and bridging the performance gap within the memory hierarchy.[1,3,4,98] Specifically, in RRAM the resistance change is associated with material reconfiguration driven by redox reactions and ion transport that can be exponentially accelerated by electric field and/or temperature during programming.[88,89] This extremely nonlinear response to stimulation ensures that the new atomic-configuration state will remain unchanged when the voltage bias is removed or under low-bias read conditions, thus enabling the devices' ability of both fast programming (within nanoseconds) and long data retention (years). Indeed, sub-nanosecond switching speed[99,100] and decades long retention time[34,101] along with other excellent performance metrics, e.g., large on/off ratio,[25] low energy consumption,[18,19] and high endurance[33,34] have been demonstrated. Extensive research efforts have been made to further improve the performance of RRAM devices for very large scale, practical applications in the last decade, and continued device optimizations are still currently underway.

4.1.1. Device Variability

One of the most challenging issues in device-level research is to improve the device uniformity, for both ECM and VCM devices. Specifically, RRAM devices are inherently stochastic during the resistive-switching process, originating from the stochastic, thermally activated ion migration and redox processes. These stochastic effects lead to temporal variations,[102] in which the switching time or switching voltage is broadly distributed from cycle to cycle even for the same device.[103,104] The stochastic growth of the filament, combined with the disordered nature of

 © 2017 WILEY-VCH Verlag GmbH & Co. KGaA, Weinheim

the amorphous switching material, also results in large device to device variations. To minimize bit errors during programming, feedback schemes that verify the device state after each programming operation, or excessive programming voltage/pulse width conditions can be used at the expense of system speed or device reliability, respectively.[105] In addition, device variations can arise from nonideal fabrication processes such as inhomogeneous film thickness, film stoichiometry, and line edge roughness, which can be mitigated through tighter process control.[104]

Engineering of the switching materials and the device structure has been extensively carried out to improve RS uniformity. Doping of the oxide layer in VCM devices, such as Al,[106] Gd,[107] and Ge[108] doping in HfO_2, has been reported to result in narrower distributions of the HRS/LRS resistance and the forming, set, and reset voltages. Dopants can lower the oxygen vacancy formation energy, and thus oxygen vacancies are likely to be formed near the dopants instead of randomly, thus help confine the V_O filament formation to the same location among cycles and improve cycle-to-cycle uniformity. Improved uniformity in the operating voltages and resistance states was also achieved by introducing nanodots[109–111] and nanocone-shaped electrodes.[112] The concentrated electric field resulting from these engineered nanostructures can help guide ion transport and redox reactions, thus suppressing random and uncontrolled filament growth.[109] The effect of filament confinement on device uniformity was also verified in a graphene-inserted RRAM device, where ion transport is allowed only through an engineered nanopore in the graphene film working as an ion-blocking layer, leading to a confined/controlled filament with improved device variations.[49,113]

4.1.2. Memory Window and Set/Reset Current in VCM Devices

Other crucial parameters that need to be further optimized for RRAMs, particularly VCM devices, include the set/reset current and the memory window.[114] Relatively high operation current (approximately milliampere) and small on/off ratio $\left(<\approx 10^2\right)$ are typically observed in VCM devices. A lower operation current is desirable not only to achieve low power consumption but also to mitigate the series resistance issue from the interconnect wires in high-density arrays, and to relax the current driving capability requirement of the programming circuitry and the selector element;[19] while a larger memory window with high on/off ratio relaxes device variation requirements and allows larger arrays to be built.

Multilayered device structure may be used to reduce the operating current, in which additional semiconductors or dielectric layers are inserted in the device stack to control the supply of oxygen vacancies or to act as a barrier layer. For example, an asymmetric and gradual profile of V_O chemical potential was obtained by employing multiple oxide layers with different O-scavenging effects, leading to the confined filament formation with lower current levels.[115,116] A reduced operation current was also observed when the supply of oxygen vacancies is limited only through an engineered nanopore in a graphene layer, in which the operation current was found to be directly proportional to the diameter of the nanopore.[49] Simply scaling the device size may also lead to lower operation current of VCM devices. Along with increased HRS resistance due to suppressed leakage current through the bulk film, higher LRS resistance values (>0.1 MΩ) were obtained in aggressively scaled devices,[74,75,117] especially when the device is scaled to the sub-10 nm dimension, i.e., comparable to the nanoscale filament size of ≈10 nm.[56] Following a similar concept, low-current operation of an HfO_2-based VCM device was demonstrated in a C-AFM-based structure, where the C-AFM tip serves as the top electrode having a sub-10 nm diameter.[118] It is important to note that in these cases, the on/off ratio is improved with significantly increased HRS resistance, contrary to cases of large-sized devices where a low programming current is obtained through current compliance, which typically leads to the degradation of the on/off ratio. Scaling the filament size by limiting the oxygen vacancy supply may further increase the HRS resistance since only a small number of V_Os need to be removed to completely restore the excellent insulating properties of the host material during reset (i.e., achieving a deep off-state)[118] thus resulting in a high on/off ratio that has been highly desirable but difficult to achieve in VCM devices.

4.1.3. Switching Reliability in ECM Devices

Even though the operations of both VCM and ECM devices originate from similar physical mechanisms, distinct RS characteristics are typically observed in these devices. For example, large memory windows and low operation current levels can be readily obtained in ECM devices, while such properties remain elusive for VCM devices, as discussed in the last section. Even with an ultralow programming current (≈1 nA), a Cu/Al_2O_3-based ECM device still exhibits excellent on/off ratio with good retention characteristics.[19,119] The feasibility of very low current operation in ECM devices can be attributed to the microscopic origin of the RS process, that is, the injected Cu and Ag cations do not chemically react with the host material in certain insulator-based switching layers and can thus be completely removed from the switching layer, leading to efficient recovery of the excellent insulator property at HRS. Indeed, although compounds may be formed in some solid electrolytes such as chalcogenides,[17,71] in insulator-based switching layers such as SiO_2 it has been found that the injected Cu and Ag cations exist as pure metal element instead of chemical compound. For example, selective area electron diffraction patterns of filaments in an Ag/a-Si device, and fast Fourier transformation patterns of an HRTEM image on nanoclusters in an Ag/SiO_2 device are indexed as elemental phase of Ag.[31,32] As a result, the deep off state provides sufficient on/off margin even in cases with a very low on-state current, in devices based on a barrier/tunneling layer or a partially formed filament using an external current compliance.[19,120]

On the other hand, the repeated insertion of foreign materials into the switching layer in ECM devices can potentially cause inevitable mechanical stress and result in deteriorated device reliability.[42] Indeed, the reported write/erase endurance of ECM devices is typically limited to the order of 10^6, comparably lower than that of VCM devices ($\approx 10^{12}$).[33,34] Improved endurance has been reported by introducing an additional layer such as

© 2017 WILEY-VCH Verlag GmbH & Co. KGaA, Weinheim

TiW,[121] Al_2O_3,[120] and graphene[122] in the device stack that prevents excessive cation injection into the switching layer. However, resolving the endurance and reliability issue still remains a critical challenge in ECM device development, particularly for logic-type applications where long endurance is needed.

4.1.4. Crossbar Arrays

A main feature of RRAM is the high storage density the device offers. Specifically, RRAM's simple, two-terminal structure enables device integration in a crossbar form with high density and high connectivity, having one device formed at each crosspoint in the crossbar, as shown in **Figure 11**a. In the crossbar structure, each device can be randomly accessed and the cell size is the minimum $4F^2$ (F representing the smallest feature size), allowing highest possible 2D density. Additionally, RRAM fabrication typically involves only a few additional steps, using low-temperature processes and materials that are mostly compatible with complementary-metal-oxide–semiconductor (CMOS) processes. This makes it possible to directly integrate RRAM arrays on top of CMOS circuitry in the same chip with low additional cost, as well as 3D-stacked memory structures with even higher density. Combined with the sub-10

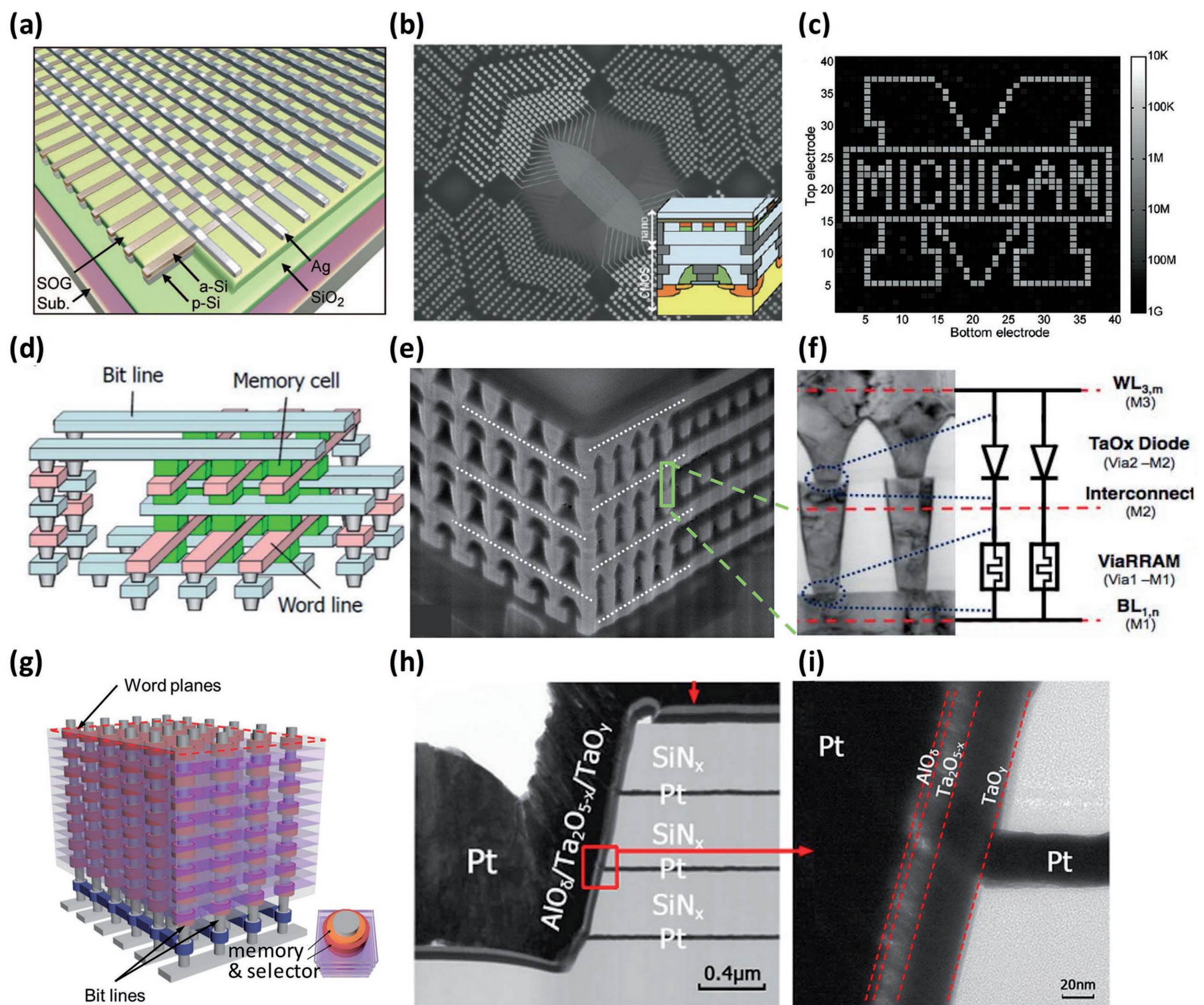

Figure 11. a) Schematic illustration of a crossbar array in which an Ag/a-Si/Si RRAM cell is formed at each crosspoint. Reproduced with permission.[21] Copyright 2009, American Chemical Society. b) Scanning electron microscopy (SEM) image showing a high-density crossbar array fabricated on top of a CMOS chip. Inset: schematic of the vertical integration of the RRAM crossbar array with the CMOS circuitry. c) A 1600 pixel bitmap image obtained by programming and retrieving data in the 40 × 40 crossbar array in panel (b). Reproduced with permission.[123] Copyright 2012, American Chemical Society. d) Schematic illustration of a 3D, stacked crosspoint structure. Reproduced with permission.[145] Copyright 2011, IEEE. e) SEM image and f) cross-sectional TEM image of a 3D stacked crosspoint RRAM array based on the ViaRRAM concept. A TaO_x diode is inserted in series with the RRAM element to reduce the sneak current. Reproduced with permission.[142] Copyright 2013, IEEE. g) Schematic illustration of the vertical RRAM structure. Reproduced with permission.[98] Copyright 2015, John Wiley and Sons. h) Cross-sectional TEM image showing two RRAM cells formed along the sidewall of a Pt bitline. i) Zoomed-in TEM image of an $AlO_\delta/Ta_2O_{5-x}/TaO_y$ sidewall device. Reproduced with permission.[149] Copyright 2014, Nature Publishing Group.

© 2017 WILEY-VCH Verlag GmbH & Co. KGaA, Weinheim

nm scalability discussed earlier, RRAM is generally viewed as a promising candidate for a broad range of applications from high-density data storage, hybrid CMOS logic circuits to portable/wearable electronics.[22,123]

Figure 11b shows an RRAM crossbar array directly integrated on top of a CMOS chip. Each Ag/a-Si switching element in the 40 × 40 array can be successfully programmed into two distinct resistance states with a read margin of at least 20× in the worst cases. Different 1600 pixel bitmap images were programmed in the 40 × 40 array through CMOS decoders underneath, and successfully retrieved, as shown in Figure 11c.

The successful operation of large-scale crossbar arrays requires the development of nonlinear "selector" devices to suppress leakage currents via sneak paths in the passive crossbar, along with optimized programming and read bias schemes.[124,125] Various selector devices based on mechanisms such as Schottky barriers,[126,127] crested tunneling barriers,[128,129] mixed-ionic-electronic conduction,[130] threshold switching[131] and metal–insulator transition (MIT),[132–134] have been proposed. These devices either show a rectifying behavior that suppresses the reverse current conduction or a very nonlinear *I–V* characteristic that suppresses leakage current in the low-bias regime. It should be noted that even though rectifying selectors are helpful during the read operation, they do not reduce power dissipation through the half-selected devices during the programming stage.[125] As a result, selectors with high *I–V* nonlinearity are preferred. Recently, large nonlinearity (10^{10}) has been reported in an Ag/HfO_2-based threshold switching device, with the formation of the Ag filament at high bias and spontaneous rupture at low bias providing the desired nonlinearity.[135,136] In addition, RRAM devices with intrinsic nonlinear characteristics, e.g., by adding a barrier layer in the device stack,[119,137,138] can simplify the fabrication process by not having to build a middle electrode.[127,135]

4.1.5. 3D Integration

To further improve the storage density, 3D integration of memory structures is necessary. 3D RRAM architectures can be achieved since only low-temperature processes are needed, and the device does not rely on a single crystalline substrate. There are generally two types of 3D architectures.[139] The first involves stacking multiple 2D crossbar arrays on top of each other, as shown in Figure 11d,e, in which the storage density increases as the number of stacked layers increases. The fabrication and functionality of 3D stacked structures have been demonstrated using Ag-based ECM devices,[140] polymer(polyimide:6-phenyl-C61 butyric acid methyl ester)-based organic resistive switching devices,[141] and TaON-based VCM devices.[142] To resolve the sneak current issue, a current rectifier, e.g., a TaO_x diode, shown in Figure 11f, was inserted in series with each RRAM cell in the crosspoint 3D structure.[142]. 3D stacking offers ultrahigh scalability with minimal changes to the fabrication processes. However, the number of lithographic steps and masks used in the process increases linearly with the number of stacks.[139,143]

As a cost-effective 3D architecture, the vertical RRAM structure was proposed.[144] In the vertical RRAM structure the metal–insulator–metal (MIM) cells are formed in parallel at the sidewall of a vertical electrode (Figure 11g–i). Several studies have demonstrated the feasibility of the proposed vertical RRAM structure, mostly based on transition metal-oxide-based systems, e.g., TaO_x,[145] HfO_x,[146] TaO_x/TiO_2,[147] WO_x,[148] and $AlO_\delta/Ta_2O_{5-x}/TaO_y$.[149] The integrated RRAM devices in the vertical structure exhibit typical resistive switching behaviors, e.g., >1000× on/off ratio, >10^{10} endurance, 10^4 s retention at 125 °C.[149] More importantly, good uniformity between devices at different layers was observed, supporting the feasibility of vertical 3D integration.[146,149] Since the electrode size in the vertical RRAM structure is determined by the width of the vertical electrode and the thickness of the horizontal electrode, potentially better scaling can be achieved since film thickness control during deposition is generally easier than pattern size control during lithography. For example, a graphene layer with atomic thickness has been employed as a horizontal electrode in a vertical RRAM structure, with improved power consumption due to the reduced device size.[150] Approaches to overcome the sneak current problem in vertical RRAM structures have also been carried out, using devices having intrinsic nonlinearity or self-rectifying behaviors,[147] or through the implementation of a vertical transistor[146] or a MIT-based selector[134] device.

4.2. Resistive Switching Devices: Synaptic Devices

4.2.1. Neuromorphic Computing Approaches

Beyond memory applications, an emerging, attractive field for resistance switching devices is bioinspired neuromorphic computing.[151–153] Nonconventional computing architectures are now being seriously considered since the current digital computing architecture, in which the central processing unit is physically separated from the memory, increasingly suffers from the von Neumann bottleneck problem resulting in the loss of energy efficiency and throughput due to intensive data movements. Furthermore, rapid advances in social networks, mobile devices, and sensors require efficient, real-time storage, and analysis of large amounts of data, while current hardware systems are not optimized for these data-intensive tasks. Neuromorphic computing systems, taking inspiration from the human brain, can potentially offer enormous computing capability through massive parallelism at extremely low power consumption and have attracted strong interest as a promising option in the search of new computing paradigms.[154–159] In this section, we will review recent progress in the development of neuromorphic computing hardware based on resistive switching devices. In particular, key requirements for practical emulation of biological elements and learning rules will be discussed, followed by discussions on recent network-level implementations of functional neuromorphic systems.

In these discussions, we will follow the memristive systems' theoretical framework, due to both fundamental arguments that this framework elegantly incorporates the native, internal dynamic processes of the device, as well as practical reasons that the analog switching characteristics, desired by neuromorphic computing systems, can be readily predicted and modeled using this approach.

 © 2017 WILEY-VCH Verlag GmbH & Co. KGaA, Weinheim

4.2.2. Memristive Systems Theoretical Framework

The concept of memristors and memristive systems was first proposed by Chua and further generalized a few years later by Chua and Kang.[12,13] In the generalized memristive systems' framework, the device dynamics are described mathematically as

$$v = R(w,i)\,i \tag{3}$$

$$\frac{\mathrm{d}w}{\mathrm{d}t} = f(w,i) \tag{4}$$

where v, i, and w are the voltage, current, and an internal state variable of the device, respectively. From Equations (3) and (4), it becomes clear that in a memristive system, the resistance cannot be determined directly by the instantaneous inputs (voltage and current). Rather, only the change of the device state can be predicted through the current state and the instantaneous inputs, as shown in Equation (4). As a result, the device's state (represented by variable w) is naturally history dependent. This simple but powerful mathematical description fundamentally explains the history-dependent hysteresis behaviors observed in RS devices, and implies that the inherent memory effect is a distinct feature of a memristive system.

The memristive framework started to draw significant attention after the work by HP laboratories in 2008 that directly linked the experimentally observed RS effects in a TiO_x-based device with the memristor concept.[14] Specifically, the device was modeled as two resistive elements connected in series, corresponding to the V_O-doped region and undoped region, respectively, with an adjustable boundary. In this configuration, the thickness of the doped region considered as the internal state variable, which is, in turn, modulated by the electric-field-induced V_O migration. The dynamic, time evolution of the state variable in response to the applied voltage is mapped to the dynamic Equation (4) in the memristive system framework, and the device exhibits characteristic pinched hysteresis loops with a clear frequency dependence, as expected from the memristor model.

Beyond theoretical importance, the memristive device framework is a very flexible and powerful tool that can help guide the understanding and optimization of devices, as different I–V and dynamic equations, often complex and nonlinear, can be used in Equations (3) and (4) to accurately predict the device operation, along with properly identified state variable(s). For example, a model with two resistive elements in parallel was proposed to successfully describe the incremental, analog resistance changes often observed in oxide-based RRAM devices,[160] in which the conductive channel area was identified as the internal state variable that reflects the nature of localized conductive paths. Additionally, exponential ionic drift, instead of the linear drift model as originally used, was employed to more accurately capture the Vo migration dynamics at high fields, and a decay term can also be included in the rate equation (Equation (4)) to account for spontaneous, lateral diffusion of ions.[160,161]

Based on these analyses, it can be argued that all resistive switching devices can be modeled within the memristive framework by mapping the current (Equation (3)) and the dynamic (Equation (4)) to the corresponding physical processes during the device operation, with properly identified internal state variable(s).[162,163] It should be noted that the dynamic equation (Equation (4)) also often implies physical reconfiguration of the material, e.g., through the change of the conductive region length or area due to ionic transport, so that key features of memristive systems, such as incremental conductance changes and other history-dependent changes of the material's properties, directly reflect the reconfigurability of the system. Therefore, proper understanding and modeling of these dynamic processes are essential to effectively utilize the reconfigurable elements toward successful system-level implementations such as building efficient neuromorphic computing hardware.

4.2.3. Synaptic Plasticity Implementations

A biological network consists of interconnected neurons through reconfigurable connections–synapses, as illustrated in **Figure 12**a. The connection strength, the synaptic weight, can be strengthened (via potentiation) or weakened (via depression) depending on the neurons' firing patterns, e.g., spiking timing and rates. The synapse can retain the updated weight[164] from tens of milliseconds to a few minutes in the form of short-term plasticity,[165] and from minutes (and hours) to days (and months) in the form of long-term plasticity.[166–168] These effects, termed synaptic plasticity, are believed to play a critical role in the processes of learning and memory.[169] The ability of memristors to modulate their conductance and evolve into different states, dependent on the input history, makes these devices ideal building blocks as artificial synapses for hardware implementation of neuromorphic systems.[4,163,170–172] Additionally, analog-type switching, in which the device conductance changes incrementally in response to a series of input signals (spikes), allows simple implementation of online learning.[4,173] Such incremental conductance modulation effects, as shown in Figure 12b, were experimentally implemented in different types of memristive devices including WO_x, Ag/a-Si, Ta_2O_5, and Al_2O_3/TiO_2.[93,151,160,174]

Different synaptic learning rules including timing- and rate-dependent plasticity which enable the efficient operation of biological systems have been successfully demonstrated in memristors. For example, spike timing-dependent plasticity (STDP) is a critical biological phenomenon during learning, and states that the synaptic potentiation or depression depends on the relative timing of the pre- and postsynaptic neuron firings. Specifically, if the presynaptic neuron fires before the postsynaptic neuron, causality may exist between the two events, and the synaptic connection between the two neurons should be strengthened. Additionally, the potentiation effect is stronger if the firing events are closer (representing stronger causality). This timing-based synaptic plasticity rule has been emulated in several different memristive systems,[175,176] where carefully designed pulses are employed to convert the relative timing information from the spiking events to a parameter that

© 2017 WILEY-VCH Verlag GmbH & Co. KGaA, Weinheim

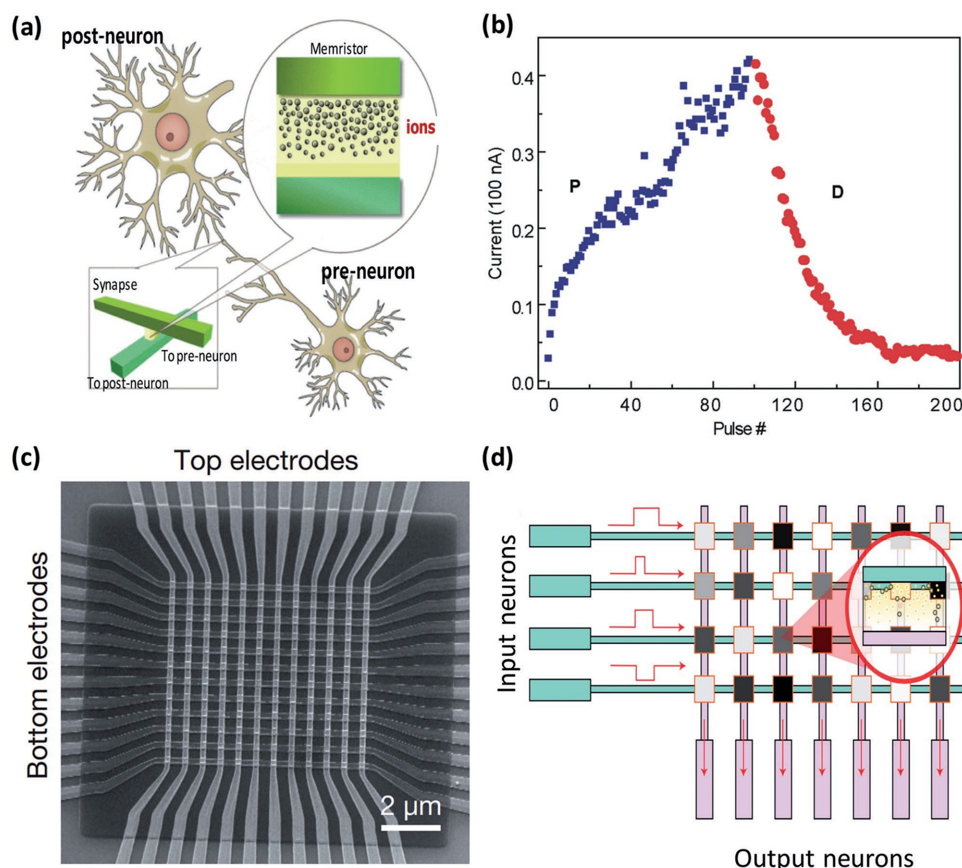

Figure 12. a) Schematic illustration of a memristor acting as a synapse bridging a pair of neurons, with the ability to gradually modulate the synaptic weight (conductance) by controlling the internal ionic configuration. b) Incremental conductance modulation of a memristor, in response to identical, consecutive potentiating (blue square) and depressing (red circle) pulses. Reproduced with permission.[151] Copyright 2010, American Chemical Society. c) A fabricated 12 × 12 memristive crossbar array used for classification of input patterns. Reproduced with permission.[174] Copyright 2015, Nature Publishing Group. d) Schematic illustration of an artificial neural network based on a crossbar structure, in which memristors acting as synaptic devices at each crosspoint regulate signals propagating through them. Reproduced with permission.[195] Copyright 2017, Nature Publishing Group.

can directly program the device, i.e., pulse height or duration, depending on the different overlap patterns of the pre- and postneuron pulses.

4.2.4. Biorealistic Emulation of Synaptic Effects

Beyond using the gradual conductance changes to emulate desired synaptic weight updates through engineering of the programming pulses, an intriguing alternative is to use the internal ionic dynamic processes in memristors to directly emulate the underlying physical and chemical processes in biological synapses, naturally at different time scales. This approach not only allows more biorealistic emulation, but also offers significant power advantages and enables direct processing of temporal, spiking inputs.[177,178]

For example, in biological synapses the timing information is naturally encoded internally, and spikes do not overlap with each other. In fact, spiking events are sparse (thus overlapping is very rare) and "sparsity" is a key factor that makes such systems so power efficient. Recent experimental and modeling efforts have shown that the internal dynamic processes within the synapse, e.g., the rise and decay of the Ca^{2+} concentration in short term, essentially provides an internal timing mechanism that enables the different timing- and rate-based synaptic functions observed experimentally.[179–181] Closer examination of the memristor model shows that similar internal dynamics can also be implemented in semiconductor memristive devices, where the (short-term) dynamics of one state variable can natively encode the relative timing information of the external stimuli, and eventually lead to the (long-term) change of another state variable that controls the device conductance, i.e., synaptic weight. These devices, with multiple state variables that evolve at different time scales, are termed "second-order" memristors and have been recently demonstrated experimentally.[97,182] In such a second-order memristor as illustrated in **Figure 13**a, the dynamics of the first state variable, such as the conductive channel area that directly determines the device conductance, is affected by a second state variable that evolves at a much shorter time scale, such as the internal temperature[97] and the oxygen vacancy mobility.[182] Similar to the Ca^{2+} dynamics in biological synapses, the rise and spontaneous decay of the short-term state variable provide an internal timing mechanism and allows the device to

 © 2017 WILEY-VCH Verlag GmbH & Co. KGaA, Weinheim

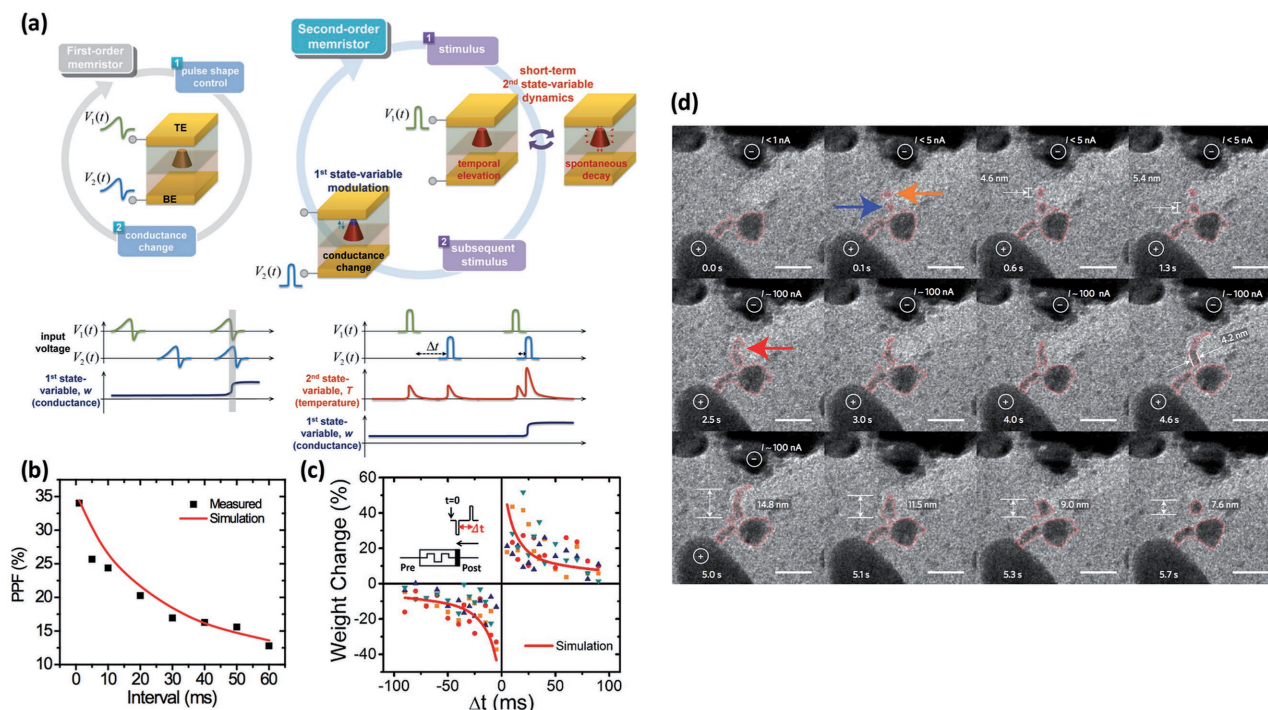

Figure 13. a) Conceptual illustration of the operation of a second-order memristor. Left: operation of a first-order memristor. The conductance is directly controlled by input voltage pulses. Right: operation of a second-order memristor. The input pulses drive the short-term evolutions of a second state variable, which in turn facilitates the evolution of the first state variable and modifies the device conductance. The internal short-term dynamics allows the device to naturally implement rate- and timing-dependent synaptic effects with simple, nonoverlapping spikes. Reproduced with permission.[97] Copyright 2015, American Chemical Society. b) A PPF results obtained from a WO_x-based memristor, showing interval- and frequency-dependent behavior analog to biological synapses. c) Weight change of the memristor device as a function of relative timing between the presynaptic and postsynaptic pulses, emulating STDP behavior with nonoverlapping pulses. Reproduced with permission.[182] Copyright 2015, John Wiley and Sons. d) In situ TEM images showing the field-driven filament formation ($t < 5.0$ s) and the diffusion-driven, spontaneous relaxation of the filament to nanoclusters ($t > 5.0$ s) in a diffusive memristor. Scale bars: 20 nm. Reproduced with permission.[136] Copyright 2016, Nature Publishing Group.

naturally emulate the rate- and timing-dependent synaptic effects, in a biorealistic fashion.

Experimentally, different synaptic functions at both short-term and long-term scales such as pair-pulse facilitation (PPF) and STDP have been directly implemented in a second-order memristor, without manually designed complex waveforms or overlapping pulses, as shown in Figure 13b,c.[182] The same concept was recently applied to a system based on two memristors, one with short-term dynamics (so-called diffusive memristor), which in turn modulates the second device with long-term conductance changes. The short-term dynamics in the diffusive memristor were directly observed from in situ TEM studies (Figure 13d), in which Ag nanoclusters were found to spontaneously diffuse and disperse due to interfacial energy minimization effects.[136]

The studies on second-order memristors and diffusive memristors reveal that rich internal dynamics can exist at different time scales in a memristor device, despite its simple appearance. Different physical processes involving ion drift, diffusion, chemical reactions, and Joule heating can be included in the dynamic equation (Equation (4)), and allow the device to exhibit diverse dynamic behaviors beyond simple conductance changes. The ability to directly and biorealistically emulate the underlying synaptic processes will likely, in turn, open the possibility of significantly extending the function and efficiency of hardware systems built with such dynamic devices.

On the other hand, the electrochemical processes during the memristor device operation can lead to chemical potential gradients arising from the Nernst potential due to the difference of metal (M) chemical potential from one interface to the other, the diffusion potential because of inhomogeneous distribution of M^{z+} and OH^- ions, and the Gibbs–Thomson potential due to the differences in surface free energy between the electrode and the nanoscale-sized filament.[183] These chemical potential gradients, formed in a nonequilibrium state during device operation, in turn introduce electromotive forces and result in the experimentally observed nanobattery effect.[183] Specifically, it can be argued that the electrochemical origin of the nanobattery effect resembles the electrochemical processes observed in neurobiological systems, and allows the solid-state ionic-based memristive devices to faithfully emulate the fundamental underlying physical and chemical processes in biological structures such as neurons and synapses, beyond what conventional electronic devices can afford.

4.2.5. Memristive Crossbar as Neuromorphic Network Hardware

An important feature of the cortical system is its large connectivity, enabling massively parallel processing. For example, the human brain has roughly 100 billion neurons with on

 © 2017 WILEY-VCH Verlag GmbH & Co. KGaA, Weinheim

average 7000 synaptic connections per neuron.[184] The two-terminal structure of memristive devices can potentially offer high connectivity, high density, and random access that are required to implement large-scale neuromorphic systems, in the form of memristor crossbar arrays. Indeed, a neural network can be readily mapped onto a crossbar structure as shown in Figure 12c,d. In this case, each input neuron (e.g., connected to a horizontal electrode) is connected to every output neuron (e.g., connected to a vertical electrode) with a memristor device acting as a synapse. Equally importantly, since current directly flows through the memristor between the input and output neurons, the "resistive" feature of the device allows it to directly modulate the information (in the form of current) flow through Ohm's law. In this sense, the device allows memory and computing functions to be performed simultaneously at the same physical location, without having to move data between different components.

Specifically, in a crossbar array, when input voltage pulses are applied to the rows of the crossbar, the output currents at the columns are determined by the product of the input voltage and the stored conductance values in the crossbar matrix. In this way, the memristor crossbar naturally performs the (input) vector-(stored synaptic weight) matrix multiplication operation,[163,170,174,185,186] a key operation in machine learning, analog computing, and other data intensive computing tasks. Note here that the vector-matrix operation is achieved directly "for free" through physical phenomena (e.g., Ohm's law and Kirchhoff's law, where the output is obtained via a single read of the output current), without having to perform computation and move data between separate processor and weight storage units. The ability to change the device conductance in situ, in turn, allows the network to adapt to the input patterns and learn useful features from the input data using online learning algorithms,[163,170,171,174] thus making the crossbar-based system a natural fit for mapping machining-learning and bio-inspired computing algorithms.

Experimental implementations of functional memristor-based neuromorphic networks have been recently demonstrated. In one example, a single-layer perceptron was mapped to a 12 × 12 crossbar array,[174] using carefully optimized Al_2O_3/TiO_2 stacks with nonlinearity and low forming voltages as synaptic devices. Classification of 3 × 3 black-and-white images into three classes, e.g., *z*, *v*, and *n*, was successfully demonstrated, as shown in **Figure 14**a–d. The neuromorphic network was trained online using a supervised training algorithm, using 30 input images including 3 ideal letters and 9 noisy versions of each letter. After applying each training pattern, the corresponding memristor conductance was updated using the Manhattan update rule,[187] a binary-quantized version of the batch-mode delta rule, as shown in Figure 14c. The weight update was performed in parallel for each column of the crossbar, validating the intrinsic parallelism of the crossbar-based

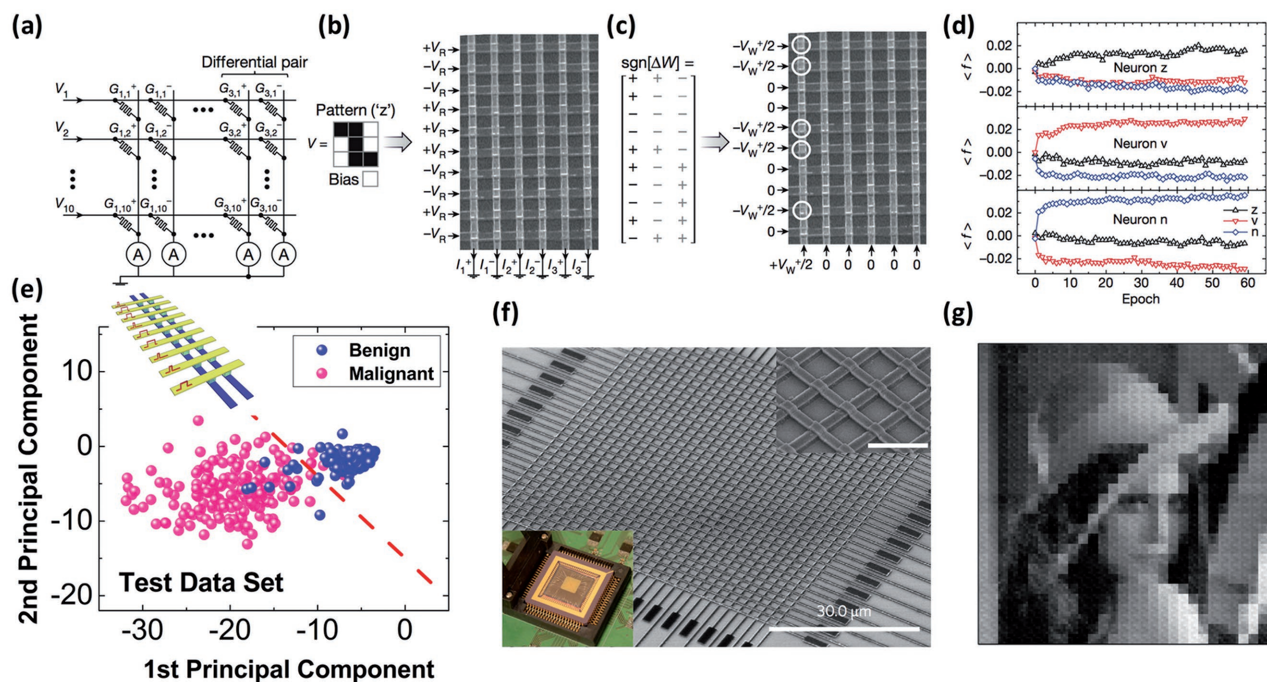

Figure 14. a–c) Illustrations of a neuromorphic network based on a 10 × 6 crossbar array, acting as a perceptron for pattern classification applications. d) Evolution of the output signals (f) experimentally obtained from the three output neurons in the perception, for different classes of inputs during training. Reproduced with permission.[174] Copyright 2015, Nature Publishing Group. e) PCA analysis results obtained in a memristor array after unsupervised training, along with a decision boundary (red dotted line) obtained using logistic regression. Inset: schematic of memristor-based network operation. The input voltage signals with different pulse widths are applied to each row, and the output current signals are collected from each column. Reproduced with permission.[190] Copyright 2017, American Chemical Society. f) SEM image of a fabricated 32 × 32 WO_x-based memristor crossbar array. Inset: magnified SEM image of the crossbar (upper right) and a wire-bonded memristor chip on the test board (bottom left).[195] g) An experimentally reconstructed image based on a sparse-coding algorithm implemented using the crossbar in panel (f). Reproduced with permission.[195] Copyright 2017, Nature Publishing Group.

 © 2017 WILEY-VCH Verlag GmbH & Co. KGaA, Weinheim

neuromorphic system during learning as well during inference. As shown in Figure 14d, all patterns were correctly classified after, on average, 23 training iterations, from6 training runs with different initial states.

In another example, a Ta_2O_5-based memristor network was used to perform principal component analysis (PCA)[188,189] by extracting features (e.g., the principal components) from sensory data and performing data clustering using unsupervised, online learning.[190] 9D unlabeled data, representing breast cell mass properties measured in nine categories from the University of Wisconsin Hospital, were mapped to a 2D output space using a 9×2 crossbar array (inset of Figure 14e) to separate benign cells from cancel cells. The two principal components were represented by memristor weights associated with the first two output neurons and obtained through online learning based on Sanger's rule.[191] After the unsupervised learning process, the memristor network successfully clustered the 583 test data points into two groups. With the help of a decision boundary obtained using logistic regression, the memristor-based hardware system achieved a classification accuracy of 97.1%, as shown in Figure 14e. These results, obtained experimentally from a small memristor network, are already comparable to results (97.6% accuracy) obtained from direct calculation of the eigenvectors in conventional PCA analysis. The high accuracy that can be obtained experimentally even in the presence of device variations further suggests that memristor-based neuromorphic hardware can indeed be reliably used for efficient feature extraction, using unsupervised, online learning algorithms.

A particularly attractive property of biological neural systems is their excellent energy efficiency in processing massive, complex data. Sparse coding, in which massive sensory inputs such as vision, auditory, and touch are represented by a relatively small set of strongly activated neurons, has been believed as an essential underlying mechanism by which biological systems can efficiently handle the large amount of high-dimensional data.[192–194] Experimental implementation of sparse coding algorithms was recently demonstrated in a memristive crossbar neural network based on WO_x devices (Figure 14f), in which the critical operations required by sparse coding, including pattern matching and lateral neuron inhibition, were effectively mapped on to the crossbar structure.[195] Specifically, input images were encoded by (sparse) output neuron activities, so that the input can be efficiently reconstructed using only a few active neurons and the associated dictionary elements stored in the memristor crossbar. Besides feedforward connections, lateral inhibition among all output neurons is a critical feature of sparse coding, as inhibition allows an optimal representation to be obtained, out of many possible representations.[196] According to Sheridan et al.,[195] lateral neuron inhibition was achieved by iterative forward and backward passes through the same crossbar, where the reconstructed input (obtained from the backward pass) is subtracted from the original input, thus essentially allowing active neurons to suppress other neurons that share similar dictionary elements. Careful analysis of the experimentally obtained network dynamics verified that the network can indeed find an efficient and optimal solution out of several possible solutions, while adjusting the sparsity parameter can balance the sparsity requirement and reconstruction accuracy. Finally, the system was used to successfully process natural images (120×120 pixels) as shown in Figure 14g, following predictions of the algorithm. These successful demonstrations clearly highlight the potential of memristive systems to process complex data with desired throughput and energy efficiency in demanding environments, and serve to stimulate continued device and system developments based on these nanoscale's physically reconfigurable components.

4.2.6. Continued Device Optimizations for Neuromorphic Computing

Successful, large-scale implementation of memristor-based neuromorphic networks critically depends on the device properties; thus, continued optimizations are still required beyond the initial demonstrations discussed above. Specifically, criteria for efficient logic operations such as neuromorphic computing are different from those for memory applications where the key is to be able to distinguish two stored states. For example, binary devices with large on/off ratio are ideally suited for memory applications, while analog-type switching devices are more desirable for neuromorphic applications. Such analog switching devices, unfortunately, typically exhibit smaller dynamic ranges (usually <10), which can cause systematic errors.[197] On the other hand, linear conductance modulation, where the conductance change can be predicted by the applied pulse width or amplitude, without prior knowledge of the current conductance value, is desirable for online learning implementations while practical devices typically show nonlinear, asymmetric conductance modulation characteristics. In a typical device, the conductance can be increased quickly from a state close to the HRS, and the rate of change will slow dramatically as the device approaches the LRS.[94,96] Combined with the device variation issue, the limited dynamic range and the nonlinear weight updates can significantly degrade the performance of memristor-based networks for neuromorphic applications,[173,197] with asymmetric nonlinearity of weight update having the most significant effect on the performance degradation while symmetric nonlinearity is less problematic.[198] Additionally, it has been shown that read noise due to thermal, $1/f$, and random telegraph effects, as well as write noise due to temporal variations can also degrade the network performance.[198] The high switching current (typically >100 μA) in typical analog-switching devices will, in turn, affect the system's power efficiency and limit the network size due to series resistance issues. Finally, forming-free memristor devices or devices with low enough forming voltages are required for reliable operation of the passive crossbar array. Otherwise, during the forming process, half-selected cells that are already formed may be exposed to a high voltage and can become damaged (e.g., stuck-at-1), even with carefully designed protective voltage schemes.[174,190]

These device optimizations will likely require synergistic efforts from materials scientists, physicists, chemists, and device and computer engineers, using systematic investigations starting from first-principles calculations and atomic-level characterizations that reveal the fundamental ionic processes and structural changes, to careful device engineering and

© 2017 WILEY-VCH Verlag GmbH & Co. KGaA, Weinheim

characterizations, and clever architecture design and optimizations that can maximally utilize the properties of the devices while sufficiently mitigating the device nonideality effects.

4.3. Resistive Switching Devices: Logic Applications

As the transistor size is approaching fundamental physical limits with diminishing returns on performance, alternative computing architectures including reconfigurable computing systems, analog computing, and neuromorphic computing have been extensively studied to extend computing functionality and increase the logic performance.[4,172,199] In the following sections, we discuss a few examples where RRAM devices have been used in these alternative logic computing applications.

4.3.1. Reconfigurable Logic Circuits

It has been demonstrated that RRAM crossbar arrays on top of CMOS circuits can serve as reconfigurable interconnects that wire up CMOS components so that different logic gates can be connected to form custom configurations, i.e., in the form of field-programmable gated array (FPGA) systems.[200] In this RRAM/CMOS hybrid FPGA system, RRAM devices can work as the configuration bits and switches in a data-routing network. The CMOS-compatible fabrication processes, small device/switch size, and nonvolatile functionality that helps eliminate power consumption for refresh make this approach attractive. Indeed, TiO_2-based RRAM/CMOS-integrated circuits with FPGA functionality were experimentally demonstrated.[200] Successful logic operations such as NOT, AND, NAND, NOR, and D flip-flop and, more importantly, reconfiguration of the CMOS gate connections were achieved by programming the states of the RRAM device overlaying the CMOS circuitry. Additionally, the defect-tolerant capability of the hybrid integrated circuits based on the redundant data paths in crossbar array structure was demonstrated as pointed by previous numerical simulations.[199,200]

4.3.2. Material Implication Logic

It is also shown that RRAM devices can be used for logic operations in which the resistance of the memristive switches was used to directly drive subsequent logic gates in the form of material implication (IMP) logic. IMP is a fundamental Boolean logic operation equivalent to (NOTp)ORq (p and q are logic variables), and was successfully executed with two memristive switches in 1×17 crossbar array.[201] In this implementation, logic values (i.e., "0" and "1") are represented by resistance of the memristive devices, and the IMP logic operation was achieved by applying voltage pulses resulting in different modulation of device resistance depending on the initial states of the two devices. Here, the conditional toggling properties for IMP were achieved through the voltage divider effect between the memristive devices and a carefully selected series resistor, with $R_{on} < R_{series} < R_{off}$, so that whether the state (resistance) of output device q can be modified depends on the state (resistance) of the input device p. Subsequently, the universal NAND operation was demonstrated using the IMP operation and an erasing operation in three interconnected memristive junctions.[201]

4.4. Beyond Resistance Change

The ability to directly change the materials' chemical composition through ionic processes allows a host of physical properties to be reconfigured, beyond electrical resistance changes. In principle, optical, magnetic, and mechanical properties of the material can also be potentially modified on demand, using simple electrical signals, thus offering tremendous opportunities in building multifunctional and reconfigurable systems. In this section, we discuss other functions that can benefit from material reconfiguration, involving changes in composition, structure, geometry, and chemical states induced by electrochemical reactions and ionic transport, and highlight the potential of these ionic systems as an important building block in multifunctional-embedded applications.[202–206]

4.4.1. Electrically Reconfigurable Optical Properties

In an ECM device, a new material, in the form of metal filaments, is created inside the host dielectric material during the RS process. As a result, the process can significantly alter the film's optical properties as well as electrical properties.

Plasmonic Memristor: In plasmonics, the signal is encoded as surface plasmon polaritons (SPPs) that propagate along a metal–dielectric interface with strong coupling with free electrons at the metal surface.[207] The SPP modes can be confined below the diffraction limit, offering potential for the implementation of nanoscale optical devices and circuits.[208,209] The built-in metal–dielectric interface in the MIM structure of RRAM devices makes RRAM devices naturally compatible with plasmonic circuits and can lead to devices such as plasmonic switches and modulators that provide coupled electro-optical memristive effects. These "plasmonic memristors" can open new opportunities for electro-optical system design and implementation, by offering low-power, electrically controlled, nonvolatile yet reversible optical modulations, beyond conventional electro-optical devices based on thermal,[210] free carrier dispersion,[211] and Pockels effects.[209]

In a recent study, an Ag-based ECM device was used as a plasmonic component that is directly integrated on a silicon-on-insulator (SOI) waveguide, shown in **Figure 15**a,b.[202] The propagated light through the waveguide is coupled to the fundamental plasmonic mode supported by the memristive device having an Ag-metal electrode, and thus different levels of optical transmission can be obtained depending on whether a metallic filament exists inside the a-Si layer, schematically shown in Figure 15c. Reversible electrical modulation of the optical signal with a clear optical hysteresis was demonstrated (Figure 15d). Here, the optical bistable behavior showing different optical transmissions is attributed to the changes of the absorption and scattering loss of the fundamental plasmonic mode due to the formation/annihilation of the lossy metal

© 2017 WILEY-VCH Verlag GmbH & Co. KGaA, Weinheim

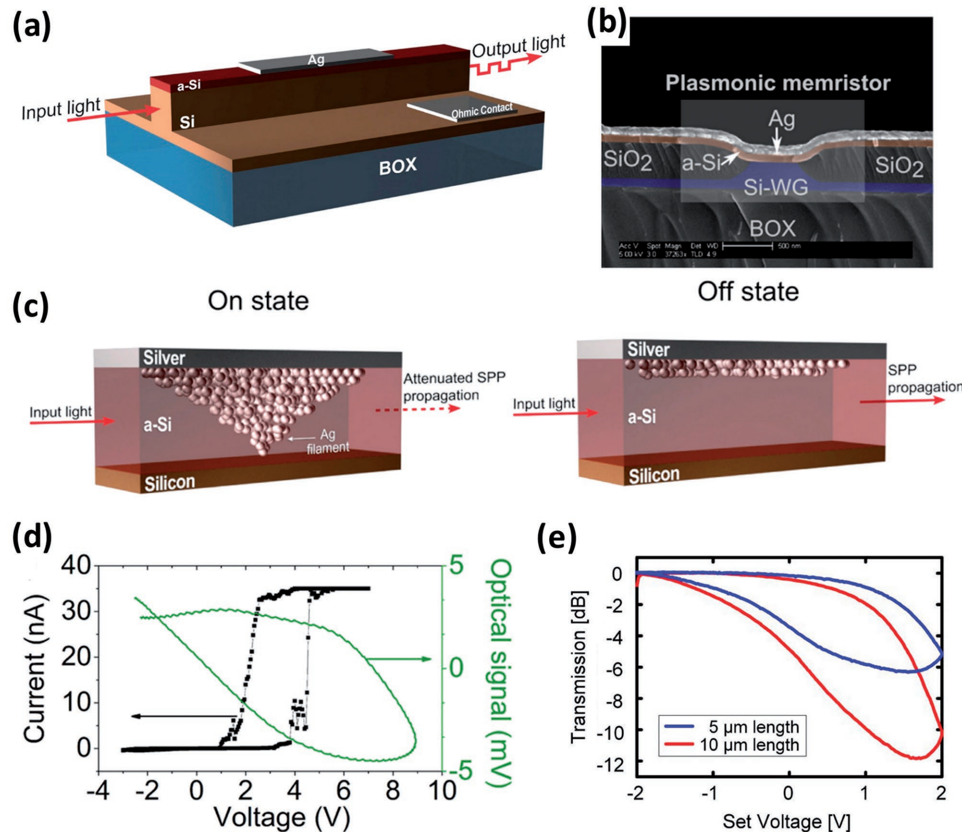

Figure 15. a) Schematic illustration of the plasmonic memristor structure with optical readout functionality. b) Cross-sectional SEM image showing an Ag/a-Si-based memristor integrated with an SOI waveguide. c) Schematic illustration of the plasmonic memristor. The formation (left)/annihilation (right) of an Ag-based conductive filament inside the a-Si electrolyte modulates the coupling of light with the plasmonic mode of the electrode, and thus light transmission through the waveguide. d) Correlation of the resistive switching *I–V* characteristics with the observed optical bistable behavior. Reproduced with permission.[202] Copyright 2013, American Chemical Society. e) Latching optical switching behavior with an extinction ratio of 12 dB (6 dB) in another plasmonic memristor. Reproduced with permission.[203] Copyright 2014, OSA publishing.

filament. In particular, by applying a write voltage, the ECM device is switched ON in which an Ag filament is formed inside the a-Si waveguide that increases scattering of the propagating light, leading to lower light transmission (Figure 15c, left). Note that since the plasmonic field is highly confined in the a-Si insulating layer of the MIM stack,[207] even minute changes of the insulating layer due to the formation of a nanoscale Ag filament can lead to measurable changes in transmission. After the application of an erase voltage, the transmitted optical signal recovers back to its initial value, due to erase of the filament and reduced scattering in the a-Si waveguide (Figure 15c, right). In a subsequent study, a high extinction ratio of 12 dB was demonstrated using a similar concept in a coupled plasmonic/memristive device, as shown in Figure 15e, demonstrating the functionality of plasmonic memristor (i.e., the electrical control of optical properties).[203]

Memory with Optical Readout Functionality: Plasmonic memristor with optical readout functionality can be utilized to couple information storage with optical communication, enabling optical readout (approximately picoseconds) that is much faster (approximately two orders of magnitude) than electrical readout and reducing the number of optical-to-electrical signal conversions in optical communication systems.[212] Recent experimental demonstrations of optical readout of an RRAM device integrated with an SOI waveguide, using a 1550 nm wavelength light system that is widely used in telecommunications, support the feasibility of this application.[202–204]

Latching Optical Switch: Another interesting characteristic of the plasmonic memristor is the latching behavior that is highly desirable for low power optical switch applications.[202,203] Specifically, since the optical modulation is based on the direct, atomic reconfiguration of the waveguide material that is both nonvolatile and reversible, latching optical switches, where the optical state can be maintained without constant energy consumption, can be achieved at the nanometer scale as shown in Figure 15d,e. The power consumption can thus be significantly reduced compared to conventional optical switches based on volatile switches that require a constant voltage supply.[207] Plasmonic memristors can also offer very low energy consumption during the switching process (e.g., 12.5 nW)[204] compared with devices based on thermo-plasmonic effects (e.g., 13.1 mW).[213] Optical modulators working in the visible range that can achieve reflectance changes up to 78%, operated within an ultralow voltage of 100 mV, have also been recently demonstrated in an $Ag/Al_2O_3/ITO$ device structure.[214]

 © 2017 WILEY-VCH Verlag GmbH & Co. KGaA, Weinheim

Atomic-Scale Optical Modulator: Historically, although electronic devices have been aggressively scaled down to nanometer and even atomic dimensions in the form of single-atom transistors and atomic switches,[215,216] photonic devices generally need to be much larger to allow sufficient light coupling and readout.[217–219] Recently, prototype photonic systems that can operate at the atomic scale have been developed by placing a single atom in a photonic cavity, which can enhance the weak interaction between optical photons and matter on the atomic scale.[219,220] In these demonstrations, atoms were delivered to optical resonators through slow laser cooling and magneto-optic trapping processes, requiring high vacuum and very low temperature. The ability to reliably move individual atoms at high enough speed, at room temperature in solid-state devices, will significantly help the development of nanoscale-integrated photonic circuits.

An atomic-scale optical switch was demonstrated by employing a resistive switching device showing conductance quantization.[204] The integrated Ag/a-Si/Pt memristive device in a planar structure on top of a silicon waveguide enables the creation of a plasmonic cavity by moving a single or at most a few atoms at the metallic tip between two planar electrodes, as shown in **Figure 16**a. The relocation of metallic atoms short-circuits the two pads and modifies the electric field in the junction, causing both resistive switching with quantized conductance and plasmonic switching (Figure 16b). Indeed, abrupt switching characteristics between two distinct plasmonic resonance states were observed in the device, acting as an atomic-scale optical switch, as shown in Figure 16c,d. Additionally, a blue-shift of the plasmonic resonance was observed in the LRS (Figure 16e) as a result of the reduction of the local field due to the presence of the filament, further confirming that the distinct plasmonic resonance states are a result of the atomic reconfiguration that accompanies electrical switching effects. Additionally, electro-optical switching in the visible spectra range with a very small active volume of (5 nm)^3, comparable to the sizes of modern electronic devices and much smaller than common optical devices, was demonstrated based on atomic reconfiguration in an Au/Al_2O_3/Ag device, as shown in Figure 16f,g, confirming the potential of nanoscale-integrated photonic circuits through material reconfiguration based on ionic effects.[221]

4.4.2. Electrically Reconfigurable Magnetic Properties

In spintronics, modulations of the materials' magnetic properties have been traditionally achieved using either external magnetic fields or induced fields from electric currents; neither is very scalable. More efficient control of magnetization has been recently achieved through the spin-transfer torque (STT) effect in ferromagnetic nanostructures such as those in a magnetic tunnel junction.[222–224] However, continued decrease of the current that drives the STT effect without sacrificing switching speed and data retention is still an ongoing task.[223,225] As a result, achieving magnetism control by means of an electric field (instead of current) is currently the focus of extensive investigation that can lead to higher speed,

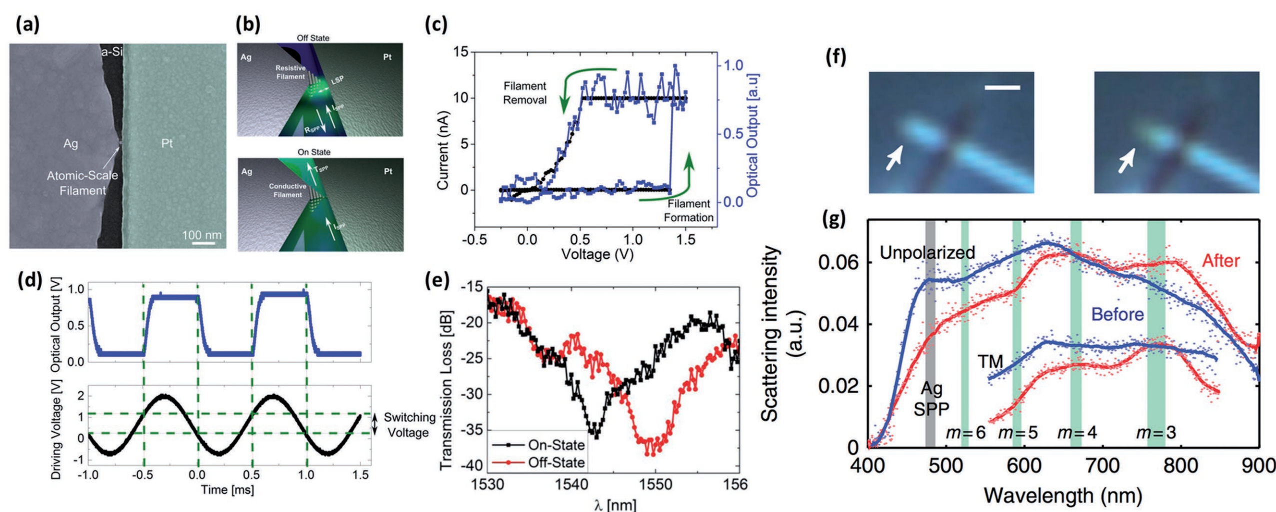

Figure 16. a) Top-view SEM image of a fabricated Ag/a-Si-based atomic-scale plasmonic switch with the electrically formed Ag filament. b) Schematic illustration of the operation of an atomic-scale plasmonic switch. The electrically controlled migration of a single or only a few atoms into a plasmonic cavity can short-circuit the two metallic pads and alter the plasmonic cavity resonance state. c) Resistive switching *I*–*V* characteristics (black circle) and the corresponding optical output transmission (blue square) that are simultaneously measured, indicating that the abrupt optical transition is correlated with resistive switching based on atomic reconfiguration. d) Optical response to a sinusoidal electrical input signal showing reversible, digital optical switching. e) Optical transmission as a function of wavelength showing two different resonance states, with a blue-shift of the resonance in the on state. Reproduced with permission.[204] Copyright 2016, American Chemical Society. f) Bright-field optical microscopy images of an Au/Al_2O_3/Ag-based memristive optical antenna before (left) and after (right) electrical switching. A change in color from blue to green is observed, suggesting that light scattering behaviors of the antenna are sensitive to even small changes in the junction as light is effectively concentrated through the excitation of surface plasmons. g) White-light-scattering spectra confocally obtained from the device before and after electrical switching. Noticeable changes in the resonant scattering responses are observed in both unpolarized and transverse magnetic (TM)-polarized spectra. Reproduced with permission.[221] Copyright 2016, Nature Publishing Group.

 © 2017 WILEY-VCH Verlag GmbH & Co. KGaA, Weinheim

lower power consumption, and improved reliability.[225–228] Electric field control of magnetism has been suggested through a number of magnetoelectric coupling mechanisms,[225] including carrier density modulation,[229] electron orbital occupation modulation,[226] and exchange coupling in multiferroics.[228,230] In addition to these magnetoelectric effects, the ability of direct, in situ, and on-demand modulation of the ferromagnetic materials through field-driven ionic processes (i.e., electric-field control of magnetism based on atomic reconfiguration) can offer potential for strong modulation, low-power, and nonvolatility, and can significantly broaden the potential of spintronic and magnetic materials and devices.

Magnetoionic Effect: In a recent study on a Co/GdO_x bilayered structure, sandwiched by electrodes (**Figure 17**a), bipolar, voltage-controlled annihilation and restoration of magnetic hysteresis were observed, as shown in Figure 17b.[205] The pronounced, nonvolatile changes in magnetic anisotropy energy (MAE) were attributed to the modulation of the metal–oxide interface by an electric field. Specifically, the oxygen concentration in the Co layer was reversibly modulated through field-driven oxygen ion migration during the voltage cycling, as confirmed through STEM–EELS analysis (Figure 17c). Changes in the oxygen concentration modulate Co's oxidation state and, in turn, the film's magnetic properties, leading to the observed modulation of the magnetic hysteresis. The magnetoionic effect can lead to changes in the interfacial magnetic anisotropy energy by >0.75 erg cm^{-2} at 2 V bias, outperforming efficiency achieved by conventional magnetoelectric coupling mechanisms.[205] The ionic transport nature was examined through temperature, voltage, and oxide thickness dependence, where faster switching speed was observed at higher temperature, under larger voltage, and in thinner oxides, consistent with the proposed mechanism. The localized, nondestructive magnetoionic coupling effect allows reversible tuning of the magnetic properties with excellent spatial control, unlike previous approaches that rely on irreversible ion-beam irradiation processes.[231,232] For example, localized laser heating facilitates ionic transport only in the illuminated area, enabling selective MAE programming as shown in Figure 17d. These results suggest a path toward electrical tuning of the interfacial chemistry in reconfigurable systems, allowing a broad range of physical and chemical properties to be modulated.

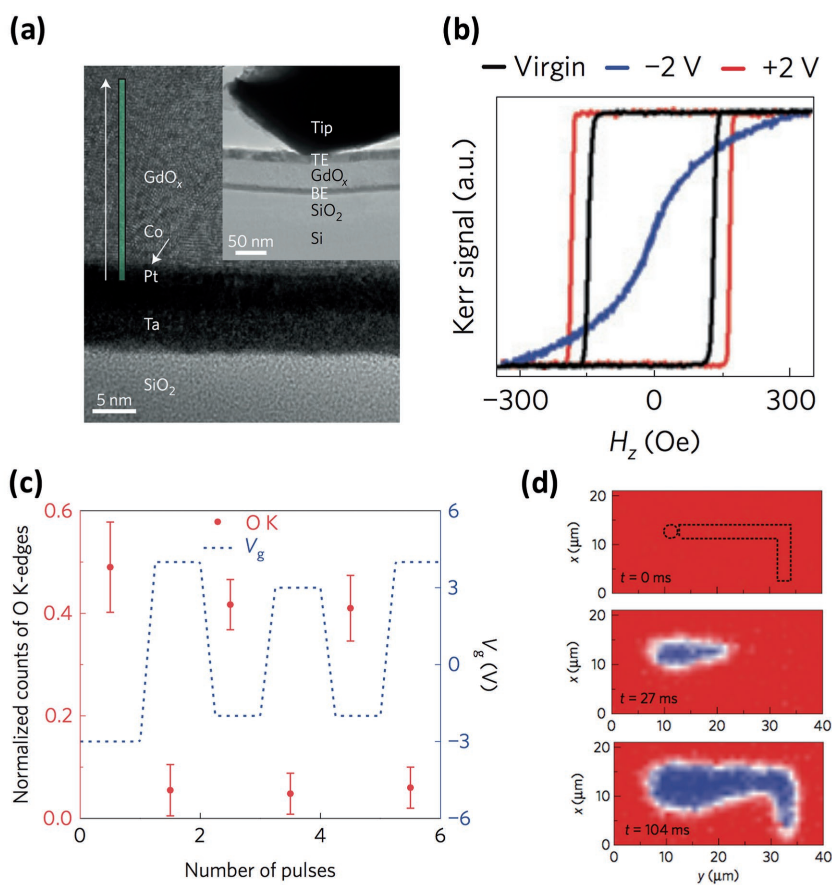

Figure 17. a) Cross-sectional TEM image of a device stack consisting of SiO_2/Ta/Pt/Co/GdO_x layers. Inset: the in-situ TEM measurement setup where a Pt/Ir probe is contacted to a device with a Ta/Au top electrode (TE) and Ta/Pt/Co bottom electrode (BE). b) Polar magneto-optic Kerr effect (MOKE) hysteresis loops measured from the virgin state and after the application of the negative and positive voltages at room temperature, showing the complete, reversible removal and restoration of the hysteresis induced by electrical stimuli. c) Normalized O K-edge EELS intensity measured in the middle of the Co layer (red circles) under the application of positive and negative voltage cycles (blue dot line) showing the reversible modulation of oxygen concentration. d) Time-resolved polar MOKE maps showing the evolution of domain expansion following a laser-defined pattern, due to the selectively enhanced ionic transport by laser heating. Reproduced with permission.[205] Copyright 2014, Nature Publishing Group.

Control of Magnetism beyond Interface/Surface: One distinct feature of the magnetoionic effect is the possibility of controlling magnetism in the bulk material, beyond the interface/surface in heterostructures. The aforementioned magnetoelectric effects such as charge-carrier modulation and orbital reconstruction are mostly limited to small regions of the material,[233,234] i.e., only a few monolayers in close proximity to the interfaces or surfaces, due to the short screening length in ferromagnetic metals[235] and semiconductors,[236] and the underlying mechanism based on interfacial chemical bonding, respectively.[225,237,238] On the other hand, it has been demonstrated that electrically induced ion migration and electrochemical processes modulate the materials' magnetic properties in the bulk form beyond the interfaces.[237,239,240] Reversible modulation of magnetic moments shown in **Figure 18**a was achieved by electrochemically driven lithium intercalation and de-intercalation in a ferromagnetic iron oxide spinel, γ-Fe_2O_3.[237] As Li ions are inserted into the iron oxide, donated electrons from the Li ions lead to chemical reduction of the octahedral-site Fe ions, from Fe^{3+} ($5\mu_B$) to Fe^{2+} ($4\mu_B$), as shown in Figure 18b, as confirmed by an analysis of the Mössbauer data exhibiting an increase of the Fe^{2+} fraction from 3% to 33% after lithiation.[237] The valence change of the octahedral-site Fe ions and the associated

© 2017 WILEY-VCH Verlag GmbH & Co. KGaA, Weinheim

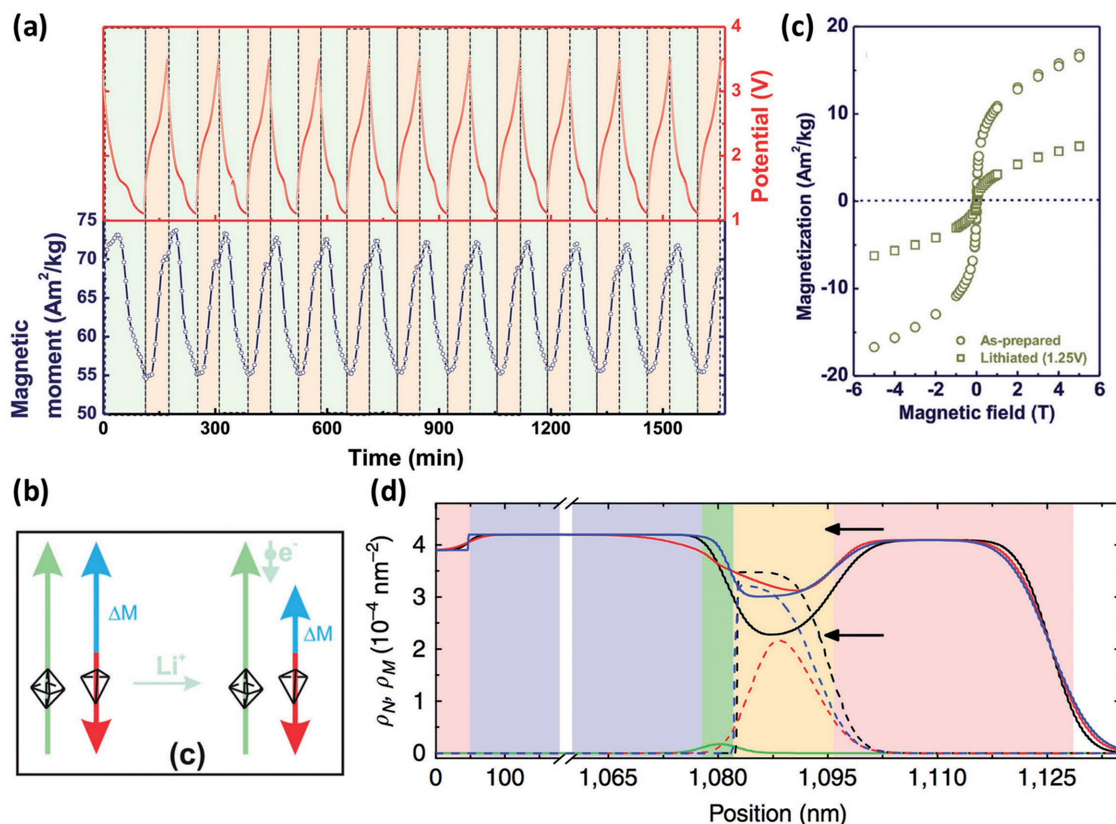

Figure 18. a) Reversible modulation of magnetic moment in response to electrical stimuli, due to electrochemically driven delithiation/lithiation in spinel iron oxide (γ-Fe_2O_3) nanoparticles. b) Schematic illustration of the magnetization modulation induced by lithium intercalation that reduces the octahedral-site Fe ions from +3 to +2 state, thus lowering its magnetic moment (as represented by the green arrow) and decreasing the total magnetization ΔM (blue arrows). Reproduced with permission.[237] Copyright 2014, John Wiley and Sons. c) Changes in magnetization of as-prepared and lithiated $ZnFe_2O_4$ samples, showing 70% loss of the saturation magnetic moment. Reproduced with permission.[239] Copyright 2016, John Wiley and Sons. d) Polarized neutron reflectometry depth profiles for as-grown (black), +40 V conditioned (red), and +/−40 V conditioned (blue) samples. The solid and dashed lines represent nuclear scattering length density (SLD), ρ_N, and magnetic SLD, ρ_M, respectively, and background colors represent Pd (red), AlO_x (blue), GdO_x (green), and Co (yellow) layers, respectively. The significant increase of the ρ_N curve inside the entire Co layer indicates that the applied electric field drives oxygen ions deep into the Co film, leading to decrease of the magnetization of the Co film. Reproduced with permission.[240] Copyright 2016, Nature Publishing Group.

magnetic state change, in turn, directly lead to the modulation of the overall bulk magnetism. In this approach, the amount of the ion intercalation should be carefully controlled to avoid irreversible structural destruction. The critical limit is one Li per formula unit,[237] and 1 Bohr magnetron (μ_B) can be reduced by one intercalated Li ion. Based on this understanding and intuition, ferrite systems that have precisely 1 μ_B net magnetic moment per formula unit such as $CuFeO_4$ were further investigated to obtain large and reversible magnetic property modulations toward on-and-off magnetism.[239] Upon the electrically controlled Li-ion exchange, a large change in magnetization was achieved in the $CuFeO_4$ system through the reduction of Cu^{2+} to Cu^{1+} ions, although fully on-and-off switching was still not obtained due to the increased net magnetic moment from the exchange of octahedral-site Cu^{2+} and tetrahedral-site Fe^{3+} ions in the as-prepared nanoparticles.[241] Additionally, shift of the Neél temperature was observed in the Li-ion exchange processes from which ≈70% magnetic response was obtained through magnetic phase transition in $ZnFe_2O_4$, as shown in Figure 18c.[239]

The magnetoionic motion based on oxygen migration can also extend far beyond the interface limit. In an Si/Pd/AlO_x/GdO_x/Co/Pd stack, polarized neutron reflectometry depth profile analysis verified significant field-driven oxygen migration into the Co layer throughout the entire thickness (15 nm), as shown in Figure 18d.[240] This O migration accompanied the reduction in the oscillation amplitude of spin asymmetry, indicating a decrease of magnetization saturation and/or structural changes. The oxidation of the Co layer was also verified from XAS measurements in which additional peaks were observed in electrically programmed samples whereas the peaks were not observed in the as-grown sample. Accompanying these material modulations, significant changes in coercivity (68%) and remanent (55%) magnetization were observed after electric and thermal treatment compared with the as-grown sample.

Magnetization Switching Coupled with Resistance Change: Nanoscale electrical control of magnetism through ion migration that is directly coupled with resistance change was also observed,[206] paving ways to tailor the magnetic properties of materials at the nanoscale. In a device based on a lithium ferrite

© 2017 WILEY-VCH Verlag GmbH & Co. KGaA, Weinheim

($LiFe_5O_8$) structure,[242] magnetization switching was observed accompanying resistive switching through the application of an external electric field, as shown in **Figure 19**a–c. Magnetic and electrical measurements verified that electric-field-induced atomic reconfiguration can induce nonvolatile and reversible modulation of the local magnetization at room temperature. Specifically, de-intercalation/intercalation of Li ions driven by the electric field alters the chemical state of the iron ions, leading to modulations of the magnetic moment.[243] At the same time, the Li-ion migration modulates the local concentration of electron hopping centers–Li vacancies, leading to the resistive switching effects. Scanning magnetic-force microscopy (MFM) analysis shows that the areas with significant magnetization changes exactly overlap with the high-conductivity areas in a C-AFM current map, confirming that the magnetization modulation originates from the same underlying atomic processes with resistive switching effects. The dynamic evolution of magnetic domains under voltage bias was also observed, showing an initial switching at a localized region followed by lateral expansion, again consistent with the characteristics of filament formation/growth processes observed in resistive switching devices. By utilizing the coupled magnetization and resistance changes, a multimode storage device in which two bits, represented respectively by the direction and the intensity of the film's magnetization, can be stored in one physical cell. The magnetization direction and the intensity were independently switched by an external magnetic field and an electric pulse, respectively. Subsequently, the stored data with four different states per cell can be properly read out through MFM measurements (Figure 19d).

5. Challenges, Looking into the Future, and Conclusions

In this article, we discussed atomic-level reconfiguration of materials through field-driven ionic processes, which we believe may lead to a new class of fundamental building blocks for future electronic, optical, and energy devices and multifunctional systems. Recent studies have clearly shown that physical reconfiguration of the material can occur through in situ, on-demand manipulation of matter (atoms) by electrical stimuli, leading to new functionalities beyond conventional mobile charge-based effects. Experimental studies such as in situ TEM analysis combined with spectroscopy characterizations have provided direct evidence showing that coupled ionic and electronic effects, such as chemical redox reactions and long-distance ion migration, can occur in solid-state semiconducting and dielectric films. Theoretical studies based on molecular dynamics and first-principles calculations have provided insight into the fundamental physical and chemical processes underlying the atomic processes involved in the material reconfigurations. A broad range of applications based on the reconfigurable materials and systems, ranging from nonvolatile data storage, neuromorphic computing, to optical switches and modulators, have been proposed and demonstrated, verifying the potential of such reconfigurable materials.

Looking into the future, a number of challenges at the materials/device level still need to be addressed to pave the way for practical, large-scale applications. For example, both cation- and anion-based devices suffer from variability issues that affect their applications in large-sized arrays. Cation-based devices are often found to show moderate endurance while anion-based devices typically exhibit low on/off ratio and high operating current. Advanced characterization techniques that can provide high spatial, temporal, and spectral resolution, thus enabling real-time, nondestructive analysis of the reconfiguration dynamics at the atomic scale will dramatically speed up the material and device developments. With the continued progress in materials, devices, and characterization techniques, we expect precise control of matter at the

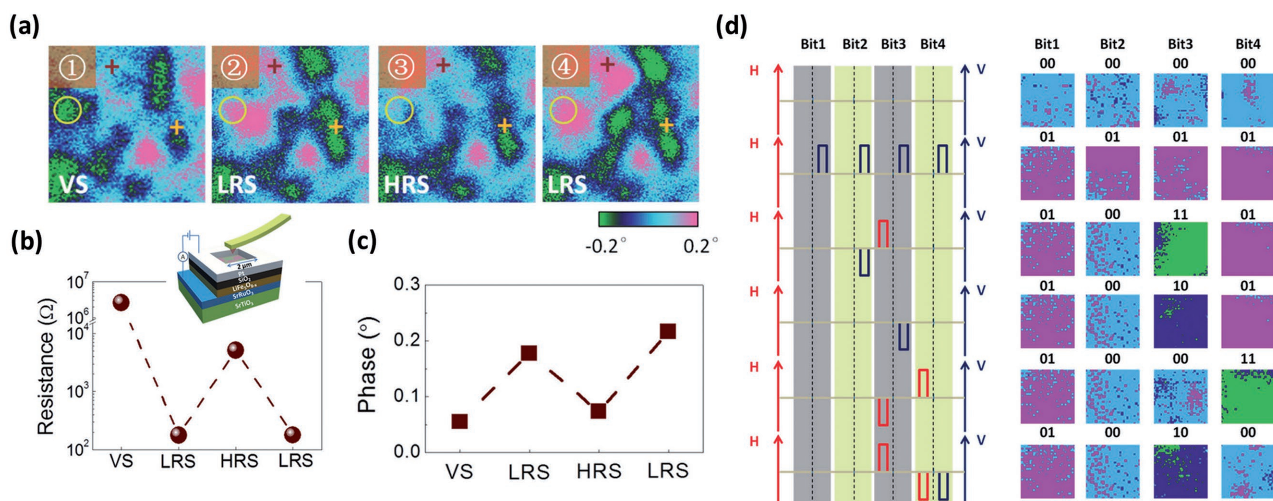

Figure 19. a) MFM images of an $LiFe_5O_8$-based device at different states during resistive switching cycles. b) The areas with significant changes of magnetization are highlighted. c) MFM phase data collected during electrical cycling in panel (b). The data are measured at the location marked by the brown cross in the MFM maps in panel (a), showing reversible modulation of magnetization that is correlated with the resistive switching behavior. d) Demonstration of multilevel data storage based on the coupled magnetization and resistance switching effects. Left: magnetic field (red) and electric pulse (blue) programming sequences for each domain, in which two bits are stored using the direction and the intensity of the domain's magnetization, respectively. Right: readout of the stored data from MFM measurements, showing four distinct states. Reproduced with permission.[206] Copyright 2016, John Wiley and Sons.

© 2017 WILEY-VCH Verlag GmbH & Co. KGaA, Weinheim

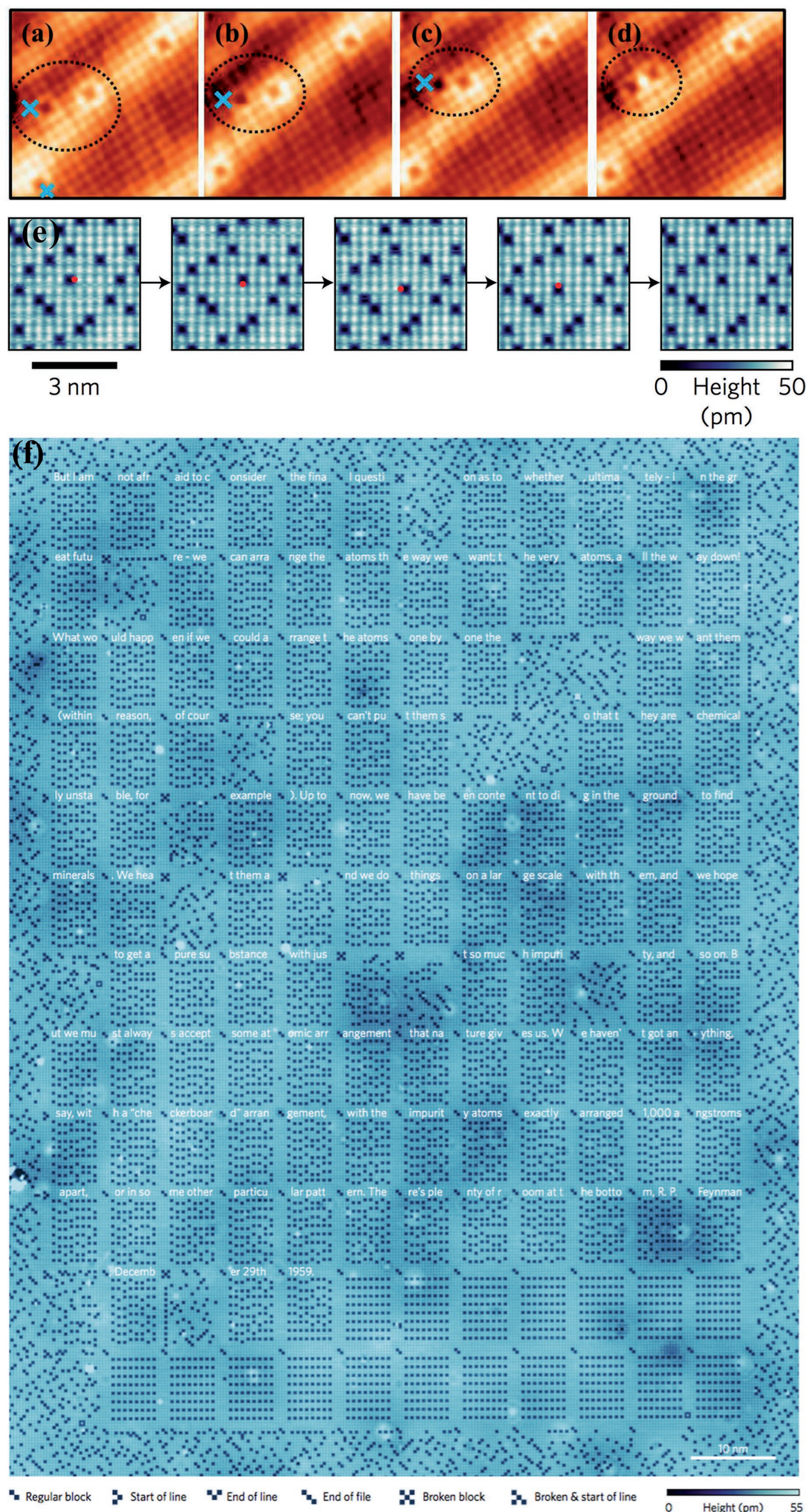

Figure 20. a–d) STM topography images of Cl vacancies in a NaCl/Au surface demonstrating atomic-level manipulation of the material configuration. Individual Cl vacancies can be laterally moved by the application of voltage with a STM tip. Reproduced with permission.[254] Copyright 2015, American Chemical Society. e) STM topography images of Cl vacancies (represented by dark blue squares) in a Cl/Cu surface showing that a Cl vacancy can be repositioned in all four directions by a STM tip, where the position of the STM tip is marked by a red dot. f) STM image of a kilobyte atomic memory through atom-by-atom manipulation of Cl vacancies, offering a high areal density of 502 terabits per square inch. Reproduced with permission.[255] Copyright 2016, Nature Publishing Group.

individual atom level can be eventually achieved, which will enable precise design and engineering of these reconfigurable materials. This level of control not only improves device scaling but also helps address issues such as device variability, endurance, and programming energy. Indeed, the principle of atomic-scale reconfiguration of materials has been demonstrated in studies of atomic switches in which quantum conductance effects were observed due to the formation of quantum point contacts (QPCs) having a single atom or a few atoms in the filament.[216,244,245] Highly reproducible and controllable QPC formations have been demonstrated experimentally in both ECM and VCM devices, and the detailed atomic configurations of QPCs consisting of only a few atoms were evaluated by first-principles calculations.[246–249] The formation of Ag clusters with an atomic contact bridging an scanning-tunneling-microscopy (STM) microscope tip and a substrate was also directly observed, supporting the feasibility of atomic control of matter movement through electrochemical processes.[250] Continued research will still be needed to improve the device reliability and to overcome the instability near the point-contact regime[76,251] and consequent retention loss.[252] Additionally, we note that recent studies on manipulation of individual atoms (or vacancies) with atomic precision using STM-microscope-tip based methods[253–255] have already led to the demonstration of a kilobyte rewritable atomic memory, in which data are encoded by the positions of individual chlorine vacancies, as shown in **Figure 20**. With further developments of the coupled ionic/

© 2017 WILEY-VCH Verlag GmbH & Co. KGaA, Weinheim

electronic systems that may allow in situ control of single atoms in solid-state materials/systems, an ultimate goal may be to replace the slow and low-temperature STM-tip based process with simple field-driven processes that can be easily implemented at room temperature, after the circuits have been completed. This kind of capability will no doubt lead to paradigm shifts in the design and fabrication of electronic, optical, and energy systems, and will require truly multidisciplinary efforts from physicists, chemists, materials scientists, engineers, and computer scientists to take full advantage of such reconfigurable materials.

Acknowledgements

The authors acknowledge financial support by the National Science Foundation (NSF) through grants ECCS-1708700 and CCF-1617315, and by the Defense Advanced Research Projects Agency (DARPA) through award HR0011-13-2-0015. J.L. was supported in part by the Kwanjeong Scholarship. The authors thank X. Zhu, Y. Jeong, S.H. Lee, and F. Cai for helpful discussions.

Conflict of Interest

The authors declare no conflict of interest.

Keywords

magnetoelectric effect, memristive systems, neuromorphic computing, plasmonic switching, resistive switching

Received: May 17, 2017
Revised: August 1, 2017
Published online: October 6, 2017

[1] I. R. Committee, *International Technology Roadmap for Semiconductors: 2013 Edition Executive Summary*, Semiconductor Industry Association, San Francisco, CA, USA **2013**.
[2] R. Waser, R. Dittmann, G. Staikov, K. Szot, *Adv. Mater.* **2009**, *21*, 2632.
[3] G. Meijer, *Science* **2008**, *319*, 1625.
[4] J. J. Yang, D. B. Strukov, D. R. Stewart, *Nat. Nanotechnol.* **2013**, *8*, 13.
[5] R. Waser, M. Aono, *Nat. Mater.* **2007**, *6*, 833.
[6] I. Valov, W. D. Lu, *Nanoscale* **2016**, *8*, 13828.
[7] P. Knauth, *Solid State Ionics* **2009**, *180*, 911.
[8] N. Kamaya, K. Homma, Y. Yamakawa, M. Hirayama, R. Kanno, M. Yonemura, T. Kamiyama, Y. Kato, S. Hama, K. Kawamoto, A. Mitsui, *Nat. Mater.* **2011**, *10*, 682.
[9] J. M. Tarascon, M. Armand, *Nature* **2001**, *414*, 359.
[10] M. Armand, J. M. Tarascon, *Nature* **2008**, *451*, 652.
[11] Y. Wang, W. D. Richards, S. P. Ong, L. J. Miara, J. C. Kim, Y. Mo, G. Ceder, *Nat. Mater.* **2015**, *14*, 1026.
[12] L. Chua, *IEEE Trans. Circuit Theory* **1971**, *18*, 507.
[13] L. O. Chua, S. M. Kang, *Proc. IEEE* **1976**, *64*, 209.
[14] D. B. Strukov, G. S. Snider, D. R. Stewart, R. S. Williams, *Nature* **2008**, *453*, 80.
[15] I. Valov, R. Waser, J. R. Jameson, M. N. Kozicki, *Nanotechnology* **2011**, *22*, 254003.
[16] S. H. Jo, W. Lu, in *9th Int. Conf. on Solid-State and Integrated-Circuit Technology* IEEE, Beijing, China **2008**.
[17] M. N. Kozicki, M. Park, M. Mitkova, *IEEE Trans. Nanotechnol.* **2005**, *4*, 331.
[18] C. Schindler, M. Weides, M. N. Kozicki, R. Waser, in *2008 IEEE Silicon Nanoelectronics Workshop*, IEEE, Honolulu, HI, USA **2008**.
[19] S. Gaba, F. Cai, J. Zhou, W. D. Lu, *IEEE Electron Device Lett.* **2014**, *35*, 1239.
[20] L. Goux, K. Sankaran, G. Kar, N. Jossart, K. Opsomer, R. Degraeve, G. Pourtois, G. M. Rignanese, C. Detavernier, S. Clima, Y. Y. Chen, A. Fantini, B. Govoreanu, D. J. Wouters, M. Jurczak, L. Altimime, J. A. Kittl, in *2012 Symp. on VLSI Technology (VLSIT)*, IEEE, Honolulu, HI, USA **2012**.
[21] S. H. Jo, K.-H. Kim, W. Lu, *Nano Lett.* **2009**, *9*, 870.
[22] S. H. Jo, W. Lu, *Nano Lett.* **2008**, *8*, 392.
[23] J. A. V. Butler, *Trans. Faraday Soc.* **1924**, *19*, 734.
[24] I. Valov, G. Staikov, *J. Solid State Electrochem.* **2012**, *17*, 365.
[25] S. H. Jo, K.-H. Kim, W. Lu, *Nano Lett.* **2009**, *9*, 496.
[26] U. Celano, L. Goux, A. Belmonte, K. Opsomer, A. Franquet, A. Schulze, C. Detavernier, O. Richard, H. Bender, M. Jurczak, W. Vandervorst, *Nano Lett.* **2014**, *14*, 2401.
[27] S. Tappertzhofen, S. Menzel, I. Valov, R. Waser, *Appl. Phys. Lett.* **2011**, *99*, 203103.
[28] S. Tappertzhofen, H. Mündelein, I. Valov, R. Waser, *Nanoscale* **2012**, *4*, 3040.
[29] T. Tsuruoka, I. Valov, S. Tappertzhofen, J. van den Hurk, T. Hasegawa, R. Waser, M. Aono, *Adv. Funct. Mater.* **2015**, *25*, 6374.
[30] S. Tappertzhofen, R. Waser, I. Valov, *ChemElectroChem* **2014**, *1*, 1287.
[31] Y. Yang, P. Gao, S. Gaba, T. Chang, X. Pan, W. Lu, *Nat. Commun.* **2012**, *3*, 732.
[32] Y. Yang, P. Gao, L. Li, X. Pan, S. Tappertzhofen, S. Choi, R. Waser, I. Valov, W. D. Lu, *Nat. Commun.* **2014**, *5*, 2382.
[33] J. J. Yang, M. X. Zhang, J. P. Strachan, F. Miao, M. D. Pickett, R. D. Kelley, G. Medeiros-Ribeiro, R. S. Williams, *Appl. Phys. Lett.* **2010**, *97*, 232102.
[34] M.-J. Lee, C. B. Lee, D. Lee, S. R. Lee, M. Chang, J. H. Hur, Y. B. Kim, C.-J. Kim, D. H. Seo, S. Seo, U.-I. Chung, I.-K. Yoo, K. Kim, *Nat. Mater.* **2011**, *10*, 625.
[35] Y. Yang, S. Choi, W. Lu, *Nano Lett.* **2013**, *13*, 2908.
[36] H. Y. Lee, P. S. Chen, T. Y. Wu, Y. S. Chen, C. C. Wang, P. J. Tzeng, C. H. Lin, F. Chen, C. H. Lien, M. J. Tsai, in *2008 IEEE Int. Electron Devices Meeting*, IEEE, San Francisco, CA, USA **2008**.
[37] Y. Y. Chen, L. Goux, S. Clima, B. Govoreanu, R. Degraeve, G. S. Kar, A. Fantini, G. Groeseneken, D. J. Wouters, M. Jurczak, *IEEE Trans. Electron Devices* **2013**, *60*, 1114.
[38] I. Goldfarb, F. Miao, J. J. Yang, W. Yi, J. P. Strachan, M. X. Zhang, M. D. Pickett, G. Medeiros-Ribeiro, R. S. Williams, *Appl. Phys. A: Solids Surf.* **2012**, *107*, 1.
[39] J. J. Yang, M. D. Pickett, X. Li, D. A. A. Ohlberg, D. R. Stewart, R. S. Williams, *Nat. Nanotechnol.* **2008**, *3*, 429.
[40] D.-H. Kwon, K. M. Kim, J. H. Jang, J. M. Jeon, M. H. Lee, G. H. Kim, X. S. Li, G.-S. Park, B. Lee, S. Han, M. Kim, C. S. Hwang, *Nat. Nanotechnol.* **2010**, *5*, 148.
[41] S. Yu, X. Guan, H.-S. P. Wong, *IEEE Trans. Electron Devices* **2012**, *59*, 1183.
[42] S. Ambrogio, S. Balatti, S. Choi, D. Ielmini, *Adv. Mater.* **2014**, *26*, 3885.
[43] S.-J. Choi, G.-S. Park, K.-H. Kim, S. Cho, W.-Y. Yang, X. S. Li, J.-H. Moon, K.-J. Lee, K. Kim, *Adv. Mater.* **2011**, *23*, 3272.
[44] J.-Y. Chen, C.-L. Hsin, C.-W. Huang, C.-H. Chiu, Y.-T. Huang, S.-J. Lin, W.-W. Wu, L.-J. Chen, *Nano Lett.* **2013**, *13*, 3671.

 © 2017 WILEY-VCH Verlag GmbH & Co. KGaA, Weinheim

[45] G.-S. Park, Y. B. Kim, S. Y. Park, X. S. Li, S. Heo, M.-J. Lee, M. Chang, J. H. Kwon, M. Kim, U.-I. Chung, R. Dittmann, R. Waser, K. Kim, *Nat. Commun.* **2013**, *4*, 1.
[46] W. A. Hubbard, A. Kerelsky, G. Jasmin, E. R. White, J. Lodico, M. Mecklenburg, B. C. Regan, *Nano Lett.* **2015**, *15*, 3983.
[47] J.-Y. Chen, C.-W. Huang, C.-H. Chiu, Y.-T. Huang, W.-W. Wu, *Adv. Mater.* **2015**, *27*, 5028.
[48] H. Lv, X. Xu, H. Liu, R. Liu, Q. Liu, W. Banerjee, H. Sun, S. Long, L. Li, M. Liu, *Sci. Rep.* **2015**, *5*, 7764.
[49] J. Lee, C. Du, K. Sun, E. Kioupakis, W. D. Lu, *ACS Nano* **2016**, *10*, 3571.
[50] J. P. Strachan, M. D. Pickett, J. J. Yang, S. Aloni, A. L. David Kilcoyne, G. Medeiros-Ribeiro, R. Stanley Williams, *Adv. Mater.* **2010**, *22*, 3573.
[51] S. Kumar, C. E. Graves, J. P. Strachan, A. L. D. Kilcoyne, T. Tyliszczak, Y. Nishi, R. S. Williams, *J. Appl. Phys.* **2015**, *118*, 034502.
[52] S. Kumar, C. E. Graves, J. P. Strachan, E. M. Grafals, A. L. D. Kilcoyne, T. Tyliszczak, J. N. Weker, Y. Nishi, R. S. Williams, *Adv. Mater.* **2016**, *28*, 2772.
[53] C. Baeumer, C. Schmitz, A. H. H. Ramadan, H. Du, K. Skaja, V. Feyer, P. Müller, B. Arndt, C.-L. Jia, J. Mayer, R. A. De Souza, C. M. Schneider, R. Waser, R. Dittmann, *Nat. Commun.* **2015**, *6*, 8610.
[54] C. Baeumer, C. Schmitz, A. Marchewka, D. N. Mueller, R. Valenta, J. Hackl, N. Raab, S. P. Rogers, M. I. Khan, S. Nemsak, M. Shim, S. Menzel, C. M. Schneider, R. Waser, R. Dittmann, *Nat. Commun.* **2016**, *7*, 12398.
[55] C. Baeumer, N. Raab, T. Menke, C. Schmitz, R. Rosezin, P. Müller, M. Andrä, V. Feyer, R. Bruchhaus, F. Gunkel, C. M. Schneider, R. Waser, R. Dittmann, *Nanoscale* **2016**, *8*, 13967.
[56] U. Celano, L. Goux, R. Degraeve, A. Fantini, O. Richard, H. Bender, M. Jurczak, W. Vandervorst, *Nano Lett.* **2015**, *15*, 7970.
[57] K. Krishnan, T. Tsuruoka, C. Mannequin, M. Aono, *Adv. Mater.* **2015**, *28*, 640.
[58] Q. Liu, J. Sun, H. Lv, S. Long, K. Yin, N. Wan, Y. Li, L. Sun, M. Liu, *Adv. Mater.* **2012**, *24*, 1844.
[59] X. Tian, S. Yang, M. Zeng, L. Wang, J. Wei, Z. Xu, W. Wang, X. Bai, *Adv. Mater.* **2014**, *26*, 3649.
[60] Y. Yang, W. Lu, *Nanoscale* **2013**, *5*, 10076.
[61] Y. Yang, W. D. Lu, *IEEE Trans. Nanotechnol.* **2016**, *15*, 465.
[62] C. Li, B. Gao, Y. Yao, X. Guan, X. Shen, Y. Wang, P. Huang, L. Liu, X. Liu, J. Li, C. Gu, J. Kang, R. Yu, *Adv. Mater.* **2017**, *29*, 1602976.
[63] J. P. Strachan, G. Medeiros-Ribeiro, J. J. Yang, M. X. Zhang, F. Miao, I. Goldfarb, M. Holt, V. Rose, R. S. Williams, *Appl. Phys. Lett.* **2011**, *98*, 242114.
[64] F. Miao, J. P. Strachan, J. J. Yang, M.-X. Zhang, I. Goldfarb, A. C. Torrezan, P. Eschbach, R. D. Kelley, G. Medeiros-Ribeiro, R. S. Williams, *Adv. Mater.* **2011**, *23*, 5633.
[65] D. B. Strukov, F. Alibart, R. Stanley Williams, *Appl. Phys. A: Solids Surf.* **2012**, *107*, 509.
[66] A. Wedig, M. Luebben, D.-Y. Cho, M. Moors, K. Skaja, V. Rana, T. Hasegawa, K. K. Adepalli, B. Yildiz, R. Waser, I. Valov, *Nat. Nanotechnol.* **2015**, *11*, 67.
[67] B. Fultz, J. M. Howe, *Transmission Electron Microscopy and Diffractometry of Materials*, Springer Science & Business Media, Berlin, Germany **2012**.
[68] D. Carta, G. Mountjoy, A. Regoutz, A. Khiat, A. Serb, T. Prodromakis, *J. Phys. Chem. C* **2015**, *119*, 4362.
[69] D.-Y. Cho, M. Luebben, S. Wiefels, K.-S. Lee, I. Valov, *ACS Appl. Mater. Interfaces* **2017**, *9*, 19287.
[70] W. Kim, S. Menzel, D. J. Wouters, Y. Guo, J. Robertson, B. Roesgen, R. Waser, V. Rana, *Nanoscale* **2016**, *8*, 17774.
[71] D.-Y. Cho, I. Valov, J. van den Hurk, S. Tappertzhofen, R. Waser, *Adv. Mater.* **2012**, *24*, 4552.
[72] K. Szot, W. Speier, G. Bihlmayer, R. Waser, *Nat. Mater.* **2006**, *5*, 312.
[73] C. Lenser, M. Patt, S. Menzel, A. Köhl, C. Wiemann, C. M. Schneider, R. Waser, R. Dittmann, *Adv. Funct. Mater.* **2014**, *24*, 4466.
[74] M. J. Kim, I. G. Baek, Y. H. Ha, S. J. Baik, in *2010 IEEE Int. Electron Devices Meeting (IEDM)*, IEEE, San Francisco, CA, USA **2010**.
[75] B. Govoreanu, G. S. Kar, Y. Y. Chen, V. Paraschiv, S. Kubicek, A. Fantini, I. P. Radu, L. Goux, S. Clima, R. Degraeve, N. Jossart, O. Richard, T. Vandeweyer, K. Seo, P. Hendrickx, G. Pourtois, H. Bender, L. Altimime, D. J. Wouters, J. A. Kittl, M. Jurczak, in *2011 Int. Electron Devices Meeting*, IEEE, Washington, DC, USA **2011**.
[76] N. Onofrio, D. Guzman, A. Strachan, *Nat. Mater.* **2015**, *14*, 440.
[77] N. Onofrio, D. Guzman, A. Strachan, *Nanoscale* **2016**, *8*, 14037.
[78] A. K. Rappe, W. A. Goddard, *J. Phys. Chem.* **1991**, *95*, 3358.
[79] A. C. T. van Duin, A. Strachan, S. Stewman, Q. Zhang, X. Xu, W. A. Goddard, *J. Phys. Chem. A* **2003**, *107*, 3803.
[80] R. J. Bondi, M. P. Desjarlais, A. P. Thompson, G. L. Brennecka, M. J. Marinella, *J. Appl. Phys.* **2013**, *114*, 203701.
[81] B. Xiao, S. Watanabe, *Nanoscale* **2014**, *6*, 10169.
[82] K. Kamiya, M. Y. Yang, S.-G. Park, B. Magyari-Köpe, Y. Nishi, M. Niwa, K. Shiraishi, *Appl. Phys. Lett.* **2012**, *100*, 073502.
[83] K. Sankaran, L. Goux, S. Clima, M. Mees, J. A. Kittl, M. Jurczak, L. Altimime, G. M. Rignanese, G. Pourtois, *ECS Trans.* **2012**, *45*, 317.
[84] S. Clima, Y. Y. Chen, R. Degraeve, M. Mees, K. Sankaran, B. Govoreanu, M. Jurczak, S. De Gendt, G. Pourtois, *Appl. Phys. Lett.* **2012**, *100*, 133102.
[85] H. Jiang, D. A. Stewart, *J. Appl. Phys.* **2016**, *119*, 134502.
[86] J. Lee, W. D. Lu, E. Kioupakis, *Nanoscale* **2017**, *9*, 1120.
[87] S. Clima, Y. Y. Chen, C. Y. Chen, L. Goux, B. Govoreanu, R. Degraeve, A. Fantini, M. Jurczak, G. Pourtois, *J. Appl. Phys.* **2016**, *119*, 225107.
[88] S. Larentis, F. Nardi, S. Balatti, D. C. Gilmer, D. Ielmini, *IEEE Trans. Electron Devices* **2012**, *59*, 2468.
[89] S. Kim, S. Choi, W. Lu, *ACS Nano* **2014**, *8*, 2369.
[90] E. Linn, R. Rosezin, C. Kügeler, R. Waser, *Nat. Mater.* **2010**, *9*, 403.
[91] F. Nardi, S. Balatti, S. Larentis, D. C. Gilmer, D. Ielmini, *IEEE Trans. Electron Devices* **2012**, *60*, 70.
[92] Y. Yang, P. Sheridan, W. Lu, *Appl. Phys. Lett.* **2012**, *100*, 203112.
[93] S. Kim, S. Choi, J. Lee, W. D. Lu, *ACS Nano* **2014**, *8*, 10262.
[94] Z. Wang, M. Yin, T. Zhang, Y. Cai, Y. Wang, Y. Yang, R. Huang, *Nanoscale* **2016**, *8*, 14015.
[95] A. Prakash, D. Deleruyelle, J. Song, M. Bocquet, H. Hwang, *Appl. Phys. Lett.* **2015**, *106*, 233104.
[96] Y. Jeong, S. Kim, W. D. Lu, *Appl. Phys. Lett.* **2015**, *107*, 173105.
[97] S. Kim, C. Du, P. Sheridan, W. Ma, S. Choi, W. D. Lu, *Nano Lett.* **2015**, *15*, 2203.
[98] C. S. Hwang, *Adv. Electron. Mater.* **2015**, *1*, 1400056.
[99] A. C. Torrezan, J. P. Strachan, G. Medeiros-Ribeiro, R. S. Williams, *Nanotechnology* **2011**, *22*, 485203.
[100] B. J. Choi, A. C. Torrezan, J. P. Strachan, P. G. Kotula, A. J. Lohn, M. J. Marinella, Z. Li, R. S. Williams, J. J. Yang, *Adv. Funct. Mater.* **2016**, *26*, 5290.
[101] S. Choi, J. Lee, S. Kim, W. D. Lu, *Appl. Phys. Lett.* **2014**, *105*, 113510.
[102] S. Clima, Y. Y. Chen, A. Fantini, L. Goux, R. Degraeve, B. Govoreanu, G. Pourtois, M. Jurczak, *IEEE Electron Device Lett.* **2015**, *36*, 769.
[103] A. Fantini, L. Goux, R. Degraeve, D. J. Wouters, N. Raghavan, G. Kar, A. Belmonte, Y. Y. Chen, B. Govoreanu, M. Jurczak, in *2013 5th IEEE Int. Memory Workshop*, IEEE, Monterey, CA, USA **2013**.
[104] S. Gaba, P. Sheridan, J. Zhou, S. Choi, W. Lu, *Nanoscale* **2013**, *5*, 5872.

© 2017 WILEY-VCH Verlag GmbH & Co. KGaA, Weinheim

[105] K.-H. Jo, C.-M. Jung, K.-S. Min, S.-M. Kang, *IEEE Trans. Nanotechnol.* **2010**, *9*, 675.
[106] S. Yu, B. Gao, H. Dai, B. Sun, L. Liu, X. Liu, R. Han, J. Kang, B. Yu, *Electrochem. Solid-State Lett.* **2010**, *13*, H36.
[107] H. Zhang, L. Liu, B. Gao, Y. Qiu, X. Liu, J. Lu, R. Han, J. Kang, B. Yu, *Appl. Phys. Lett.* **2011**, *98*, 042105.
[108] Z. Wang, W. G. Zhu, A. Y. Du, L. Wu, Z. Fang, X. A. Tran, W. J. Liu, K. L. Zhang, H. Y. Yu, *IEEE Trans. Electron Devices* **2012**, *59*, 1203.
[109] Q. Liu, S. Long, H. Lv, W. Wang, J. Niu, Z. Huo, J. Chen, M. Liu, *ACS Nano* **2010**, *4*, 6162.
[110] J. H. Yoon, J. H. Han, J. S. Jung, W. Jeon, G. H. Kim, S. J. Song, J. Y. Seok, K. J. Yoon, M. H. Lee, C. S. Hwang, *Adv. Mater.* **2013**, *25*, 1987.
[111] P. Bousoulas, S. Stathopoulos, D. Tsialoukis, D. Tsoukalas, *IEEE Electron Device Lett.* **2016**, *37*, 874.
[112] B. K. You, J. M. Kim, D. J. Joe, K. Yang, Y. Shin, Y. S. Jung, K. J. Lee, *ACS Nano* **2016**, *10*, 9478.
[113] X. Zhao, S. Liu, J. Niu, L. Liao, Q. Liu, X. Xiao, H. Lv, S. Long, W. Banerjee, W. Li, S. Si, M. Liu, *Small* **2017**, *13*, 1603948.
[114] I. R. Committee, *International Technology Roadmap for Semiconductors: 2015 Edition Section 6: Beyond CMOS*, Semiconductor Industry Association, Stanford, CA, USA **2015**.
[115] L. Goux, A. Fantini, G. Kar, Y. Y. Chen, N. Jossart, R. Degraeve, S. Clima, B. Govoreanu, G. Lorenzo, G. Pourtois, D. J. Wouters, J. A. Kittl, L. Altimime, M. Jurczak, in *2012 Symp. on VLSI Technology (VLSIT)*, IEEE, Honolulu, HI, USA **2012**.
[116] C. Y. Chen, L. Goux, A. Fantini, R. Degraeve, A. Redolfi, G. Groeseneken, M. Jurczak, in *2015 45th European Solid State Device Research Conf. (ESSDERC)*, IEEE, Graz, Austria **2015**.
[117] Z. Zhang, Y. Wu, H.-S. P. Wong, S. S. Wong, *IEEE Electron Device Lett.* **2013**, *34*, 1005.
[118] Y. Hou, U. Celano, L. Goux, L. Liu, A. Fantini, R. Degraeve, A. Youssef, Z. Xu, Y. Cheng, J. Kang, M. Jurczak, W. Vandervorst, *Appl. Phys. Lett.* **2016**, *108*, 123106.
[119] J. Zhou, F. Cai, Q. Wang, B. Chen, S. Gaba, W. D. Lu, *IEEE Electron Device Lett.* **2016**, *37*, 404.
[120] M. Barci, G. Molas, A. Toffoli, M. Bernard, A. Roule, C. Cagli, J. Cluzel, E. Vianello, B. De Salvo, L. Perniola, in *2015 IEEE Int. Memory Workshop (IMW)*, IEEE, Monterey, CA, USA **2015**.
[121] A. Belmonte, W. Kim, B. T. Chan, N. Heylen, A. Fantini, M. Houssa, M. Jurczak, L. Goux, *IEEE Trans. Electron Devices* **2013**, *60*, 3690.
[122] S. Liu, N. Lu, X. Zhao, H. Xu, W. Banerjee, H. Lv, S. Long, Q. Li, Q. Liu, M. Liu, *Adv. Mater.* **2016**, *28*, 10623.
[123] K.-H. Kim, S. Gaba, D. Wheeler, J. M. Cruz-Albrecht, T. Hussain, N. Srinivasa, W. Lu, *Nano Lett.* **2012**, *12*, 389.
[124] J. Zhou, K.-H. Kim, W. Lu, *IEEE Trans. Electron Devices* **2014**, *61*, 1369.
[125] S. Kim, J. Zhou, W. D. Lu, *IEEE Trans. Electron Devices* **2014**, *61*, 2820.
[126] A. Kawahara, R. Azuma, Y. Ikeda, K. Kawai, Y. Katoh, Y. Hayakawa, K. Tsuji, S. Yoneda, A. Himeno, K. Shimakawa, T. Takagi, T. Mikawa, K. Aono, *IEEE J. Solid-State Circuits* **2013**, *48*, 178.
[127] G. H. Kim, J. H. Lee, Y. Ahn, W. Jeon, S. J. Song, J. Y. Seok, J. H. Yoon, K. J. Yoon, T. J. Park, C. S. Hwang, *Adv. Funct. Mater.* **2012**, *23*, 1440.
[128] W. Lee, J. Park, S. Kim, J. Woo, J. Shin, G. Choi, S. Park, D. Lee, E. Cha, B. H. Lee, H. Hwang, *ACS Nano* **2012**, *6*, 8166.
[129] B. J. Choi, J. Zhang, K. Norris, G. Gibson, K. M. Kim, W. Jackson, M.-X. M. Zhang, Z. Li, J. J. Yang, R. S. Williams, *Adv. Mater.* **2015**, *28*, 356.
[130] G. W. Burr, K. Virwani, R. S. Shenoy, G. Fraczak, C. T. Rettner, A. Padilla, R. S. King, K. Nguyen, A. N. Bowers, M. Jurich, M. BrightSky, E. A. Joseph, A. J. Kellock, N. Arellano, B. N. Kurdi, K. Gopalakrishnan, in *2013 Symp. VLSI Technology (VLSIT)*, IEEE, Kyoto, Japan **2013**.
[131] S. Kim, Y. B. Kim, K. M. Kim, S.-J. Kim, S. R. Lee, M. Chang, E. Cho, M.-J. Lee, D. Lee, C.-J. Kim, U.-I. Chung, I.-K. Yoo, in *2013 Symp. VLSI Technology (VLSIT)*, IEEE, Kyoto, Japan **2013**.
[132] M. J. Lee, Y. Park, D. S. Suh, E. H. Lee, S. Seo, D. C. Kim, R. Jung, B. S. Kang, S. E. Ahn, C. B. Lee, D. H. Seo, Y. K. Cha, I. K. Yoo, J. S. Kim, B. H. Park, *Adv. Mater.* **2007**, *19*, 3919.
[133] S. Kumar, M. D. Pickett, J. P. Strachan, G. Gibson, Y. Nishi, R. S. Williams, *Adv. Mater.* **2013**, *25*, 6128.
[134] E. Cha, J. Woo, D. Lee, S. Lee, J. Song, Y. Koo, J. Lee, C. G. Park, M. Y. Yang, K. Kamiya, K. Shiraishi, B. Magyari-Köpe, Y. Nishi, H. Hwang, in *2013 IEEE Int. Electron Devices Meeting*, IEEE, Washington, DC, USA **2013**.
[135] R. Midya, Z. Wang, J. Zhang, S. E. Savel'ev, C. Li, M. Rao, M. H. Jang, S. Joshi, H. Jiang, P. Lin, K. Norris, N. Ge, Q. Wu, M. Barnell, Z. Li, H. L. Xin, R. S. Williams, Q. Xia, J. J. Yang, *Adv. Mater.* **2017**, *29*, 1604457.
[136] Z. Wang, S. Joshi, S. E. Savel'ev, H. Jiang, R. Midya, P. Lin, M. Hu, N. Ge, J. P. Strachan, Z. Li, Q. Wu, M. Barnell, G.-L. Li, H. L. Xin, R. S. Williams, Q. Xia, J. J. Yang, *Nat. Mater.* **2016**, *16*, 101.
[137] C. T. Chou, C. W. Hsu, C. C. Chang, T. H. Hou, in *Extended Abstracts of the 2014 Int. Conf. Solid State Devices and Materials*, The Japan Society of Applied Physics, Ibaraki, Japan **2014**.
[138] J. H. Yoon, K. M. Kim, S. J. Song, J. Y. Seok, K. J. Yoon, D. E. Kwon, T. H. Park, Y. J. Kwon, X. Shao, C. S. Hwang, *Adv. Mater.* **2015**, *27*, 3811.
[139] A. H. Edwards, H. J. Barnaby, K. A. Campbell, M. N. Kozicki, W. Liu, M. J. Marinella, *Proc. IEEE* **2015**, *103*, 1004.
[140] C. Kügeler, M. Meier, R. Rosezin, S. Gilles, R. Waser, *Solid State Electron.* **2009**, *53*, 1287.
[141] S. Song, B. Cho, T.-W. Kim, Y. Ji, M. Jo, G. Wang, M. Choe, Y. H. Kahng, H. Hwang, T. Lee, *Adv. Mater.* **2010**, *22*, 5048.
[142] M.-C. Hsieh, Y.-C. Liao, Y.-W. Chin, C.-H. Lien, T.-S. Chang, Y.-D. Chih, S. Natarajan, M.-J. Tsai, Y.-C. King, C. J. Lin, in *2013 IEEE Int. Electron Devices Meeting*, IEEE, Washington, DC, USA **2013**.
[143] J. Y. Seok, S. J. Song, J. H. Yoon, K. J. Yoon, T. H. Park, D. E. Kwon, H. Lim, G. H. Kim, D. S. Jeong, C. S. Hwang, *Adv. Funct. Mater.* **2014**, *24*, 5316.
[144] H. S. Yoon, I.-G. Baek, J. Zhao, H. Sim, M. Y. Park, H. Lee, G.-H. Oh, J. C. Shin, I.-S. Yeo, U.-I. Chung, in *2012 Symp. VLSI Technology (VLSIT)*, IEEE, Honolulu, HI, USA **2009**.
[145] I. G. Baek, C. J. Park, H. Ju, D. J. Seong, H. S. Ahn, J. H. Kim, M. K. Yang, S. H. Song, E. M. Kim, S. O. Park, C. H. Park, C. W. Song, G. T. Jeong, S. Choi, H. K. Kang, C. Chung, in *2011 Int. Electron Devices Meeting*, IEEE, Washington, DC, USA **2011**.
[146] H.-Y. Chen, S. Yu, B. Gao, P. Huang, J. Kang, H.-S. P. Wong, in *2012 Int. Electron Devices Meeting*, IEEE, San Francisco, CA, USA **2012**.
[147] C.-W. Hsu, C.-C. Wan, I.-T. Wang, M.-C. Chen, C.-L. Lo, Y.-J. Lee, W.-Y. Jang, C.-H. Lin, T.-H. Hou, in *2013 IEEE Int. Electron Devices Meeting*, IEEE, Washington, DC, USA **2013**.
[148] S. Gaba, P. Sheridan, C. Du, W. Lu, *IEEE Trans. Electron Devices* **2014**, *61*, 2581.
[149] Y. Bai, H. Wu, R. Wu, Y. Zhang, N. Deng, Z. Yu, H. Qian, *Sci. Rep.* **2014**, *4*, 3213.
[150] S. Lee, J. Sohn, Z. Jiang, H.-Y. Chen, H.-S. P. Wong, *Nat. Commun.* **2015**, *6*, 8407.
[151] S. H. Jo, T. Chang, I. Ebong, B. B. Bhadviya, P. Mazumder, W. Lu, *Nano Lett.* **2010**, *10*, 1297.
[152] T. Ohno, T. Hasegawa, T. Tsuruoka, K. Terabe, J. K. Gimzewski, M. Aono, *Nat. Mater.* **2011**, *10*, 591.
[153] M. D. Pickett, G. Medeiros-Ribeiro, R. S. Williams, *Nat. Mater.* **2012**, *12*, 114.
[154] Y. V. Pershin, M. Di Ventra, *Proc. IEEE* **2012**, *100*, 2071.

 © 2017 WILEY-VCH Verlag GmbH & Co. KGaA, Weinheim

[155] D. S. Modha, R. Ananthanarayanan, S. K. Esser, A. Ndirango, A. J. Sherbondy, R. Singh, *Commun. ACM* **2011**, *54*, 62.
[156] G. Indiveri, B. Linares-Barranco, T. J. Hamilton, A. van Schaik, R. Etienne-Cummings, T. Delbruck, S.-C. Liu, P. Dudek, P. Häfliger, S. Renaud, J. Schemmel, G. Cauwenberghs, J. Arthur, K. Hynna, F. Folowosele, S. Saighi, T. Serrano-Gotarredona, J. Wijekoon, Y. Wang, K. Boahen, *Front. Neurosci.* **2011**, *5*, 73.
[157] C.-S. Poon, K. Zhou, *Front. Neurosci.* **2011**, *5*, 108.
[158] C. Mead, *Proc. IEEE* **1990**, *78*, 1629.
[159] G. Indiveri, S.-C. Liu, *Proc. IEEE* **2015**, *103*, 1379.
[160] T. Chang, S. H. Jo, K.-H. Kim, P. Sheridan, S. Gaba, W. Lu, *Appl. Phys. A: Solids Surf.* **2011**, *102*, 857.
[161] D. B. Strukov, R. S. Williams, *Appl. Phys. A: Solids Surf.* **2008**, *94*, 515.
[162] L. Chua, *Appl. Phys. A*, **2011**, *102*, 765.
[163] P. Sheridan, W. Lu, *Memristors and Memristive Devices for Neuromorphic Computing*, Springer International Publishing, Cham, Switzerland **2014**.
[164] W. M. Cowan, T. C. Südhof, C. F. Stevens, *Synapses*, JHU Press, Baltimore, MD, USA **2001**.
[165] R. S. Zucker, W. G. Regehr, *Annu. Rev. Physiol.* **2002**, *64*, 355.
[166] T. V. P. Bliss, G. L. Collingridge, *Nature* **1993**, *361*, 31.
[167] W. C. Abraham, *Philos. Trans. R. Soc., B* **2003**, *358*, 735.
[168] T. V. P. Bliss, T. Lømo, *J. Physiol.* **1973**, *232*, 331.
[169] P. J. Sjöström, G. G. Turrigiano, S. B. Nelson, *Neuron* **2001**, *32*, 1149.
[170] T. Chang, Y. Yang, W. Lu, *IEEE Circuits Syst. Mag.* **2013**, *13*, 56.
[171] D. Kuzum, S. Yu, H.-S. P. Wong, *Nanotechnology* **2013**, *24*, 382001.
[172] D. S. Jeong, K. M. Kim, S. Kim, B. J. Choi, C. S. Hwang, *Adv. Electron. Mater.* **2016**, *2*, 1600090.
[173] P. M. Sheridan, C. Du, W. D. Lu, *IEEE Trans. Neural Networks Learning Syst.* **2016**, *27*, 2327.
[174] M. Prezioso, F. Merrikh-Bayat, B. D. Hoskins, G. C. Adam, K. K. Likharev, D. B. Strukov, *Nature* **2015**, *521*, 61.
[175] G. S. Snider, in *2008 IEEE Int. Symp. Nanoscale Architectures*, IEEE, Anaheim, CA, USA **2008**.
[176] C. Zamarreño-Ramos, L. A. Camuñas-Mesa, J. A. Pérez-Carrasco, T. Masquelier, T. Serrano-Gotarredona, B. Linares-Barranco, *Front. Neurosci.* **2011**, *5*, 26.
[177] S. Agarwal, T.-T. Quach, O. Parekh, A. H. Hsia, E. P. DeBenedictis, C. D. James, M. J. Marinella, J. B. Aimone, *Front. Neurosci.* **2016**, *9*, 3498.
[178] M. J. Marinella, S. Agarwal, D. Hughart, S. Plimpton, O. Parekh, T.-T. Quach, E. Debenedictis, R. S. Goeke, A. H. Hsia, J. B. Aimone, C. D. James, in *IEEE Rebooting Computing Summit 4 (RCS 4)*, IEEE, Washington, DC, USA **2015**.
[179] S. N. Yang, Y. G. Tang, R. S. Zucker, *J. Neurophysiol.* **1999**, *81*, 781.
[180] H. Z. Shouval, M. F. Bear, L. N. Cooper, *Proc. Natl. Acad. Sci. USA* **2002**, *99*, 10831.
[181] M. Graupner, N. Brunel, *Proc. Natl. Acad. Sci. USA* **2012**, *109*, 3991.
[182] C. Du, W. Ma, T. Chang, P. Sheridan, W. D. Lu, *Adv. Funct. Mater.* **2015**, *25*, 4290.
[183] I. Valov, E. Linn, S. Tappertzhofen, S. Schmelzer, J. van den Hurk, F. Lentz, R. Waser, *Nat. Commun.* **2013**, *4*, 1771.
[184] D. A. Drachman, *Neurology* **2005**, *64*, 2004.
[185] L. Gao, F. Alibart, D. B. Strukov, in *2012 IEEE/IFIP 20th Int. Conf. VLSI and System-on-Chip (VLSI-SoC)*, IEEE, Santa Cruz, CA, USA **2012**.
[186] E. J. Merced-Grafals, N. Davila, N. Ge, R. S. Williams, J. P. Strachan, *Nanotechnology* **2016**, *27*, 365202.
[187] W. Schiffmann, M. Joost, R. Werner, *University of Koblenz: Institute of Physics*, Koblenz, Germany **1994**.
[188] M. Sonka, V. Hlavac, R. Boyle, *Image Processing, Analysis*, Springer, Boston, MA, USA **1993**.
[189] H. Abdi, L. J. Williams, *Wiley Interdis. Rev.: Comput. Stat.* **2010**, *2*, 433.
[190] S. Choi, J. H. Shin, J. Lee, P. Sheridan, W. D. Lu, *Nano Lett.* **2017**, *17*, 3113.
[191] T. D. Sanger, *Neural Networks* **1989**, *2*, 459.
[192] B. A. Olshausen, D. J. Field, *Nature* **1996**, *381*, 607.
[193] W. E. Vinje, *Science* **2000**, *287*, 1273.
[194] T. Hromádka, M. R. DeWeese, A. M. Zador, *PLoS Biol.* **2008**, *6*, e16.
[195] P. M. Sheridan, F. Cai, C. Du, W. Ma, Z. Zhang, W. D. Lu, *Nat. Nano* **2017**, *18*, 507.
[196] C. J. Rozell, D. H. Johnson, R. G. Baraniuk, B. A. Olshausen, *Neural Comput.* **2008**, *20*, 2526.
[197] S. Yu, P.-Y. Chen, Y. Cao, L. Xia, Y. Wang, H. Wu, in *2015 IEEE Int. Electron Devices Meeting (IEDM)*, IEEE, Washington, DC, USA **2015**.
[198] S. Agarwal, S. J. Plimpton, D. R. Hughart, A. H. Hsia, I. Richter, J. A. Cox, C. D. James, M. J. Marinella, in *2016 Int. Joint Conf. on Neural Networks (IJCNN)*, IEEE, Vancouver, BC, Canada **2016**.
[199] G. S. Snider, R. S. Williams, *Nanotechnology* **2007**, *18*, 035204.
[200] Q. Xia, W. Robinett, M. W. Cumbie, N. Banerjee, T. J. Cardinali, J. J. Yang, W. Wu, X. Li, W. M. Tong, D. B. Strukov, G. S. Snider, G. Medeiros-Ribeiro, R. S. Williams, *Nano Lett.* **2009**, *9*, 3640.
[201] J. Borghetti, G. S. Snider, P. J. Kuekes, J. J. Yang, D. R. Stewart, R. S. Williams, *Nature* **2010**, *464*, 873.
[202] A. Emboras, I. Goykhman, B. Desiatov, N. Mazurski, L. Stern, J. Shappir, U. Levy, *Nano Lett.* **2013**, *13*, 6151.
[203] C. Hoessbacher, Y. Fedoryshyn, A. Emboras, A. Melikyan, M. Kohl, D. Hillerkuss, C. Hafner, J. Leuthold, *Optica* **2014**, *1*, 198.
[204] A. Emboras, J. Niegemann, P. Ma, C. Haffner, A. Pedersen, M. Luisier, C. Hafner, T. Schimmel, J. Leuthold, *Nano Lett.* **2016**, *16*, 709.
[205] U. Bauer, L. Yao, A. J. Tan, P. Agrawal, S. Emori, H. L. Tuller, S. van Dijken, G. S. D. Beach, *Nat. Mater.* **2014**, *14*, 174.
[206] X. Zhu, J. Zhou, L. Chen, S. Guo, G. Liu, R.-W. Li, W. D. Lu, *Adv. Mater.* **2016**, *28*, 7658.
[207] A. Emboras, C. Hoessbacher, C. Haffner, W. Heni, U. Koch, P. Ma, Y. Fedoryshyn, J. Niegemann, C. Hafner, J. Leuthold, *IEEE J. Sel. Top. Quantum Electron.* **2015**, *21*, 276.
[208] K. C. Y. Huang, M.-K. Seo, T. Sarmiento, Y. Huo, J. S. Harris, M. L. Brongersma, *Nat. Photonics* **2014**, *8*, 244.
[209] A. Melikyan, L. Alloatti, A. Muslija, D. Hillerkuss, P. C. Schindler, J. Li, R. Palmer, D. Korn, S. Muehlbrandt, D. Van Thourhout, B. Chen, R. Dinu, M. Sommer, C. Koos, M. Kohl, W. Freude, J. Leuthold, *Nat. Photonics* **2014**, *8*, 229.
[210] T. Nikolajsen, K. Leosson, S. I. Bozhevolnyi, *Appl. Phys. Lett.* **2004**, *85*, 5833.
[211] J. A. Dionne, K. Diest, L. A. Sweatlock, H. A. Atwater, *Nano Lett.* **2009**, *9*, 897.
[212] C. A. Barrios, M. Lipson, *J. Lightwave Technol.* **2006**, *24*, 2898.
[213] S. Papaioannou, D. Kalavrouziotis, K. Vyrsokinos, J.-C. Weeber, K. Hassan, L. Markey, A. Dereux, A. Kumar, S. I. Bozhevolnyi, M. Baus, T. Tekin, D. Apostolopoulos, H. Avramopoulos, N. Pleros, *Sci. Rep.* **2012**, *2*, 38.
[214] K. Thyagarajan, R. Sokhoyan, L. Zornberg, H. A. Atwater, *Adv. Mater.* **2017**, *6*, 1701044.
[215] F. Q. Xie, L. Nittler, C. Obermair, T. Schimmel, *Phys. Rev. Lett.* **2004**, *93*, 128303.
[216] K. Terabe, T. Hasegawa, T. Nakayama, M. Aono, *Nature* **2005**, *433*, 47.
[217] E. Timurdogan, C. M. Sorace-Agaskar, J. Sun, E. S. Hosseini, A. Biberman, M. R. Watts, *Nat. Commun.* **2014**, *5*, 4008.
[218] B. S. Dennis, M. I. Haftel, D. A. Czaplewski, D. Lopez, G. Blumberg, V. A. Aksyuk, *Nat. Photonics* **2015**, *7606*, 76060N.

© 2017 WILEY-VCH Verlag GmbH & Co. KGaA, Weinheim

[219] D. O'shea, C. Junge, J. Volz, A. Rauschenbeutel, *Phys. Rev. Lett.* **2013**, *111*, 193601.
[220] I. Shomroni, S. Rosenblum, Y. Lovsky, O. Bechler, G. Guendelman, B. Dayan, *Science* **2014**, *345*, 903.
[221] D. T. Schoen, A. L. Holsteen, M. L. Brongersma, *Nat. Commun.* **2016**, *7*, 1.
[222] E. B. Myers, D. C. Ralph, J. A. Katine, R. N. Louie, R. A. Buhrman, *Science* **1999**, *285*, 867.
[223] Y. Huai, *Association of Asia Pacific Physical Societies (AAPPS) Bull.* **2008**, *18*, 33.
[224] A. Brataas, A. D. Kent, H. Ohno, *Nat. Mater.* **2012**, *11*, 372.
[225] C. Song, B. Cui, F. Li, X. Zhou, F. Pan, *Prog. Mater. Sci.* **2017**, *87*, 33.
[226] T. Maruyama, Y. Shiota, T. Nozaki, K. Ohta, N. Toda, M. Mizuguchi, A. A. Tulapurkar, T. Shinjo, M. Shiraishi, S. Mizukami, Y. Ando, Y. Suzuki, *Nat Nano* **2009**, *4*, 158.
[227] F. Xiu, Y. Wang, J. Kim, A. Hong, J. Tang, A. P. Jacob, J. Zou, K. L. Wang, *Nat. Mater.* **2010**, *9*, 337.
[228] C. A. F. Vaz, J. Hoffman, C. H. Ahn, R. Ramesh, *Adv. Mater.* **2010**, *22*, 2900.
[229] H. Ohno, D. Chiba, F. Matsukura, T. Omlya, *Nature* **2000**, *408*, 944.
[230] Y.-H. Chu, L. W. Martin, M. B. Holcomb, M. Gajek, S.-J. Han, Q. He, N. Balke, C.-H. Yang, D. Lee, W. Hu, Q. Zhan, P.-L. Yang, A. Fraile-Rodríguez, A. Scholl, S. X. Wang, R. Ramesh, *Nat. Mater.* **2008**, *7*, 478.
[231] C. Chappert, *Science* **1998**, *280*, 1919.
[232] J. H. Franken, H. J. M. Swagten, B. Koopmans, *Nat. Nanotechnol.* **2012**, *7*, 499.
[233] M. Weisheit, S. Fahler, A. Marty, Y. Souche, C. Poinsignon, D. Givord, *Science* **2007**, *315*, 349.
[234] H. J. A. Molegraaf, J. Hoffman, C. A. F. Vaz, S. Gariglio, D. van der Marel, C. H. Ahn, J.-M. Triscone, *Adv. Mater.* **2009**, *21*, 3470.
[235] T. Cai, S. Ju, J. Lee, N. Sai, A. A. Demkov, Q. Niu, Z. Li, J. Shi, E. Wang, *Phys. Rev. B* **2009**, *80*, 55.
[236] H. Ohno, *Nat. Mater.* **2010**, *9*, 952.
[237] S. Dasgupta, B. Das, M. Knapp, R. A. Brand, H. Ehrenberg, R. Kruk, H. Hahn, *Adv. Mater.* **2014**, *26*, 4639.
[238] J.-M. Hu, L.-Q. Chen, C.-W. Nan, *Adv. Mater.* **2015**, *28*, 15.
[239] S. Dasgupta, B. Das, Q. Li, D. Wang, T. T. Baby, S. Indris, M. Knapp, H. Ehrenberg, K. Fink, R. Kruk, H. Hahn, *Adv. Funct. Mater.* **2016**, *26*, 7507.
[240] D. A. Gilbert, A. J. Grutter, E. Arenholz, K. Liu, B. J. Kirby, J. A. Borchers, B. B. Maranville, *Nat. Commun.* **2016**, *7*, 12264.
[241] J. A. Gomes, M. H. Sousa, F. A. Tourinho, J. Mestnik-Filho, R. Itri, J. Depeyrot, *J. Magn. Magn. Mater.* **2005**, *289*, 184.
[242] X. Wang, L. Gao, L. Li, H. Zheng, Z. Zhang, W. Yu, Y. Qian, *Nanotechnology* **2005**, *16*, 2677.
[243] R. D. Gunning, K. Rode, S. R. G. Sofin, M. Venkatesan, J. M. D. Coey, I. V. Shvets, J. G. Lunney, *Appl. Surf. Sci.* **2009**, *255*, 5245.
[244] T. Hasegawa, K. Terabe, T. Tsuruoka, M. Aono, *Adv. Mater.* **2011**, *24*, 252.
[245] S. Tappertzhofen, I. Valov, R. Waser, *Nanotechnology* **2012**, *23*, 145703.
[246] K. Krishnan, M. Muruganathan, T. Tsuruoka, H. Mizuta, M. Aono, *Adv. Funct. Mater.* **2017**, *27*, 1605104.
[247] C. Chen, S. Gao, F. Zeng, G. Y. Wang, S. Z. Li, C. Song, F. Pan, *Appl. Phys. Lett.* **2013**, *103*, 043510.
[248] X. Zhu, W. Su, Y. Liu, B. Hu, L. Pan, W. Lu, J. Zhang, R.-W. Li, *Adv. Mater.* **2012**, *24*, 3941.
[249] T. Tsuruoka, K. Terabe, T. Hasegawa, M. Aono, *Nanotechnology* **2011**, *22*, 254013.
[250] I. Valov, I. Sapezanskaia, A. Nayak, T. Tsuruoka, T. Bredow, T. Hasegawa, G. Staikov, M. Aono, R. Waser, *Nat. Mater.* **2012**, *11*, 530.
[251] W. Yi, S. E. S. A. ev, F. Miao, M. X. Zhang, J. J. Yang, A. M. Bratkovsky, R. S. Williams, G. Medeiros-Ribeiro, *Nat. Commun.* **2016**, *7*, 1.
[252] S. R. Nandakumar, M. Minvielle, S. Nagar, C. Dubourdieu, B. Rajendran, *Nano Lett.* **2016**, *16*, 1602.
[253] D. M. Eigler, E. K. Schweizer, *Nature* **1990**, *344*, 524.
[254] K. Schouteden, E. Janssens, H.-Y. T. Chen, Z. Li, C. Van Haesendonck, G. Pacchioni, K. Lauwaet, P. Lievens, *ACS Nano* **2015**, *9*, 5318.
[255] F. E. Kalff, M. P. Rebergen, E. Fahrenfort, J. Girovsky, R. Toskovic, J. L. Lado, J. Fernández-Rossier, A. F. Otte, *Nat. Nanotechnol.* **2016**, *11*, 926.

© 2017 WILEY-VCH Verlag GmbH & Co. KGaA, Weinheim